Dissertation

Graphene-based field effect transistors for the biosensing of toxins

ausgeführt unter der Leitung von

Prof. Wolfgang Knoll
Austrian Institute of Technology
and
Competence Centre for Electrochemical Surface Technology

Thesis zur Erlangung des Grades eines
„Doctor of Philosophy“ (PhD) der Fachbereiche Biologie und Medizin
der Johannes Gutenberg - Universität Mainz

von

Ciril Reiner-Rozman
a0504192
Muthgasse 11
A-1190 Wien

Wien, im Mai 2016

Erstgutachter: Prof. Wolfgang Knoll

Zweitgutachter: Prof. Harald Paulsen

Prüfungsdatum: 14.07.2016

Publications

Paper

Graphene-based liquid-Gated field effect transistor for biosensing: Theory and Experiments, *Ciril Reiner-Rozman, Melanie Larisika, Christoph Nowak, Wolfgang Knoll*, Biosensors and Bioelectronic 70, **2015**, pp.21-27.

Scanning Electrochemical Microscopy as a Characterization Tool for Reduced Graphene Oxide Field Effect Transistors, *Ciril Reiner-Rozman, Jürgen Schodl, Christoph Nowak, Christoph Kleber*, e-Journal of Surface Science Nanotechnology 13, **2015**, pp.366-372.

Electronic Biosensing with Functionalized rGO FETs, *Ciril Reiner-Rozman, Caroline Kotlowski, Wolfgang Knoll*, Biosensors 6(2), **2016**, pp.17.

Electronic Olfactory Sensor Based on A. mellifera Odorant-Binding Protein 14 on a Reduced Graphene Oxide Field-Effect Transistor, *Melanie Larisika, Caroline Kotlowski, Christoph Steininger, Rosa Mastrogiacomo, Paolo Pelosi, Stefan Schütz, Serban F. Peteu, Christoph Kleber, Ciril Reiner-Rozman, Christoph Nowak, Wolfgang Knoll*, Angewandte Chemie 54(45), **2015**, pp.13245-13248.

Patents

Flow and pressure sensitive graphene sensor, *Ciril Reiner-Rozman*, ID 14162292.8, **2015**.

Poster

Detection of Aflatoxin B1 from real-life food samples with graphene-based field effect transistors, *"Bioelectrochemistry and more..." Symposium*; June 25, **2015**, Competence Centre for Electrochemical Surface Sciene Technology, Wiener Neustadt, Austria.

Conferences

Construction and optimization of a graphene-based field effect transistor device, *Bioelectronics Symposium*; October 20, **2014**, Nanyang Technological University, Singapore.

Graphene field-effect transistors as biosensors, *VBST Meeting*; September 15, **2014**, University of Bath, England.

Thesis

A diploma thesis was supervised in the frame of the presented work. "Odorant sensing with functionalized graphene field-effect transistors utilizing impedance spectroscopy", *Patrik Aspermair*, **2016**, Technical University of Graz, Austria.

Contents

1 Introduction **3**
- 1.1 Graphene . . . 3
  - 1.1.1 Historical Overview . . . 3
  - 1.1.2 Fabrication Methods . . . 5
  - 1.1.3 Properties of Graphene . . . 8
- 1.2 Field-Effect Transistors . . . 15
  - 1.2.1 FETs as Biosensors . . . 17
- 1.3 Liquid-Solid Interfaces . . . 18
  - 1.3.1 Debye Length . . . 18
  - 1.3.2 Electric Double Layers - Grahame Equation . . . 19
- 1.4 Biosensing . . . 22
  - 1.4.1 Langmuir Binding Kinetics . . . 22
  - 1.4.2 The Energy Landscape Theory of Protein Folding . . . 24
  - 1.4.3 Signal Transduction in Graphene FET Biosensors . . . 26
- 1.5 Mycotoxins . . . 28
  - 1.5.1 Aflatoxins . . . 30
- 1.6 The Corn Kernel . . . 33

2 Scope of Work and Goals **35**

3 Materials & Methods **38**
- 3.1 List of used Chemicals & Materials . . . 38
- 3.2 Preparation Methods . . . 41
  - 3.2.1 Chemicals . . . 41
  - 3.2.2 Preparation of the Field-Effect Transistors . . . 42
  - 3.2.3 FET Setup . . . 43
  - 3.2.4 Characterization Equipment . . . 44
- 3.3 Characterization of the Field-Effect Transistors . . . 47
  - 3.3.1 Graphene Surface Coverage . . . 47
  - 3.3.2 Characteristic Curves . . . 49
  - 3.3.3 Hysteresis . . . 50
- 3.4 FET Device Selection . . . 52
  - 3.4.1 Selection based on FET Measurements . . . 52
  - 3.4.2 Surface Electrochemical Microscopy of Graphene . . . 53
- 3.5 Calculations for the Graphene Field Effect Transistor . . . 58

3.5.1 Calculation of the Source-Drain Current . . . 58
3.5.2 Protein Adsorption/Desorption Kinetics . . . 62
3.5.3 Theoretical Validation of the analytical Array Procedure . . . 63

4 Measurements in buffered Solutions 66
4.1 Introduction . . . 66
4.2 Dependency of the Charge Mobility on pH . . . 66
4.3 Impedance Spectroscopy . . . 70
4.4 Application as microfluidic Flow-meter based on Graphene . . . 72
4.5 Measurements of the Debye-length Dependency . . . 73
4.6 Biosensing of Aflatoxin B1 . . . 76
4.6.1 Basic Sensing Principles . . . 76
4.6.2 Evaluation of the Surface Binding Kinetics . . . 79
4.6.3 Unspecific Binding . . . 82
4.6.4 Cross-reactivity . . . 83

5 Measurements in Real-life Food Samples 87
5.1 Impedance Spectroscopy of Grain Samples . . . 88
5.2 Grain Extract Responses in DC Mode . . . 92
5.3 Surface Passivation . . . 94
5.3.1 Chemical Protective Layers . . . 95
5.3.2 Metal Oxide Passivation Layers . . . 96
5.4 Array Configuration . . . 104
5.5 Array Measurements in Corn Samples . . . 106
5.5.1 Application of the Array Configuration for the Detection of Aflatoxin B1 from Corn Extracts . . . 106
5.5.2 Measurement of a Calibration Curve for the Detection of Aflatoxin B1 from Corn Extracts . . . 109
5.5.3 Evaluation of the established Setup following the USDA-GIPSA Requirements . . . 113

6 Summary and Conclusions 118

7 Outlook 124

8 Appendix I

Bibliography VIII

Abbreviations

Abbreviation	*Long name*
PBSE	1-pyrenebutanoic-acid-succinimidyl-ester
PFDTS	11-Pentafluorophenylundecanoatetriethoxysilane
APTES	3-Aminopropyltriethoxysilane
GPTS	3-Glycidoxypropyltrimethoxysilane
AC	Alternating current
Al_2O_3	Aluminium oxide
a.u.	Arbitrary units
AFM	Atomic force microscopy
BSA	Bovine serum albumin
CNT	Carbon nano tubes
CVD	Chemical vapor deposition
CV	Cyclic voltammography
DNA	Deoxyribonucleic acid
V_i	Dirac point voltage
DC	Direct current
EDL	Electric double layer
Eltopf	Energy landscape theory of protein folding
ELISA	Enzyme-linked immunosorbent assay
E_F	Fermi energy
FET	Field effect transistor
FAO	Food and agriculture organisation
V_G	Gate voltage
GIPSA	Grain inspection, packers and stockyard administration
GO	Graphene oxide
GDU	Growing degree unit
HPLC	High-performance liquid chromatography
HI	Hydriodic acid

Abberiation	*long name*
HCl	Hydrogen chloride
IgG	Immunoglobulin G
$FeCl_3$	Iron(III)chloride
pI	Isoelectric point
LOD	Limit of detection
PBS	Phosphate buffered saline
PEG	Polyethylene glycol
PMMA	Poly(methyl methacrylate)
$KMnO_4$	Potassium permanganate
QCM-D	Quartz crystal microbalance with dissipation
RCA	Radio Corporation of America cleaning
rGO	Reduced graphene oxide
RNA	Ribonucleic acid
SiO_2	Silicon dioxide
I_D	Source-Drain current
V_D	Source-Drain voltage
H_2SO_4	Sulfuric acid
SECM	Surface electrochemical microscopy
TPG	Temperature programmed growth
THF	Tetrahyfrofuran
TiO_2	Titan dioxide
2D	Two-dimensional
UHV	Ultrahigh vacuum
USDA	United States department of agriculture
XPS	X-ray photoelectron microscopy

Abstract

A biosensor setup was designed for the detection of aflatoxin B1 based on field effect transistors (FET) using reduced Graphene-Oxide (rGO) as transducer. For the detection of this analyte specific IgG antibodies are immobilized to the transistor channel area, specifically capturing the analyte and inducing a change of the surface charge at binding events. The dependence of the detected signal on the ion strength of the buffer solution was studied and results were superimposed with the Debye-length theory, demonstrating the applicable ion strengths for the shown type of biosensor. Furthermore, characterization of pH responses and the binding of bovine serum album (BSA) have been tested as a standard for the biosensor. The results were published in Biosensors & Bioelectrononics [1].
Additionally, the field effect transistor was tested with standard electrochemical experiments in electrolyte buffer. The binding affinity of aflatoxin B1 on the corresponding antibody was characterized, measuring basic kinetic parameters according to the Langmuir binding theory for the description of the equilibrium surface coverage as a function of the bulk (analyte) concentration in aqueous solution. The obtained binding coefficient (K_D) for aflatoxin B1 is found to be in the same magnitude as described in literature. Furthermore, the main aim of this project was the detection of aflatoxin B1 from real-life corn samples using anti-fouling layers for the protection of the rGO and the diminishment of unspecific surface potential and charge changes. Therefore a sensor array was used, implicating a FET with the target aflatoxin B1-antibody and a FET with a non-targeted antibody (BSA) for comparison of the response signals. For the realization, reduced graphene oxide (rGO) was synthesized using a wet-chemical method. Afterwards 50 μm channel-width field effect transistors were fabricated using this rGO. Several techniques for the fabrication of a suitable protective layer for the graphene have been tested in this work, including polymers, chemicals with aromatic structures and different sputtered metal oxides. Sputtered metal-oxides showed the most promising approach for the passivation of the graphene layer due to the most efficient ratio of protection efficiency to the loss of specific signal strength. Hence a passivation coating of 30 nm Ta_2O_5 was sputtered on the semiconductor (rGO) without pin-holes. Then, using a silane as linking molecule, the target antibodies (aflatoxin B1) were immobilized on the passivated surface just before measurement in liquid-gated configuration. The passivation prohibits binding of non-specific molecules from the food samples on

the graphene surface, but still allows for surface potential changes when these food samples are flushed over the FET channel. Therefore, a negative control FET is connected serially to the targeted FET and this negative control is performed using non-target antibodies (anti-BSA). The signals of both FETs are then compared and the difference from the signal areas is giving a read-out for the aflatoxin B1 binding on the target antibodies. A comparison of the integrated areas, obtained by the response signals of the FETs during contaminated corn injections, yields the final biosensor read-out. The limit of detection (LOD) in real-life samples was found to be around 10 nM, being two magnitudes higher than for measurements in buffer, but still below the maximum toxin concentration instructed by the EU and US food administration. Calibration curves for the binding of aflatoxin B1 on passivated gate-immobilized antibodies in real-life foodstuffs were obtained using a titration of 5 different contaminated corn food samples and one certified blank corn sample. The detection signals were then obtained by the integration of the separate response signals and the difference of the areas resulting from the integration of the target FET and the negative control.

The presented approach shows promising results for the development of a novel biosensor due to the low assay time (around 2 minutes), small device size, real-time readout and the good cost efficiency. The work on aflatoxin B1 detection was performed in the framework of an COMET project from CEST (Competence Centre for Electrochemical Surface Technology, Wiener Neustadt, Austria) in cooperation with Romer Labs® (Tulln, Austria). Additionally to the sought experimental data on toxin detection from real-life samples in this Ph.D.-thesis a patent for the system as a liquid-velocity sensor was accomplished, showing the logarithmic dependence of the graphene resistance on the volumetric flow rate over the sensing area.

Chapter 1

Introduction

1.1 Graphene

Graphene is a sp^2-hybridized carbon material with a two-dimensional hexagonal lattice. Due to the unique electronic, mechanical and optical properties of graphene, a quickly growing interest in research evolved around this topic over the last decade.

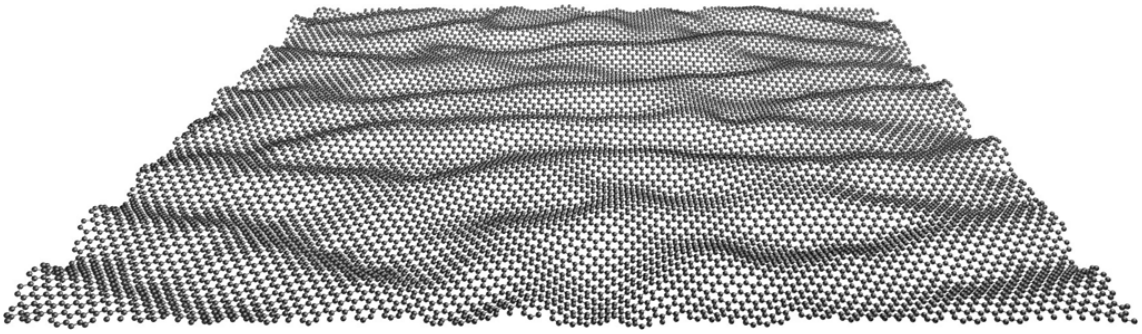

Figure 1.1: The structure of graphene [2]

1.1.1 Historical Overview

For better understanding of graphene as a material, a historical overview on the works with few-layered graphite or graphene is adjuvant, since these papers help giving a better overview or at least a different perspective on the state of this field as we know it today. Therefore we have to go back more than 150 years in time, when in 1859 Charles Brodie experimented on thin oxidized graphite films [3], in-

troducing a synthesis for graphite-oxide that is basically used until today for the fabrication of graphene. The theoretical possibility of a stable two-dimensional crystal was already discussed in the beginning of the 20^{th} century. Bragg [4], Debye and Scherrer [5], followed by Bernal [6] made major publications on the structure of graphite and thereby touched upon the topic of single layers of graphite planes. They explained the fundamental structure of graphite accurately and discussed the effects of fewer graphite layers, but at this point in time the fabrication of a layer with thickness of a single atom was not feasible. A decade later, in the 1930s, Peierls followed by Landau have separately proposed theories on the stability of two dimensional crystals. They showed that a state of matter where the density only depends on two or less dimensions can not be stable due to thermal fluctuations which would destroy the structure of any such crystal, it would melt at applicable temperatures [7, 8]. This observation is described by the Mermin-Wagner theorem, originating from statistical and quantum mechanics. It states that for structures with less than two dimensions a crystalline order isn't possible due to thermodynamic long-wavelength fluctuations at temperatures above absolute zero [9]. This prediction excited a discussion on the stability in two dimensions by a few theoretical physicists in the 1960s [10–12]. Interestingly, around the same time Boehm et al. fabricated thin oxidized carbon films [13], characterized them with a electron microscope and found flakes with thicknesses from 3 to 6 Å, indicating the first documented fabrication of graphene-oxide. In their research they also discussed the possible reduction methods, the intercalation effects of liquids in between separate layers of graphite and the resulting change in layer to layer distance. The effects studied by Boehm and his colleagues are fundamental for the understanding of observations at the interface of graphene and any aqueous liquid, as shown later in this work. Some other unique properties, like the high conductivity of a single layer of graphite were first postulated and theoretically calculated already in 1947 by Wallace in his publication on few-layered graphite [14]. Another approach for the fabrication of grahite-oxide was published in 1958 by Hummers and Offeman [15], is still used until today and known as the Hummers method, defining the basis for wet chemical synthesis methods of graphene. The band structure of a single graphite layer was first calculated by DiVincenzo and Mele in 1984, showing that few layers of graphite have a smaller bandgap than conventional graphite and that a single layer of graphite has no bandgap at the K-point of its unit cell [16]. Their results for a monolayer are in good agreement with the results from experiments

in the 21^{st} century and describe graphene as a semi-metallic semiconductor. Only until Shenderova et al. performed ab initio calculations on the structure of carbon nanocomposites in 2002 and thereby showed that a carbon lattice is stable if at least 6 000 atoms are present, the discussion on the stability of a single layer of carbon perished mostly. Soon after, the first isolated single layer flakes of graphene were found and characterized by Geim and Novoselov in 2004 [17, 18]. For the isolation of a single flake they used the "Scotch-Tape" method, where the researcher is constantly pealing off layers from a piece of graphite, repeating this procedure until finally only a single layer is left at one side of the scotch tape. This layer then was characterized using different laboratory techniques. The procedure has the advantage that no chemical modification of the used graphite is necessary and therefore the obtained graphene layer is pristine. Thereupon they hooked on to the discussion on the stability of the 2D-material as explained above [19]. Their often cited paper from 2007 on the intrinsic ripples in graphene [20] postulated that rippling of the single layers stabilizes the material in that manner that it can't be broken due to thermal fluctuations as stated in the Mermin-Wagner theorem. The group of Geim and Novoselov further experimented with graphene, publishing several papers on it's properties and have been awarded with the nobel price for their work in 2010. Today graphene is used in a wide field of applications and the interest is constantly growing, rendering graphene as one of the major advances in science in the last decade.

1.1.2 Fabrication Methods

Wet Chemical Methods

Graphene can be synthesized from graphite by different wet chemical methods. A few such methods, namely the Hummers method [15] and the synthesis by Boehm [13] and Brodie [3] have been mentioned in the chapter above. The procedure is similar for all three synthesis routines, the basic raw material is graphite, which is oxidized using strong oxidizing agents like potassium permanganate ($KMnO_4$) and sulfuric acid (H_2SO_4) in an aqueous medium. The obtained graphite-oxide has a higher layer to layer distance, which makes it easier to mechanically exfoliate single layers from the graphite-oxide chunks. This procedure can be realized by ultrasonication

or simple stirring of the solution to exfoliate the single layers of graphene-oxide (GO). After a few filtration steps, the single GO layers can be withdrawn from the solution and applied on the substrate of choice. Usually Silicon wafers with a top coated oxide layer are therefore used. In a final step the GO is reduced by a reducing agent. For this purpose many different chemicals can be used and the properties of the resulting graphene depends strongly on the reducing agents. The most popular reducing agents are:

Hydrazine gives the best results regarding reduction efficiency but comes with the downside of being harmful to health if not treated properly [21]

Hydriodic acid is much less harmful but usually doesn't reduce the material as well as hydrazine [22]

Ascorbic acid causes no health concerns at all but has the lowest reduction efficiency of the mentioned chemicals [23, 24].

Another option is the use of thermal or photocaltalytic reduction [25]. In this process the sample is heated up to a certain temperature, which will result in a lower percentage of oxides bound to the graphene layer. Even reduction of graphene using microwaves was shown to be possible [26].
Graphene obtained from wet-chemical synthesis is called reduced graphene-oxide (rGO) to underline the difference to other types of graphene which may vary in properties depending on the fabrication method [27]. In fact, the properties of wet-chemically synthesized graphene and graphene from chemical vapor deposition (CVD) might differ so much in properties that they are considered as different materials.

Chemical Vapor Deposition

CVD is a bottom up technique for the production of graphene [28]. It can be fabricated from the gaseous phase using CVD techniques. Therefore there are many different setups for CVD, mostly plasma induced, or epitaxial methods [29]. CVD can also be performed from atmospheric pressure up to ultrahigh vacuum (UHV) applications, always depending on the desired product. For the fabrication of graphene, the widely used carbon sources are methane or ethene gas but also larger carbon

based molecules can be used [30]. To improve the quality and to change the properties of the resulting graphene films a catalyst can be applied. Briefly, a copper foil is placed in a UHV suitable glass tube (mostly made of quartz) which itself is placed in a spherical oven. Often a pre-modification step of the surface is performed using highly energetic ions and is annealed at temperatures from 1 200 to 1 500 Kelvin. The pressure in the glass tube is decreased to UHV (usually around 10^{-11} mbar), flushed through the inlet of a inert gas and a carrier gas. Mostly hydrogen is used as carrier gas, transporting the desired concentrations of the methane gas over the heated copper foils. There it accumulates and settles on the foils, depending on the parameters of the process until the desired thickness is obtained. The graphene layers then have to be transfered from the copper foil to the desired substrate. Therefore the graphene layer is covered with a polymere like Poly(methyl methacrylate) (PMMA). Then the copper foil is dissolved with a solution of Iron(III)chloride ($FeCl_3$) in hydrogen chloride (HCl) and the leftover graphene on PMMA is transfered to the substrate. As the final steps the PMMA is then dissolved in acetone and burned at high temperatures to minimize the resulting residue from the materials used. CVD can be performed on different substrates like copper (as mentioned above), nickel, cobalt, iron, gold and many more. The choice of the substrate will influence the quality and structure of the fabricated graphene to a large extend [31].

Although CVD is known to fabricate the most pristine graphene layers, this assumption holds only true for ideal processes. The last steps, especially the transfer of the graphene layer to the substrate, will leave residue from the materials like copper and PMMA in small concentrations in the reulting graphene. These can modify the properties of the material, obstructing the applicability when used for e.g. electronic applications [32]. Depending on the used technique and parameters, the uniformity of the grown graphene film can vary strongly. Furthermore also impurities on the surface can lead to nucleation of graphene or graphite layers during the process leading to the formation of grainy structures [33]. This disadvantage was widely discussed, since the formation of these graphitic island can compromise the material quality very strongly and is dependent on the substrate and the system pressure. These problems can be solved by modification of the used materials and equipment, since it also has been shown that the graphene films with the highest purity and uniformity has been produced using CVD [34].

Mechanical Exfoliation

Fabrication methods for graphene using mechanical exfoliation, like the previously mentioned "Scotch-Tape" method have been the first to be used for the fabrication of pristine graphene [17]. Anyhow, these methods are not applicable for the fabrication of bulk amounts of graphene and therefore inefficient due to low reproducibility, low yield and very tedious work for the experimenter.

Other Methods

During the last years also a few other methods for the production of graphene emerged [35]. Temperature Programmed Growth (TPG) for example is using surface-attached hydrocarbons as the carbon source, which then are pyrolized at specific temperatures. Another option is the segregation method, where deposition is performed at such high temperatures that a portion of the carbon atoms segregates into the bulk of the underlying metal substrate. After cooling of the substrate the carbon atoms segregate back from the bulk to the surface and form graphene flakes. Apart from this examples there are even more different methods, which are not discussed in detail here but can be found in literature in different reviews [36].

1.1.3 Properties of Graphene

The properties of graphene have been studied in a wide extend over the last years and in this work the main focal point is at the electronic properties of graphene while other properties are discussed only briefly at the end of this chapter.

As mentioned previously, graphene is a sp^2-hybridized monolayer of carbon atoms arranged in a planar hexagonal lattice. The carbon atoms are bound by covalent σ-bonds between the 2s, $2p_x$ and $2p_y$ orbitals, giving the material very strong mechanical properties, forming a stiff lattice [37]. The unit cell contains two carbon atoms with a interjacent distance of 0.142 nm. The electrons in the $2p_z$ orbitals are bound more weakly by π-bonds and due to their resulting mobility graphene sheets are very conductive. The sum of these electrons is often referred to as electron cloud, due to the delocalisation of the electrons all over the graphene surface and their distribution normal to the plane [38]. Because of the semi-metallic nature of graphene

(resulting from the electron cloud) very high charge carrier mobilities have been observed in graphene, with values of up to 200 000 cm^2/Vs [39]. Values of around 20 000 cm^2/Vs are found at room temperature [40]. The electron and hole mobilities are dependent on the number of impurities or dopands in the graphene layer. For reduced graphene oxide it was shown that potassium and sodium dopands are located around 0.3 nm normal to the surface [41]. Using this distance for the theoretical calculation of the number of dopands depending on the electron mobility, it can be shown that for the highest mobility graphene (200 000 cm^2/Vs) the distance between impurities is around 76 nm with a impurity density of $1.7x10^{10}$ cm^{-2}, while mobilities of around 30 000 cm^2/Vs point at a number of impurities which is one magnitude higher ($1.7x10^{11}$ cm^{-2}) [42]. Besides impurities, the most produced graphene films are polycrystalline [43], have point defects in the form of lattice vacancies or non-hexagonal structures and line defects which can be e.g. dislocations [44]. These defects can significantly alter the chemical, electrical and mechanical properties of the material [45].

The electronic band structure of graphene has overlapping π- and σ-bands with the bandgap being dependent on the position on the graphene lattice. These bands overlap at the K-points, which are highly symmetric points defining the edges of the first Brillouin zone at the corners of the honeycomb lattice. The points of the overlap, which are also called Dirac points, cause a semi-metallic behaviour of graphene materials, having a significant bandgap aside of the Dirac points. The theoretical band properties described here are results of the time-dependent Schrödinger equation in three-dimensional space for the lattice structure of graphene. The described theoretical band structure is disturbed when doping and/or impurities are implemented, which is often caused by chemical synthesis of the graphene material and therefore the band structure of rGO can be significantly altered. Anyhow, all graphene materials display strong electron-hole symmetry, meaning that the band structure close to the Fermi energy (E_F) is constituted in such way that the bands of electron charge carriers π^* and the bands of the hole charge carriers π are approximately mirror images of each other [38]. This means that graphene has conducting properties for both charge carrier types and therefore is a semiconductor with ambipolar properties, displaying p- and n-type characteristics.

For pristine graphene at a temperature of 0 K, at the ground state of the material, E_F is exactly at the potential of the band overlaps at the Dirac points. Therefore the

band structure of graphene satisfies the criteria for a conducting material, where E_F is located in the conduction band, as well as the criteria for a semiconductor, where E_F is found in the bandgap. Because of the band overlap at the Dirac points and E_F located exactly at this point, graphene is the only material satisfying both criteria. This unique property makes graphene a very useful material for applications like field effect semiconductors, because E_F can be shifted almost freely when applying external electric fields. The properties of graphene can then be tuned to close or widen the bandgap, which is a very useful feature for electronic applications. The Fermi velocity, which is the velocity of the highest energetic electrons at 0 K, is around 10^6 m/s [46, 47]. The charge transport by the electron cloud is dependent on two modes: on one side ballistic transport, which is happening independently of the temperature when no scattering by impurities is the case [48, 49] and on the other side classical transport, which is activated at a certain temperature. The ratio of both charge carrier transport types also depends on the size of the used graphene layers [49].

In an experimental environment it is difficult to insulate single layers of graphene, especially when using suspended GO solutions from wet chemical synthesis and therefore the resulting graphene can often consist of multilayered structures. The thickness and number of layers of a graphene surface is mostly characterized by atomic force microscopy, low-energy electron microscopy, Raman spectroscopy or contrast microscopy [50]. The band structure is altered depending on the number of layers in the observed graphene and the ability to tune the bandgap of graphene is more pronounced for multilayered graphene. The properties of a single graphene layer have been described above, it has no bandgap and is a semimetal. The same is true for a bilayer and trilayer with the additional characteristic that a bandgap can be induced by an external potential [51]. The more layers are observed, the closer the band structure and properties converge towards the structure of graphite, which has metallic properties with no free charge carriers at low temperature. Using high frequency applications at high temperatures graphite may display semiconducting properties [52, 53]. Changing the number of graphene layers, another effect, the increase of effective mass and decrease of mobility of the charge carriers [53] is observed. This effect corresponds to the described changes in the band structure above and is a direct implication of the theory and solutions of the Schrödinger equation. The effective band properties of graphene also depend on the underlying substrate. SiO_2 is the most common substrate used and can limit the charge carrier mobility

of the graphene layer [39]. Anyhow, due to the price-efficient availability, superior flatness and good electronic properties SiO_2 still is the most suitable substrate for electronic applications based on graphene. Another noteworthy and unique electronic property of graphene is the Quantum Hall effect [40] which displays shifted Landau levels in comparison to other materials. The effect is observed at high magnetic fields when using bilayer graphene and basically is a quantization of the Hall effect at integer multiples of e^2/h, the squared elementary charge over Planck's constant. Also the dielectric constant of graphene ϵ_g is depending on the number of layers and changes with external electric fields, being almost constant for bilayer graphene in regards to the applied E-field and having values of approximately $\epsilon_\perp = 3$ and $\epsilon_\parallel = 1.8$. For example, graphene consisting of 10 layers can have ϵ_g increased manifold when an electric field is applied [54].

Raman spectroscopy is a powerful tool for the characterization of graphene layer thickness, the density of defects and the plane structure at once [55]. The characteristic features of graphene layers when using Raman spectroscopy are in the region of 800 to 3 000 cm^{-1}, having a so called G-band at 1 580 cm^{-1}, a D-band at 1 360 cm^{-1}, a D'-band at around 1 600 cm^{-1} and a 2D-band at 2 700 cm^{-1} [55]. When interpreting an obtained Raman spectrum, the ratio of 2D-band and G-band intensities can be used for the calculation of the number of layers [56]. A single layer of graphene has the 2D-peak about four times higher than the G-peak. This technique is widely used although criticised by some scientist in regard to accuracy. The heterogenous electron transfer, which is the transfer of electrons from chemical species at the graphene surface to the solid-state electrode is fairly high in graphene with a rate of $1.2x10^{-3}$ cm/s, but independent on the number of defects in the graphene layer [57], whereas studies on CVD-fabricated graphene showed otherwise [58]. Monolayer and bilayer graphene are electroactive materials, having improved electron transfer kinetics in comparison to graphite. Electrochemical studies showed that the interfacial capaciatance from measurements of cyclic voltammograms (CV) for graphene is around 21 $\mu F/cm^2$, using ferricyanide as redox material, which in this measurement is negligible due to the high capacitance of the diffuse layer [57]. The quantum capacitance was measured in other groups and was found around 8 $\mu F/cm^2$ [59]. The values obtained from electrochemical measurements can vary strongly depending on the initial material of the graphene. rGO can still contain a significant amount of different oxygen containing groups, which have profound impact on the electrochemical behaviour of the material [60], changing the capacitances and molecular

affinities but are not affecting the electron transfer rate.

The graphene carbon lattice has a high affinity for the adsorption of gases and it can be shown that rGO can re-oxidize in oxygen rich environments, forming oxygen containing graphitic carbon structures [61]. The resulting doped graphene surface can be regenerated by heating [62]. These properties qualify graphene as a superb material for gas sensors and the state-of-the-art results underline the applicability [63, 64]. When interactions with the gaseous phase are not desired, the graphene layer can be encapsulated for different applications, protecting the layer from oxidation by the environment using parylene and alumina [65] or metal oxides [66]. Also the application of graphene in biosensors requires a protection of the surface against non-specific binding or chemical reactions with the environment, therefore the use of anti-fouling layers and passivation techniques is applied to a wide extent. Depending on the device different materials are used, including non-covalently bound pyrene-functionalized polyethylenglycol (PEG) [67] or other polymers [68], metal-oxides like Al_2O_3 [69, 70], TiO_2 [71], peptides [72], proteins like BSA [73, 74], alkane-amines [75], nitrogen [76] or aromatic structures like fluorobenzene [77] and many more. The key factor for any of these passivation techniques is that the passivating layers don't impair the electronic properties of the graphene, so that the sensitivity of the device is not negatively influenced.

The interaction of graphene with aqueous media is of interest and allows some important insights. When graphene is brought into contact with water an adsorption of water molecules takes place, doping the material [17]. Graphene is hydrophobic in principle, but monolayers of graphene are more hydrophilic than multilayers [78]. GO on the other side is more hydrophilic than rGO due to the loss of polar groups and hence rGO can be seen as an intermediate of pristine graphene and GO regarding the hydrophobicity. Just as a graphite layer [79], also the interfaces of two monolayers of graphene and the space between the SiO_2 substrate can intercalate water molecules. Studies on ruthenium surfaces coated with graphene showed that water intercalates between the substrate and graphene, increasing the interplanar distance by 0.6 Å which is attributed to the hydrophobicity of the substrate and the resulting energetically more favourable state [45]. Hence this should also be the case for SiO_2 substrates. Furthermore, it was shown that confined water is also found in between two layers of graphene [80] and forms square ice at room temperature with a thickness of one to three monolayers. The thickness of the confined water depends

on the graphene layer distance, which can vary due to impurities and defects. For pristine graphene the interlayer distance of bilayered graphene was calculated to 3.3 Å [81], which is enough to encapsulate one or two monolayers of water [82]. This effect has profound influence on electronic properties, especially when using flaky graphene, where single graphene layers are connected by such intercalations and the charge carriers have to bridge the gap, which is exactly where the water is confined. Electric fields applied to these confined water films induce phase transitions, change the crystalline structure of the resulting icy layers and increase the freezing point of the confined water [83]. For the use of flaky rGO these intercalations can be responsible for a change of the observed conductivity when the properties of the aqueous environment are altered, e.g. by change of ionic strength or the pH.

A monolayer of graphene is the strongest material ever measured, having a breaking strength of 42 N/m, which is hundredfold higher than for steel and a elastic stiffness of 340 N/m [37], close to the stiffness of a diamond. The thin structure of graphene makes it very light-weight at the same time, with a weight of only 76 μg/m^2. On the other hand, graphene sheets are very unstable when scrolling or bending into cylindrical shapes [84] and are brittle in regard to the fracture toughness which is comparably low [85].

The optical properties of graphene are unique as well. Graphene is highly conductive and transparent, absorbing 2.3 % of incident white light, which for a single atom layer thick material is a arguably high value [86]. Interestingly this value only depends on the fine structure constant α in a very simple relation, where the opacity is $\pi \cdot \alpha = 2.3$. Every further layer increases the opacity by 2.3 % and at the same time the reflectance is negligible for any thickness, being less than 0.1 % [86]. The visibility of graphene layers strongly depends on the underlying substrate whereby thick substrates with a surface oxide layer are increasing the visibility in reflectance. Therefore transmission microscopy is less suitable in this case. For the optimal visibility the resonance conditions of the light source and the wavelength of any used monochromatic light need to be adjusted properly, because then it is also possible to distinguish between mono- and bilayers of graphene [87] using optical microscopy. Plasmons, collective density oscillations of the electron cloud are the gapless excitations of graphene. They can be used for different applications with high versatility due to the wide applicable frequency ranges, low dissipation and linear dispersion relation. The tuning of the plasmonic properties of graphene can

be achieved by gating with an electric field or by doping, where gating changes the plasmon frequency [88]. Due to these fact graphene can be used for the optimization of optical applications like surface plasmon resonance and hence has become widely used in this field [89]. The refractive index of graphene was found to be 3.135 and the extinction coefficient 0.897, measured using surface plasmon resonance at 670 nm [90].

The possible future application for graphene seem to be endless, with many ideas for the use being published and researched up to date. They include the fabrication of super-capacitors and batteries [91–93], solar-cells [94, 95], photovoltaics [96], memory storage [97], filtration membranes for the desalination of water [98], membranes for gas seperation [99], ultrafiltration membranes [100], as lubricant [79], as superconductors [101, 102], transparent electrodes for applications like touchscreens [103], as thermal conductors [104] for organic light-emitting diodes [105, 106], field effect transistors [17, 107, 108], biosensors [109, 110], as a neuronal electronic interface in medicine [111], stronger material composites [112] and many more.

1.2 Field-Effect Transistors

FETs are electronic elements, fabricated since the 1960s. They have been investigeted by Bardeen and Brattain first in 1948 [113], bringing the nobel prize in physics in 1956. Up to date FETs are the most common electronic devices used in every day life applications. They consist of a Source, Drain and Gate electrode, contacted via a semiconductor. The basic principle of FETs is based on the electric field effect of semiconducting materials, which are used as the so called Gate material. Applying an external electric field at the Gate, the semiconductor can be manipulated with respect to its electrical conductivity due to the low density of electrons in the bulk of the material. Thereby the density of charge carries in the valence and conduction band is altered, changing the distance to the E_F of the material. Depending on the nature of the semiconductor, it hence can supply or withdraw charge carriers for a current flow from Source to Drain when the applied electric field is altered. The effect can be enhanced by doping of the material, which is the insertion of acceptor or donor impurities. They can supply or trap additional charge carriers, depending on the applied electric field [114].
The most simple setting of a FET consists of three electrodes, connected via the semiconductor. In standard configuration, a relatively high current is passing through the FET channel and the Gate material connected via the Source and Drain electrodes. This current then is regulated using a third electrode, the Gate, which usually is connected perpendicular to the semiconductor through an insulating layer. The voltage at the Gate electrode (V_G) is propagating an electric field to the semiconductor and hence, depending on the band structure of the Gate material, the conductivity of the semiconductor is adjusted by V_G. Depending on this effect the FET is called n-type if the channel is conductive for positive V_G or p-type if conductive for negative V_G. Due to this effect the transistor can be turned on and off depending on the prefix of the applied V_G and hence the current from Drain to Source (I_D) can be regulated, adjusted or turned on and off by adjustment of V_G. The characterization of the FET is usually performed by measurements of I_DV_G curves. Therefore a sweep over a range of voltages is performed at the Gate, at the same time a biased voltage from Source to Drain is applied and the response of the I_D is measured. Using the obtained I_DV_G curves, several transistor parameters can be analyzed. The threshold voltage (V_{th}) is defined as the voltage at which the transistor is turned on. It is the voltage in the I_DV_G diagram where the slope of

the response curve exceeds 0, when investigating the curve from the non-conductive (shut) side to the condutive (opened) side of the diagram. Hence V_{th} is the voltage at which the device switches to the turned on state. If the applied $V_G < V_{th}$ the FET is turned off, the cutoff region is reached with no conduction from Source to Drain. When observing the system in detail it can be seen that also for this region a weak inversion current is measured, called subthreshold leakage [115]. Subthreshold leakage is occurring because of highly energetic electrons which can pass the closed channel due to their thermal energy resulting from the Fermi-Dirac distribution of the charge carrier energies [114].
Another important characteristic curve is the relation of Source-Drain voltage (V_D) to I_D for any biased V_G, called I_DV_D curve. It is linear if a conducting material is used for the channel. For a semiconductor the relation consists of a saturation region as well as a linear region, which are divided by a cutoff of I_D when further increasing V_D. For some applications a fourth electrode, the "bulk" is applied on the underlying substrate and can be used for a better integration of the device in circuits [116]. The properties of the FET are defined by the length and width of the channel and the used semiconductor material. The relation of these parameters can be found in equation 3.3. A further option for the characterization of a FET is the evaluation of the transconductance, which is the ratio of input to output signal. The mutual transconductance is mostly defined as

$$g_{\mathrm{m}} = \frac{\Delta I_{\mathrm{out}}}{\Delta V_{\mathrm{in}}} \tag{1.1}$$

which is the fraction of the change in applied voltage to the observed change of the current [117].

Different configurations for the positioning of the Gate electrode can be used. The most common configurations are the top-gated FET, where the Gate is positioned perpendicular to the semiconductor and contacted by an insulating layer. Another configuration is the back- or bottom-gate, where the Gate is found at the backside of the substrate, which is used as the insulating material for the propagation of the electric field. Furthermore, also a liquid-gate configuration can be used, which basically is a top-gated configuration with an ionic liquid as contact material for the Gate electrode to the semiconductor instead of an insulating layer. A detailed description of the gating configurations can be found in [118].

There are different types of FETs including metal-oxide FETs, junction FETs, ion-sensitive FETs, orangic FETs, BioFETs and many more, which are used for different specific applications and depending on the task a wide variety of new FETs is steadily fabricated. The focus of this work is on the application of liquid-gated graphene field effect transistors, sometimes called graFET, which themselves are a new type of FETs emerging since suitable fabrication methods for graphene are available.

1.2.1 FETs as Biosensors

A FET can be used as a biosensor, whereby the readout is produced by holding the variable voltage parameters constant and using the information from the measured I_D as a signal for biochemical processes in the transistor channel. In principle the operation of a FET as biosensor is the reversed operation as in the standard use, where the channel conductance is adjusted by V_G. For the operation as a biosensor the channel conductance is changed by modifications of the semiconducting material due to environmental influences and the I_D is used to read out this change, while V_G is constant. A biosensor is based on the binding/adsorption of target analytes from the medium of interest to bioreceptors attached on the surface and therefore the FET has to be designed in such manner that direct contact of the medium with the surface can be achieved. For the read-out of the binding signals, a transducing unit which transforms the chemical, electrical, optical or mechanical signals at the bioreceptor to a readout signal is necessary.

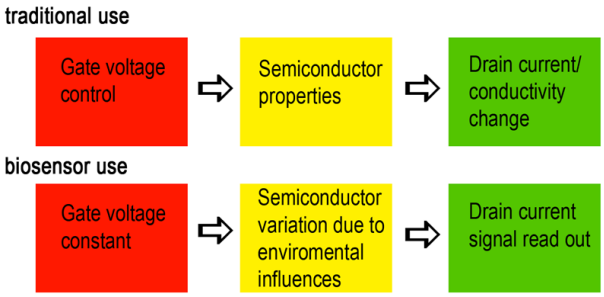

Figure 1.2: Schematic illustration of the basic principle when using a FET as biosensor.

There are almost limitless possibilities for the use of different biorecognition units like antibody-antigen interactions, cells, tissue, enzymatic reactions, nucleic interaction and more. A suitable biorecognition unit must have significant affinity to the analyte and interact with the transducing material at the same time. In the case

of graphene FETs the graphene layer is the transducer while immobilized surface molecules are used as biorecognition units. They are classified as nanobiosensors or Bio-FETs. A schematic image for the comparison of the signal transduction for the use of FETs as biosensors and the classical electronic use of FETs is given in figure 1.2.
There is a wide range of transducing materials which might be applied for the construction of FET based biosensors such as conductive polymers like pentacene [119] or pyrrole [120], silicon nanochannels [121], carbon nanotubes [122] or metal oxides [123]. Depending on the conductivity and sensitivity for events at the biorecognition units the choice of transducing material varies with the aimed application. In general it can be stated that high conductivity and low noise levels combined with good semiconducting properties qualify a transducing material for sensitive detection. Hence graphene is considered suitable for a wide range of applications and has outperformed other materials with regards to sensitivity [109]. Further advantages of FETs in comparison to other biosensors are the good price-efficiency, small device size, easy integration in electronic circuits and the easiness of the fabrication of array configurations on a single device.

1.3 Liquid-Solid Interfaces

The interface formed between a liquid and a solid with respect to its electrodynamic behaviour is a very challenging topic. It has been studied for centuries, resulting in great theories from scientists like Helmholtz, Debye or Stern. A complete description of this topic would exceed the framework of this thesis, but a brief introduction on the relevant phenomena in this area shall be given in the next subsections.

1.3.1 Debye Length

The Debye length (λ_D) is the measure of a charge carrier's net electrostatic effect in solutions. It can also be seen as the interacting radius of molecules in a solution (electronic interaction). For example a λ_D of 100 nm means that a molecule in the solution has a spherical radius (or Debye sphere) of those 100 nm and will (most probably) interact with other molecules (attract or repel) in this interacting

volume. λ_D for ionic liquids/electrolytes can be calculated by knowing the ion strength and properties of the present salts by the following equation, as shown by Russel et al. [124] :

$$\lambda_D = \sqrt{\frac{\epsilon_r \epsilon_0 k_B T}{2 N_A e^2 I}} \tag{1.2}$$

where I is the electrolyte's total ion strength, T the temperature, ϵ_r the dielectric constant of the electrolyte, ϵ_0 the dielectric constant of vacuum, e the unity charge, N_A Avogadro's constant and k_B Boltzmann's constant. Here, one should keep in mind that ϵ_r falls linearly with increasing electrolyte concentration. Hence ϵ_r can not always be seen as a constant and furthermore has dependency on the ion strength [125–127] (e.g. 8.5 mM ionic strength has $\epsilon_r = 80$, 170 mM ion strength has $\epsilon_r = 70$). The importance of the Debye screening length for FETs has also been demonstrated by Stern et al. [128], showing that the expected response signals of liquid-transistors depend strongly on this parameter.

1.3.2 Electric Double Layers - Grahame Equation

The electric double layer (EDL) formed on the rGO-liquid interface has an impact on the measuring setup and is definitely worth a closer analysis. The most basic theory on the behaviour of ionic liquids at charged interfaces is given by the Helmholtz double layer theory [129], which describes the innermost layer of water molecules at the surface. It does not consider diffusion, adsorption or the dipole moments of the solvent. The Gouy-Chapman model includes a diffuse model, describing the charge distribution depending on the distance from the surface [130]. The Stern model combines both theories, introducing a Stern layer at the the interface and is more accu-

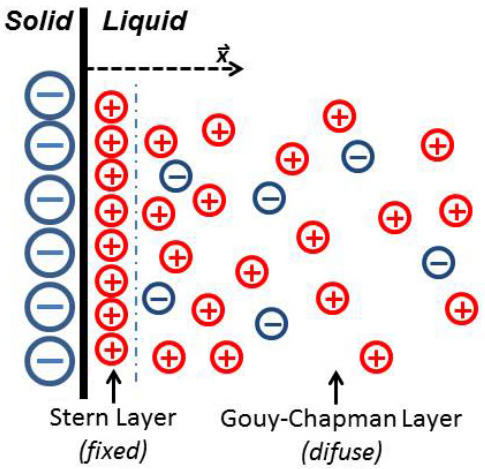

Figure 1.3: Schematic illustration of the liquid-solid interface, the fixed Stern layer and the diffuse Gouy-Chapman layer.

rate for highly charged surfaces [131]. A graphical illustration of the EDL and the theories of Stern and Gouy-Chapman are given in figure 1.3. The theory treated here is the Gouy-Chapman theory for EDLs, considering optimizations proposed by Grahame [132].
For any electrically charged liquid-solid interface the theory can be used to describe surface phenomena, but therefore a relation between the surface charge density σ, the number of free charges $\mathrm{n_i(x)}$ and the surface potential $\Psi(x)$ is needed. The x-coordinate mentioned here is directed normal to the surface.

To obtain a suitable dependency of the charge distribution along the liquid-solid interface, the Poisson equation in one dimension has to be established:

$$\nabla^2\Psi = -\frac{\rho_e}{\epsilon_r\epsilon_0} \tag{1.3}$$

with ϵ_r and ϵ_0 being the electrolyte and vacuum permittivity respectively, Ψ the surface Potential and ρ_e the surface charge at the interface. Furthermore the distribution of the charge carriers has to be taken into account and therefore the Boltzmann statistics for the distribution of the ions in the electrolyte is applied, yielding the connection of charge to the surface potential:

$$n_\mathrm{i} = {n_\mathrm{i}}^0 e^{\frac{-W_\mathrm{i}}{k_\mathrm{B}T}} \tag{1.4}$$

where n_i is the average local concentration of i-ions at the observed point, ${n_\mathrm{i}}^0$ the total number of ions present, k_B Boltzmann's constant, T the temperature and W_i is the work needed to move an ion in the field. This work can also be expressed as the charge movement in the potential Ψ for movements towards the surface: $W^+ = e\Psi(x)$; and away from the surface: $W^- = -e\Psi(x)$. Substituting these observations into the Poisson equation, the following results for movement towards or away from the charged surface are obtained:

$$\rho(x) = ze[n^+ - n^-] \tag{1.5}$$

with

$$n^+(x) = n(\infty)e^{\left(\frac{-ze\Psi(x)}{k_BT}\right)} \tag{1.6}$$

$$n^-(x) = n(\infty)e^{\left(\frac{ze\Psi(x)}{k_BT}\right)} \tag{1.7}$$

where $n(\infty)$ is the number of ions at infinite distance from the surface, z the valency of the observed ions and e the unity charge. Since the rGO-FET system for which these calculations are performed in this work can be assumed as a low potential case, a suitable approximation for the surface potential can be applied ($e\Psi_0 = e\Psi(x = 0) \ll k_BT$), yielding the simplified form of the Poisson-Boltzmann equation:

$$\Psi = \Psi_0 e^{\left(\frac{-x}{\lambda_D}\right)} \tag{1.8}$$

with λ_D being the Debye length (see chapter 1.3.1).

Calculating the surface charge σ from these observations, the Grahame equation for the distribution of charges in an electrolyte at a charged liquid-solid interface can be obtained:

$$\sigma = \sqrt{8n(\infty)\epsilon_r\epsilon_0 k_BT}\, sinh\left(\frac{ze\psi_0}{zk_BT}\right) \tag{1.9}$$

This result gives the dependency of the EDL decay along the direction perpendicular to a solid with surface charge σ on the ion concentration of the electrolyte. It can be used for calculations of the EDL thickness. When λ_D and the topography of the biological materials on the surface are known, this procedure enables the study of the charge distribution around binding events. It therefore enables the optimization of working parameters like ion concentration and applied potentials for the detection of biomolecules in liquids.

1.4 Biosensing

1.4.1 Langmuir Binding Kinetics

The Langmuir adsorption model was derived by Irving J. Langmuir in 1917 [133, 134] and describes the adsorption of a given analyte to a two-dimensional surface. The model requires a surface with a known and constant number of binding sites, which can bind a single monolayer of the analyte and which is in direct contact to the solution containing the analyte in infinity concentration. The interaction of the analyte A and the surface binding sites B is occurring through binding and wash-off of the analyte at the same time for any constant and given concentration until equilibrium of the reaction is reached. The constant reaction and substitution of A to B is depending on the number of occupied sites and the injected concentration of the analyte. For each concentration the system adjusts to a different equilibrium, leading to a dependency of surface coverage on the concentration of the analyte in the solution. When all binding sites are occupied, equilibrium is reached at the saturation concentration, determining the association binding constant K_A, which can be used to determine the affinity of the analyte to the binding sites in a comparative way. The resulting curve is called Langmuir binding isotherm, because of the implicit dependence on the systems temperature and can be described by the equation:

$$\Theta = \frac{pK_D}{1 + pK_D} \tag{1.10}$$

where K_D is the dissociation binding constant, Θ the surface coverage in percent and p is the partial pressure of the desired component in the system. The dissociation constant K_D is the reciprocal value of K_A, the association constant (K_D=K_A^{-1}).

When observing a given binding event which follows the pre-requirements for the Langmuir binding analysis, the kinetic response can be fitted using a simple exponential function e^{kt}, where k is the exponent of the reaction and is also referred to as the observed binding constant k_{obs}. Such a direct observation of the binding con-

stant can lead to the evaluation of the binding affinity of the system by two simple identities:

$$k_{\text{obs}} = k_{\text{on}}[C] - k_{\text{off}} \tag{1.11}$$

and

$$K_{\text{D}} = \frac{k_{\text{off}}}{k_{\text{on}}} \tag{1.12}$$

where k_{on} and k_{off} are the affinity constants for association and dissociation. Anyhow, better accuracy using the Langmuir binding theory is reached when measuring a wide range of the analytes concentrations and plotting the obtained k_{obs} versus the corresponding concentrations. Because of equation 1.11, which has a linear nature, the affinity constants can be obtained by linear fitting over the observed k_{obs}. The slope and offset of this linear fit then define k_{on} and k_{off}, which again can be used in equation 1.12 to obtain the dissociation binding constant K_D and furthermore also K_A.

A commonly used means enabling to estimate K_D using the Langmuir isotherm is the fitting of the concentration to the surface coverage. The surface coverage is obtained by any given response signal in such a way that the concentration where no change of the response is observed for increasing concentrations of the analyte is defined as the saturation concentration. The corresponding response signal value is set as a surface coverage of 100 %. All other response signals obtained are then normalized to this value, plotted against the corresponding concentrations and fitted with the Langmuir isotherm function given in equation 1.10. K_D can then be estimated by the value of the concentration at 50 % surface coverage. The obtained affinity constant is comparable to the IC_{50} value which is usually obtained in systems like e.g. enzyme kinetics. A more detailed derivation of the Langmuir binding theory can be found in [135].

1.4.2 The Energy Landscape Theory of Protein Folding

Proteins are polymers composed of amino acids. These amino acid chains can fold to several conformations of the protein, depending on outer factors and are responsible for the proteins three-dimensional structure. Already in 1959 Kauzmann et al. showed that the hydrophobic forces play a powerful role in the adjustment of the proteins structure [136]. The center of any folded protein will contain the main part of the hydrophobic structures, while the hydrophilic structures will be located at the surface of the protein. Hence changes in the solvents properties will affect the energy of interactions between the hydrophobic groups and vary the proteins total structure.

The protein folding procedure is a highly complex electromechanical process and can be interpreted on a rough multi-dimensional potential surface. Commonly the native state of the protein is described as the conformation with the highest possibility if no external potential is affecting the molecule. These native states can be recognized by structural motifs occurring locally at certain domains of the protein.

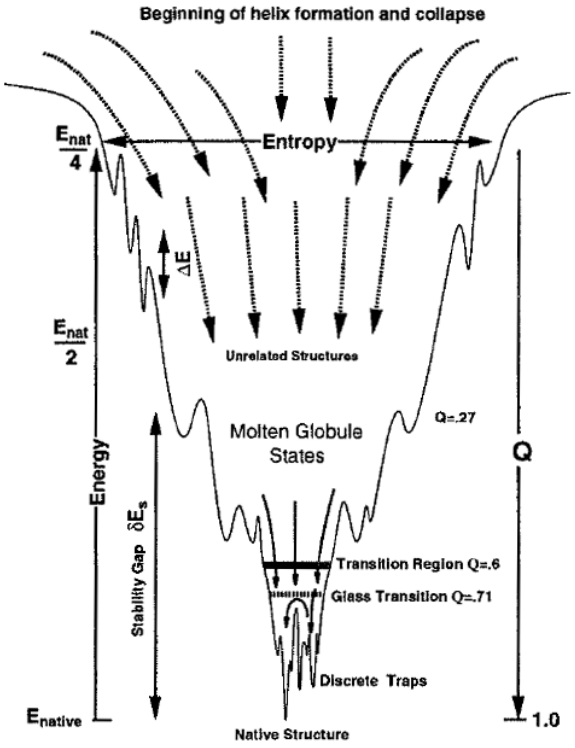

Figure 1.4: Schematic illustration of an realistic energy landscape funnel for a given protein [137].

An attempt to describe the folding mechanisms and conformational changes of proteins is the statistical energy landscape approach which is a statistical description of a protein's potential surface. This theory is phenomenological in it's nature, does not describe the detailed structure of the protein and can be applied for any given molecule [137]. The main, very general assumption is the description by using few energy parameters in a very simple form. Usually the Gibbs energy, free energy and total energy of the system

are used. The energy difference from the ground state to any observed folded state's mean energy is called the stability gap ΔE. Basically the energy landscape theory of protein folding (Eltopf) can be seen as an example of the potential well used in theoretical physics. From that point of view the ground state is located at the bottom of the well.
Other local minima can be found at different excitation energies, the energy landscape reassembles a funnel with the energy walls being rugged to some extend, the so-called roughness of the landscape, depending on the type of protein. The roughness of the landscape defines how much energy is needed to excite the protein to fold from the ground state to any other stable state, overcoming the energy barrier and leading into another conformation which is located at another minimum, as shown in figure 1.4. This approach has given good results in the past, yielding different functions for the prediction of the protein structure.

Some sequences of amino acids found in proteins are thermodynamically foldable, while others are kinetically foldable [138]. In both cases the folding reaction must happen so fast, that it is relevant for biologically processes.

Interestingly, the Gibbs free energy of a protein that has bound to an analyte in it's vicinity in equilibrium can be calculated directly from the observation of time constants using any biosensor with sufficient time-resolved analysis. The theory of the Gibbs free energy and the Nernst equation yield a very powerful identity, allowing to switch from known binding affinities from the Langmuir theory, to the corresponding change in Gibbs free energy [139].

$$\Delta G(pH) = -2.303\ RT\ log(K_D) \tag{1.13}$$

This relation gives us the difference in energy from the ground state to the conformation of the protein when the analyte has bound, and therefore defines the height of the energy landscape for protein folding. The width and roughness of the energy landscape funnel still remain unknown, nevertheless the energy needed for a conformational change to the state of the protein where an analyte is bound is calculated by the given relation.

The Eltopf allows to obtain further thermodynamic parameters, like the density of states, from which the entropy can be calculated directly. Unfortunately, for a

detailed and explicit calculation the exact structure of the energy funnel has to be known. An explicit analysis of the energy landscape for given proteins was not performed in this work, furthermore the Eltopf was used for theoretical considerations and the explanation of the transduction principle of the FET.

1.4.3 Signal Transduction in Graphene FET Biosensors

During a binding event of a protein immobilized to the rGO, the conformation of the protein changes. This conformational change causes a displacement of charged areas in the protein, inducing a small dipole momentum. This momentum can locally have significant energy to transfer to molecules close by (approximately 0.5 nm) but will not have any net effect on molecules located further away, since the resulting potential drops with $1/R^3$. Anyhow, the energy transfer to the nearest neighbours, which in fact can only be ions from the buffer solution in the EDL will lead to a displacement of the EDL. Hence a change of the surface potential is obtained, if the distance of the binding event from the surface is less than the Debye length of the system, following equation 1.8. The charge carrier mobilities in the underlying rGO change when such surface potential variations occur. Furthermore, the resistance of the rGO-FETs and the observed $I_D V_G$ curves will be modified by such binding events.
In other words, the binding of an anlayte at the antibody will change the Gibbs and free energy of the systems surface. The corresponding relation can be calculated from the Langmuir binding theory and the "Nernst-like" identity (equation 1.13). Using the Eltopf (see chapter 1.4.2), this relation gives us the difference in energy from the ground state to the conformation of the protein when the analyte has bound and therefore defines the height of the energy landscape. The roughness of the energy landscape funnel still remain unknown, but the energy needed for a conformational change when an analyte is bound is determined by the given relation.
Due to this conformational change of the protein, two types of charge carriers are displaced, namely:

1) Displacement of the intrinsic protein charge, which is very low in comparison to the total EDL charge, but can have a significant effect on the adjacent ion charges, due to a chain reaction like displacement of the Helmholtz layer, depending on the signum of the applied electric field.

2) The displacement of the EDL (induced as stated above) will change the electron and hole mobility because of the different surface charge, which itself is in direct contact with the EDL and will have a inverse proportional signum of the charges from the EDL displacement. This effect will create or remove "charge obstacles" on the surface of the rGO, which in fact will modify the electron and hole mobility and therefore displace the $I_D V_G$ curve from left to right or vice versa.

For the case of V_G=0, two facts have to be taken into account. Firstly, the potential difference from the Source or Drain electrode to the Gate electrode is still given, which will create an EDL in the opposite direction as if the potential is applied at the Gate. Secondly, the charge displacement at the surface would also occur if the system is not situated in an electric field, since the sole presence of ion charges in the vicinity of the protein will trigger an interaction when the protein changes conformation. In this case the charge displacement happens with increased disorder (higher entropy - therefore a wider energy landscape funnel in the Eltopf theory), resulting in a higher noise level of the I_D baseline of the FET.
The capacitance of the system could also be discussed in this context because it also defines the I_D of the FET. Surface charge variations also modify the capacitance of the system, which is directly dependent on the charge signum and the number of charges at the liquid-solid interface. As will be shown in equation 3.3, a change in charge carrier mobility (induced by the change of the surface charge density) and a change in the capacitance (due to the displacement of the EDL and surface charge) have a direct effect on the FET read-out.

In conclusion, it can be stated that the dipole momentum induced by binding events is not the source of the observed response signal, but triggers a cascade of charge displacements which in the end modifies the charge carrier mobilities and capacitance and therefore the FET read-out.

1.5 Mycotoxins

Mycotoxins are produced as secondary metabolites by fungi like *aspergillus flavus* and have been discovered in the 1960s. These moulds have no chlorophyll and are typically classified as parasites, reproducing via spores, called conidium, which are small structures that can produce new individuals [140]. A single type of mould can produce different types of toxins, but one type of toxin can be produced by different moulds [141]. Mycotoxins are harmful to human health, interacting with the human organism in many ways, interfering with cellular respiration, carbohydrate and lipid metabolisms, can even bind to DNA or RNA [142], cause allergic reactions and weaken the immune system. They can be found in the mould itself or in the substrate on which the mould grows. Air-borne mycotoxins can also endanger human health by inhalation [143], which makes indoor growth of moulds hazardous for the inhabitants. The reason for the production of mycotoxins by mould is not yet cleared out. It is assumed that the mycotoxins are used as a defensive mechanism, protecting the fungus from insects and at the same time the toxins are weakening competing species [144].

In a simplified explanation, moulds invade potential hosts by adsorption of their conidium on the surface of the plant. The conidium is covered with a self-inhibitor, which prevents germination of the spore and difuses through the plants cuticle as soon as in contact with the host, leading to germination of the conidium [145]. The actual stage of infestation depends strongly on the type of fungus, some moulds kill the plant cells immediately to feed on them, others form a biotrophic relationship, keeping their host alive while feeding on their nutrients [146]. A differentiation between moulds that are infecting their hosts pre- or post-harvest is adjuvant because of the wide range of mechanisms leading to mycotoxin contamination in plants, which can be split into these two groups. Post-harvest pathogens have easier excess to their hosts if the surface is damaged or wounded, leading to higher growth rates. Once the host barriers are overcome, the pathogen changes from a possible biotrophic stage to the necrotrophic stage, killing the host by modulation of the pH environment in the plant, slowing down enzymatic activity and gene expression of the host and accelerating the mould proliferation to a more suitable environment for the enzymatic arsenal of the fungus [147]. The change of pH happens by secretion of ammonia for alkaline fungi or organic acids for acidic fungi [145]. Furthermore, also

reactive oxygen species are produced by enzymatic reactions of the fungus, which induces cell death of the host plant [148]. Depending on environmental parameters, the fungus can produce significant amounts of mycotoxins in this stage, depending on the availability of nutrients and hence it has been shown that the moulds in harsh or nutrient rich environments don't produce secondary metabolites [149]. When the environmental parameters are suitable for the fungus at beneficial pH and salt concentrations and sufficient access to glucose is given, the mould will sporulate [150], relieving conidium to spread further. Understanding the cycle of mould infestation can help to preclude toxin contamination by different methods like conservation, the use of fungal viruses [151],engineering of ethylene-free fruits [152] or the use of competing fungi [153] [145].

Mycotoxins represent one of the biggest threats to food and feed safety with estimated 25 % of the world's food crops being affected, as published by the Food and Agriculture Organisation (FAO) [154]. The occurrence of mycotoxins strongly depends on climatic and geographical factors and might differ for a certain location from year to year. This is a key factor for the immanent humanistic need of supplying the world population with basic food availability and on the other hand also an important economic factor, because the incomes from luxury products like coffee are also minimized due to toxin contamination. Agencies like the European Comission, US Food and Drug administration, the World Health organisation or the FAO discuss the problems concerning mycotoxins contamination of food stuffs and propose legislatures ensuring the consumers safety. This is the major motivation for the development of suitable biosensors, which have become more sensitive, cheap and easy to handle over the last decades. Therefore the percentage of contaminated food and feed stuffs found by testing has risen during the last decade because of better availability and sensitivity of the analytical equipment. Hence the amount of contaminated food in markets is minimized, but the harvest profits are reduced at the same time due to the expenses for post-harvest tests of the crop. The need for further development of price-efficient biosensors for the rapid detection of toxins can be demonstrated by the example of the 2004 toxin outbreak in Kenya. The outbreak led to 125 deaths and hundreds of treated patients after consumption of aflatoxin contaminated (mostly homegrown) maize. The contamination was induced by a strain of *Aspergillus flavus* which was not previously found in Africa [155].

Mycotoxins can not be destroyed or broken down easily by means of food treatment

like cooking or freezing. They can't be digested and remain in the organism of any species consuming contaminated food [156]. More than 400 different types of mycotoxins have been found until today, with new ones being discovered constantly. Only a few types are commonly found in food stuffs, namely aflatoxins, ochratoxin A, alternariol, patulin, citrinin and trichothecin [157]. Contamination of food can only be confirmed by analytical testing of the foodstuffs. It can be challenging to find a representative sample from a lot or silo which needs to be chosen carefully due to the heterogeneous distribution of the toxins in large food stashes. The state of contamination can only be determined by laboratory tests because toxins can be already present without any visible sign.

1.5.1 Aflatoxins

Aflatoxins are one of the best surveyed toxins up to date and are mostly found in products from Asia, Africa and America. They are considered to be the most powerful naturally occurring hepatocarcinogen [158], being the most toxic, teratogenic and mutagenic member of the mycotoxin family. Aflatoxins are produced by the mould species of *Aspergillus flavus* and *Aspergillus parasiticus* in a wide range of variation, containing at least 28 aflatoxin types [159]. They exhibit fluorescence of specific color indicated by their names like aflatoxin B1, B2 or aflatoxin G1, G2, where the B stands for blue and G stands for green [160]. They have heterocyclic structures, are highly oxygenated and different aflatoxins have similar structures [161]. Aflatoxin B1 (AfB1), which is mainly targeted in this work, is the most potent toxin and carcinogen among the aflatoxins, being a highly unsaturated molecule with no hydroxyl group (the structure of AfB1 is shown in figure 1.5). The biologocal activity of AfB1 is ascribed to the K-region, at the 2-3 π-bond of the molecule, which binds via electrophilic addition and when hydroxylated, the toxin looses it's carcinogenity [161]. At the same time AfB1 requires metabolic activation to exert its reactivity [162]. Ingestion of AfB1 causes a syndrom called aflatoxicosis, which primarily causes liver failure, edema of legs, abdominal pain and vomiting, but also accumulates in the heart, brain and kidneys and is most destructive for infected

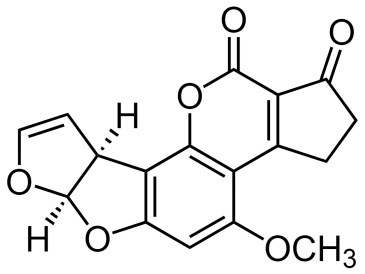

Figure 1.5: Structure of aflatoxin B1.

children. It is also argued that AfB1 ingestion is the main cause for liver cancer, because affected tissue samples show strong blue fluorescence and occurrence overlaps with AfB1 contaminated regions [163].

Biosensing of Aflatoxin B1

AfB1 is a small molecule with a size of 312.28 kD and is electrically neutral. Due to the charge neutrality of the molecule, conventional electronic methods did not reach the limits of detection (LOD) so far that can be observed when using more widespread analytical methods like enyzyme-linked immunosorbent assay (ELISA) or high-performance liquid chromatography (HPLC). ELISA tests for the detection of AfB1 are already commercially available and are advertised with a LOD around 1 pM in buffer and around 30 pM in real-life samples. This is well below all allowed maximum concentrations of AfB1 in food stuffs instructed by the international food safety legislations. Such low detection limits are found for a few publications [164] and several commercial products which can also be used in-field, while most publications using ELISA show limits of detection around 500 pM, e.g. [165, 166]. The main disadvantages of this approach are the long assay time, which usually is more than several hours, the very high effort in plate preparation before measurement and relatively high cross reactivity rates (between 30 and 70 %) [167]. HPLC on the other hand, suffers from interferences from the sample background components, resulting in strong baseline drifts or the overlapping of peaks. It requires the use of bulky equipment which can only be used in laboratory conditions and also has relatively long assay times. The LOD using HPLC for real-life samples depends strongly on the named limitations. Newer techniques are able to correct baseline drifting by mathematical and statistical correction terms and de-convolute overlapped peaks using special computer software. Vosough et al. [168] have shown that HPLC is able to detect AfB1 concentrations with a LOD of approximately 8 nM, using second-order algorithms for multi-target analysis. The problem of long assay times and portability was tackled in [169], presenting a portable immunoaffinity fluorometric biosensor based on optical detection from cuvette. The work demonstrated detection times of less than 2 minutes and a LOD of 300 fM in buffer, but has not been tested for measurements in foodstuffs, which probably would not be possible for

highly viscous liquids due to the proposed structure of that biosensor.

Electrical detection of AfB1 was demonstrated on Silicon based FETs utilizing gold nanoparticles [170]. The approach is based on an indirect competitive immunoassay leading to a LOD of 3 nM for the described biosensor. The measurements have been performed under dry conditions, evading Debye length dependency due to the drying of the liquid in the channel prior to measurement. Although the sensing characteristics and the detection principle based on nanoparticles demonstrate very promising applicability for the detection of AfB1, the method in [170] is very facile and needs the use of lithography, etching, annealing, CVD, plasma treatment and nanoparticle synthesis. Furthermore, no detection in real-life food samples was demonstrated in that work.

Another indirect biosensor was proposed in [171], measuring the concentration of *A.flavus* in rice with the use of carbon nanotube based FETs. The *A.flavus*-antibodies are bound to the nanotubes by a protein G, ensuring ideal orientation. The rice samples were extracted in buffer and measured in liquid-gated FET configuration. Passivation was achived with Tween20 and gelatine. The LOD was found for 10 μg of *A.flavus* per g of rice with an assay time of 30 minutes. Anyhow, the detection of the mould itself is not ideal, because the AfB1 concentration does not necessarily overlap with the presence of the sole mould.

Another electronic approach for the indirect detection of AfB1 are electronic noses [172–174], which are based on gas chromatography. This technique utilizes the detection of gases produced by moulds as an indicator of mould growth and needs to be performed in an insulated headspace which is a major disadvantage.

Furthermore, several aptamer-based biosensors for the detection of toxins were published and are summarized in [175]. These sensors show promising behaviour, but studies have been performed mostly in buffered solutions only and the applicability of aptamers in more complex media like foodstuffs needs to be tested in future due to the novelty of the approach.

Biosensors based on electronic detection with the use of antibodies at the moment show the most attractive features like portability and rapid testing [176]. To our best knowledge no AfB1 biosensor based on graphene was developed until now, although graphene can fulfull several of the requirements for a suitable transducing material used as AfB1 sensor.

1.6 The Corn Kernel

The efficiency of corn growth related to the environment temperature is characterized by the growing degree unit (GDU) which describes the direct link to harvested amounts and is given in °C.

$$GDU = (\frac{T_{max} + T_{min}}{2}) - 10 \tag{1.14}$$

where T_{max} is the daily maximum temperature and T_{min} is the daily minimum temperature of the area under cultivation [177]. The second most limiting factor for the growth of corn is moisture. With corn plants developing 2 m deep roots, short time spans of drought can be well handled by the plant if planted in adequate soil. These two facts ovelap with the ideal conditions for mycotoxin contamination, which are dry stress and high temperatures. Due to the definition of the GDU, it can clearly be seen that temperatures which proliferate good plant growth also enhance the occurance of mycotoxins. Therefore the safest environments for the growth of toxin-free corn are in regions north or south of 35° latitude, where temperatures are too low for strong germination and the accumulation of mycotoxins. Anyhow, most of the corn producing regions are not situated in these latitudes due to the lower yield than in hotter regions. In cooler regions other sorts of crops have to be chosen to assure good harvest before the first frost, which can limit the growing time of the crops in the north. Further promotion of mycotoxin contamination comes from damage by insects, since the physical damage to the plants increases the moisture content and temperature in the grain itself. The contamination of such damaged corn was found to be six times higher than in an comparable undamaged plant [178]. Both factors mentioned above, temperature and moisture are also fundamental for the development of mycotoxins. In comparison to chapter 1.5 on mycotoxins, it can be seen that the ideal environmental conditions for the growth of corn are very similar to conditions under which the highest production of mycotoxins is possible. Therefore mycotoxin analysis is fundamental for the safety of foodstuffs from corn cultivation.

The structure of corn is crucial for detailed analysis of the unspecific binding that happens when a corn extract is brought in contact with a biosensing surface, in-

cluding graphene. To find a suitable passivation against these sorts of unspecific signals, the compositions of the corn extract can be considered. For the scope of this work it can be assumed that most foodstuffs that are relevant for testing of mycotoxins mostly consist of kernels only. Since 82 - 84 % of the corn kernels weight are constituted of endosperm and the endosperm itself is composed of 86 to 89 % of starch [158], we can assume that starch is the most present component in the used corn extracts. The second most prominent ingredient is the germ with approximately 10 % of the total weight and contains 81 to 85 % of the total kernel oil. The other parts of the kernel consist to 6.7 % from hemicellulose and 3 % of cellulose. Insoluble neutral detergent fiber represents the most part of what is left, while we do not need to consider it for the biosensor approach, since it is not soluble and therefore will be dismissed during filtration steps before measurement with the biosensor. Further ingredients are present in portions of less than one percent and have not been considered in this work. However, it has to be mentioned that the signal resulting from the presented biosensor originates from surface charge changes, which can be influenced by charged components of the kernel even if they occur only in such small quantities.

Chapter 2

Scope of Work and Goals

The aim of this work was the development of a sensing platform for the detection of AfB1 from real-life food samples, focusing on grains like corn and wheat. The requirements of sensitivity, selectivity and accuracy for the developed biosensor were defined by the American food safety protocols of the United States department of agriculture for Grain inspection, packers and stockyard administration (USDA-GIPSA) and their limitations to toxin concentrations in the investigated food products. This task requires a versatile biosensor that can generate reproducible data in a variable environment. Therefore a highly sensitive transducing material with large effective area and low degree of unspecific binding of other molecules in the matrix is required. State-of-the-art biosensors don't combine portability, electronic-based detection, rapid read-out, easy handling and low production at once, therefore the ultimate goal for this work is the development of a biosensor fulfulling the named criteria. A FET based on graphene qualifies as a promising transducer for biosensors due to the high conductivity of the semiconductor and the hence expected high sensitivity to surface charge changes. Owing to the complex matrix consisting of food extracts, a protective layer is needed to shield the graphene surface from binding of any unspecific components. A liquid-gated approach is beneficial due to the advantage that the probed solution can be used as the Gate insulating material at the same time. Furthermore, the liquid-gate can be modified with regard to the electrochemical properties best suitable for the sensitive sensing of AfB1.

The goals of this thesis are structured as follows:

- Characterization of the FETs in means of electrical and structural properties, including optimization of the graphene surface, measurements of characteristic curves and studies on the theoretical predictability of the biosensor. Furthermore, two different graphene materials will be compared, including rGO obtained from a modification of the Hummers method and rGO obtained from the synthesis introduced by Brodie. The surface coverage of the FETs will be investigated by optical and electrochemical techniques to analyse the electrochemical activity of the transistor channel. The responsiveness of the FETs to changes of the electrolyte has to be studied, characterizing the dependence of the charge carrier mobility on the pH of the solution and studying the influence of ionic strength by impedimetric measurements.

- Investigations of the biosensing capabilities of the devices by binding experiments of charged proteins in aqueous solutions for the comparison to the detection of uncharged biomolecules will be performed. Furthermore, the dependency on the Debye length, hence the sensing sensitivity in electrolytes with variable properties will be analyzed to obtain insight that is needed for measurements in complex media like food samples. The principle of signal transduction of rGO-FET biosensors has to be discussed, which to our best knowledge is not cleared out up to now. Further on also the binding affinities of AfB1 and the LOD have to be measured and characterized.

- A comparison of different types of AfB1 antibodies and their applicability in FETs has to be tested to improve the sensing capabilities of the devices. The sensitivity and especially selectivity will be tested by studies of the responses to other toxins with chemically similar structures, which could also occur in the same food sample types. The choice of the antibody is of immanent importance, because the sensitivity of the fabricated biosensors can only be as good as the sensitivity of the surface immobilized antibodies.

- The effects of food extracts to the bare graphene surface will be tested in direct and alternating current for the evaluation of the responses by comparison to measurements from solutions with different ionic strengths. This is supposed to yield information on the portion of ionic effects (resulting from ions in the food samples) in relation to the whole unspecific response. A variety of different passivation materials could be used for the presented biosensor, therefore measurements of unspecific binding at various Gate potentials with different

passivation materials have to be performed. A comparison of polyethylene glycol, fluorobenzene, 1,4-Di-n-butylbenzene and metal oxides will be done. The best suitable material will be characterized thoroughly and an optimization for the best suitable thickness and material properties elucidated.

- For the detection of AfB1 from real-life food samples an array configuration has to be established including the development of the theoretical background for the signal deconvolution. Therefore, a series of binding experiments for the construction of a calibration curve needs to be accomplished. The binding behaviour will be characterized by the Langmuir and Rodbard functions, discussing the advantages of both approaches. Finally, a comparison to the requirements of the USDA-GIPSA protocols is pursued for both curves, discussing the possibilities for further optimization and the choice of a suitable calibration curve as well as it's limitations.

Chapter 3

Materials & Methods

3.1 List of used Chemicals & Materials

- Equipment
  - AFM picoView (custom)
  - Analytical scale (KERN)
  - Autoclave (UNIEQUIP)
  - 1/16' tubing connectors (Omnifit)
  - Chrome 99.9 %, 2 - 4 mm pieces (MaTeck)
  - Electrolyte conductivity tester Laquatwin (Horiba)
  - ElProScan ELP1 (HEKA)
  - Evaporation system (HHV FL400 Auto 306)
  - Gate-electrode Dri-Ref^{TM} (Gentaur)
  - Gold 99.99 % purity, granular (MaTeck)
  - Gold contact pins (Tekon)
  - Gold electrodes with cable (Lindeberg)
  - Graphite flakes, 2 - 5 mm (NGS Naturgraphit GmbH)
  - Heating oven (Thermo Scientific Haraeus)
  - IPC High Precision Multichannel Dispenser (ISMATEC)
  - Keithley 2336
  - Keithley 4200 SCS
  - LabRAM HR Raman confocal microscope (Horiba)

  - Molybdenum evaporation boats (HHV Ltd)
  - Multimeter 87V True RMS (Fluke)
  - Omni-LOK connectors (Omnifit)
  - Optical microscope HR800 (Horiba)
  - Optical microscope BX51M (Olympus)
  - Peristaltic pump IPC 8 (ISMATEC)
  - Peristaltic pump tubings, ⊘ 0.64 mm, length 300 mm (ISMATEC)
  - Pipette tips (Star Labs)
  - QSense E4 system (Vaästra Frölunda)
  - Self-designed Flow cell (Lindeberg & IFT, TU Vienna)
  - Shadow masks for 40 μm channels (Fuhrmann)
  - Silicon wafers, 20 x 20 mm (Siegert Consulting eK)
  - Silver-chloride elctrode Flex Ref (World Precision Instruments)
  - Stirring plates (Heidolph MR Hei Tec)
  - SUPRA^{TM} 40 Field Emission Scanning Electron Microscope (Zeiss)
  - Triaxial tip holders (Keithley)
  - Ultrasonicator ELMSA S180H (Elmasonic)
  - Sputtering system Univex 450c (Leybold systems)
  - Impedence multichannel meter VPM3 (Bio-Logis SAS)

- Software
  - AFM picoview (Agilent)
  - Gwyddion 2.33 SPM data analysis tool (Czech Merology Institute)
  - Analytical software for impedance (EC-Lab)
  - Keithley Interactive Test Environment KITE (Keithley)
  - Lua Script editor (individual software)
  - Mathlab 7.13, R2011b (Mathworks)
  - Origin Lab 8.5
  - SmartSEM®V05 (Zeiss)
  - Stream Basic (Olympus)

- Chemicals
  - 3-Aminopropyltriethoxysilane 97 % (ABCR GmbH & Co. KG)
  - Acetic acid 100 % (VWR)

- Acetonitrile 99.8 % (Sigma Aldrich)
- Ammonia 32 % (Merck)
- Anti-BSA monoclonal (Sigma Aldrich)
- Bovine serum albumin (Sigma Aldrich)
- Citric acid 30 % (Sigma Aldrich)
- Disodium hydrogen phosphate Na_2HPO_4 99 % (Sigma Aldrich)
- DI Water 18.2 MΩ/cm (Sartorius Stedium Biotech)
- Ethanol 99 % (Australco)
- Ferrocenemethanol 97 % (Sigma Aldrich)
- Graphene-oxide solution (University of Bayreuth)
- Hydrogen Peroxide H_2O_2 30 % (Sigma Aldrich)
- Hydrazine monohydrate 80 % (Sigma Aldrich)
- Magnetic-bead protein purification kit (Thermo Fisher)
- Monoclonal alflatoxin B1 antibody (Santa Cruz)
- Polyclonal afaltoxin B1 antibody (Agrisera)
- Potassium chloride KCL 99.5 % (Carl Roth GmbH)
- Potassium chloride 99.6 % (AnalaR NORMAPUR, VWR Chemicals)
- Potassium dihydrogen phophate KH_2PO_4 99 % (Sigma Aldrich)
- Potassium ferricyanide 99 % (Sigma Aldrich)
- Pyrene butanoic succinimidy ester (Invitrogen)
- Silica gel (Merck)
- Sodium chloride 99 % (Riedel-de-Haen)
- Sulfuric acid 98 % (Sigma Aldrich)
- Tetrahydrofuran 99 % (Merck)
- Tris (Sigma Aldrich)
- Tween®20 (Sigma Aldrich)

3.2 Preparation Methods

3.2.1 Chemicals

Buffered Solutions

Phosphate buffered saline (PBS) with total ionic strength of 17 mM were applied for all experiments; pH-values were adjusted using NaOH and KOH solutions. 1-pyrenebutanoic acid succinimidyl ester (PBSE) was used as linker, purchased from Sigma Aldrich and diluted to a 2.5 μM solution in tetrahydrofuran (THF) and applied on the prepared FET devices shortly before antibody incubation for 5 minutes until the THF is vaporized. The Anti-BSA stock solution was diluted in PBS at 1 μM concentration and incubated after linker immobilization for two hours on the devices. BSA used for experiments was also solved in 17 mM PBS buffer at pH 7.4 and further diluted to the desired concentration. AfB1 was purchased from Alfa Aesar and solved in 17 mM PBS buffer with the addition of 1 % acetonitrile. Further dilutions were performed using the same buffer, keeping the acetonitrile concentration constant for all solutions. The pH for the solutions used in titration experiments in buffer was adjusted to pH 8 using NaOH and KOH solutions.

Real-Life Grain Sample Extraction

The extraction of different grain types in this work is based on procedures used by Romer Labs®. The intial protocol resulted in very viscous solutions, therefore an optimized extraction routine for corn samples was developed. The aim was to keep the extraction efficiency with regards to the toxin concentration as given in the food samples as high as possible. At the same time the solutions had to be optimized to a less viscous liquid to reduce the responsive behaviour of the extracts to our FET devices. Since earlier experiments showed bad reproducibility of corn extraction as given initially, different optimization steps have been tested. Corn extract yielded by the following protocol shows best reproducibility of the FET responses and had most constant pH and ionic strength:

1. Mixing of 10 g corn + 80 mL of PBS (17 mM, pH 7.4, 1 % Tween®20)
2. Stirring with magnetic stir bar at 600 rpm for 30 min
3. Stick out for 1 h
4. Collection of the top portion (≈ 60 % of the stuck out solution)
5. Centrifugation for 1 min at 4000 rpm
6. Collection of the top portion (≈ 95 % of the centrifuged solution)
7. Filtration via 0,45 μm Micropore filter

When needed the solutions were then adjusted to pH 5 using NaOH and KOH solutions. The extractions efficiency was not evaluated in this work and is assumed at approximately 10 %, based on results of studies on the extraction efficiency by Romer Labs®.

3.2.2 Preparation of the Field-Effect Transistors

Substrate Preparation

Silicon substrates with a 300 nm native oxide layer were chosen as base material for the FETs. The SiO_2 substrates were cleaned with a standard RCA cleaning procedure. The substrates were then submerged in a 1-2 % APTES solution in Ethanol for 1h, APTES forming a self-assembled monolayer to increase the adsorption of graphene. After rinsing with ethanol, the substrates were heated to 120°C for two hours and afterwards cooled down to room temperature. GO sheets were prepared using a variation of the Hummers method derived for the application on FETs [179]. The obtained GO was applied on Si-wafers via spin coating or drop casting of the top portion of the GO solution. The devices were then treated in hermetically sealed glass petri dishes with Hydrazine at 70°C overnight to accomplish graphene-oxide reduction, forming the graphene structure consisting of sp^2-hybridized bonds. The GO reduction success was evaluated in previous studies using X-ray photoelectron microscopy (XPS). Flake distribution was preliminary checked with an optical microscope and the chosen devices then characterized using SEM. For the attachment of the antibody to the sensing area, the graphene surface was chemically modified by a bi-functional linker, PBSE. On one end the linker firmly attaches to the graphene surface through $\pi - \pi$ interactions with a pyrene group and on the other hand it covalently reacts with the amino group of the protein to form an amide bond. For

the immobilization 20 μL of a 2.5 μM PBSE solution in Tetrahydrofuran (THF) was placed onto the rGO-FET channel and incubated until the THF has evaporated completely. The samples were washed with THF afterwards to remove any non-bound components from the surface and then dried with compressed air.

Electrical Preparation

Electrodes applied consisted of gold (60-100 nm) with an adhesive layer of chromium (2-3 nm) using a standard evaporation process with a shadow mask. A chip-holder was designed for this process, ensuring the central positioning of the electrodes as well as reducing electrode geometry glazing because of unwanted shadow offset during the evaporation process. Success of the used reduction technique via hydrazine was established earlier [179] and the resistance of FET channel on the substrate was measured to indirectly check the degree of GO reduction by using a Fluke Multimeter "87 V True RMS Multimeter". To assure that the conductivity of the used electrolyte is not higher than the conductivity of the used graphene layers, all devices displaying higher conductivity than 1 000 ohm were dismissed, equivalent to the resistance of 170 mM PBS buffer at room temperature.

3.2.3 FET Setup

The electrical measurements for the characterization of the FETs (I_D vs. t and $I_D V_G$) were conducted using a probe station "Keithley 4200". Results were recorded using the Keithley Interactive Test Environment software. The FETs were electrically contacted using spring-loaded gold contact pins (Tekon®) brazed to gold electrodes with silver cables for the Source and Drain electrodes. For testing of the FET functionality, a Dri-Ref™ from Gentaur was used as Gate-electrode. The electrodes were positioned by mounting to the flow cell and the use of triaxial tip holders (Keithley). For biosensing of AfB1, a silver-silver chloride reference electrode (Flex ref, World Precision Instruments) was used to operate the FET device in liquid-gated configuration with a constant Gate bias V_G of -0.3 V and a constant Source-Drain bias I_D of 0.2 V. The general procedure of the Afb1 titrations experiment started with continuously flushing the detection area with pure buffer (17 mM PBS, pH = 8.0), until a stable baseline of I_D was established.

All measurements were performed using a custom made flow cell (figure 3.1) made from PMMA with fixed flow channel geometry (16 μL), ensuring a defined flow rate of 300 μL/min to minimize mass transfer limitations of the analyte to the sensor surface in all experiments. The material of the cell was chosen to be PMMA, because of its reported biocompatibility [180]. For the generation of a defined flow speed, fixed flow channel geometry, exact electrode contacts and FET positioning, and a defined sample volume are necessary. The construction also provides shock resistance and ensures the setup being largely unaffected by lateral movement or axial orientation. The capacitative properties of the analyte liquid solution, the charged interface, the graphene in the semiconductor channel determine the devices conductivity. This sensing area simultaneously contains the carrier medium and the contact layer and hence enables a real-time readout for several applications. Furthermore, electrode drillings for constant Gate-electrode distance (2 mm) and a hollow with FET geometry for fixed positioning of the devices were incorporated to the flow cell. As observed in almost all biosensor devices, a slight drift in I_D was observed with time. For this reason, the I_D response curves were normalized by subtraction to the baseline current (I_{D0}) for all measurements if not stated otherwise.

Figure 3.1: Image of the custom build flow-cell used for all experiments. [135]

3.2.4 Characterization Equipment

Scanning electron microscopy (SEM)

SEM images were recorded using a Zeiss "SUPRA^{TM} 40 Field Emission Scanning Electron Microscope" instrument.

Atomic force microscope (AFM)

AFM was performed for the evaluation of surface roughness using a custom build device provided by the Austrian Institute of Technology, Techgate, Vienna. The instrument is connected and operated via a picoView software, Agilent. Scanning

was done on a 3 x 3 μm area with a magnification factor of 1 024 and recording speed of 0.3 line scans per second. The resulting data was evaluated and illustrated with a Gwyddion 2.33 SPM data analysis tool.

Raman spectroscopy

Raman spectroscopy was performed using a LabRam Aramais instrument from Horiba Jobin Yvon. Imaging was performed with a 10 x magnification objective and for the measurments a excitation wavelength of 532 nm and exposure time of 20 seconds for three repetitions with a 10 % filter was used. The laser spot size was 520 μm^2.

Optical microscopy

Optical images images were taken with an "Olympus BX51M" microscope in reflection mode.

Surface electrochemical miscroscopy (SECM)

SECM measurements were performed using a ElProScan ELP1 system, provided by HEKA Elektronik Dr. Schulze GmbH, Lambrecht/Pfalz, Germany (HEKA). The system is equipped by a Controller Unit (ElProScan ESC 3), a bipotentiostat/galvanostat (PG 340 USB), a closed-loop optical-encoder based XYZ positioning system (Applied Scientific Instrumentation), a software controlled 45° imaging system (HEKA) for prepositioning of the electrode tip on the sample under visual control, a shear force unit and a data acquisition software (Potmaster, HEKA). Measurements were accomplished in a three-electrode configuration cell consisting of a Pt-disk microelectrode, a Pt wire auxiliary electrode and Ag wire with deposited AgCl as quasi-reference electrode. Ferrocenemethanol, 1 mM in aqueous solution, was used as mediator. Potassium chloride, 100 mM in aqueous solution, was used as supporting electrolyte. Ultrapure water was obtained from a Seralpur Pro 90 CN (Seral) system with conductivity values lower than 0.05 μS/cm. Pt-disk microelectrodes (tip) were purchased from HEKA. To verify the functionality and stability of the microelectrode, CV measurements were done using standard protocols before and after each measurement (data not shown).

Quartz Microbalance measurements with dissipation (QCM-D)

QCM-D measurements were performed on a QSense E4 system (QSense AB, Vaästra Frölunda, Sweden) using a QFM 401 flow module. Dissipation and frequency were measured simultaneously on OSX 303 sensor crystals. A Q-Tools

software was used for data recording.

Cyclic voltammetry (CV) and Impedance spectroscopy

Impedance spectroscopy and CV measurements were performed with a VPM3, Bio-Logis SAS potentiostat. For CV measurements one electrode of the FET was used as the working electrode, potassium ferricyanide was applied above the channel and a platinum wire, used as the reference electrode, was contacted by the solution. Impedance spectroscopy was performed by the application of AC at the Source and Drain electrodes, while the Gate electrode was operated by a biased voltage. Signals were recorded using the VPM3 potentiostat and EC-Lab software.

Reactive sputtering

Reactive sputtering was performed using a Univex 450c, Leybold system. Argon to O_2 ratio was set to 80:20 with a gas flow rate of 6 sccm and chamber pressure of 2 μbar. A power of 40 W was applied to the target to obtain a sputtering rate of 0.048 nm/s.

3.3 Characterization of the Field-Effect Transistors

For the characterization of the fabricated rGO-FETs the graphene surface coverage and distribution were analyzed first. Tunneling electron microscopy (TEM) and scattering electron microscopy (SEM) were applied therefore. Furthermore, Raman spectroscopy was utilized to analyze the quality and impurities of the rGO. In the next step, characteristic curves of the resulting FETs were measured to evaluate the electronic properties. The reversibility of the devices and possible energy loss resulting from previously applied potentials were evaluated by hysteresis measurements.

3.3.1 Graphene Surface Coverage

The graphene coverage of the FET channel is determining the devices electric properties and is finally of importance for the applicability of the FET. The coverage and thickness of the applied graphene films was checked by SEM, TEM and SECM as shown in chapter 3.4.2. The results from the characterization of the surface coverage by SEM and TEM are shown in this chapter. Because two types of rGO were used during this thesis, data for both materials is provided.

Firstly the self-synthesized GO was used for the fabrication of the FETs and was used for all experiments described in chapter 3 and chapter 4 of this thesis. The protocol for the synthesis was established by [179]. TEM imaging was performed to validate the topological structure of a single GO flake. As can be seen from figure 3.2, the unreduced graphene oxide flakes are not entirely flat, but contain wrinkles and foldings. This behaviour has been demonstrated and explained in literature by the enhanced thermal stability due to the wrinkling of the

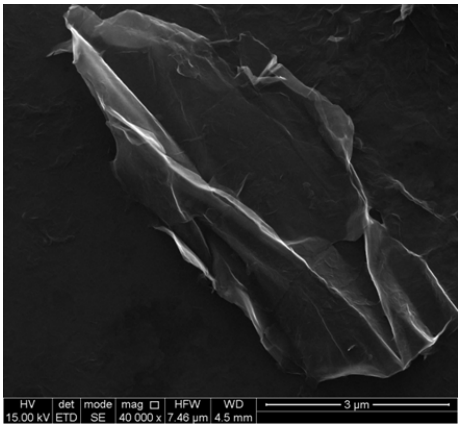

Figure 3.2: A tunnelling electron microscopy image of a single oxidized graphene flake.

rGO sheets [20]. A SEM image of the distribution of this graphene is given in figure 3.4.1c. The self-synthesized GO was always reduced by hydrazine, leading to resistances of the FETs in the range from 100 Ω to 2 kΩ.

The second type of GO used in this work was provided by the University of Bayreuth, namely by Prof. Josef Breu and in contrast to the self-synthesized GO, was not fabricated by a variation of the Hummers method but by the method proposed by Brodie et al. [3]. The resulting GO solution had a graphene concentration of 0.5 wt% and was too highly concentrated for the direct application on the silanized SiO_2 substrates. Therefore dilutions were tested and a suitable dilution step found for a best possible homogeneousness to obtain mostly single layer graphene flakes. The GO was applied by spin coating of 100 μL of the solutions followed by a wash-off with water. SEM images of two of those dilution steps are shown in figure 3.3a&b.

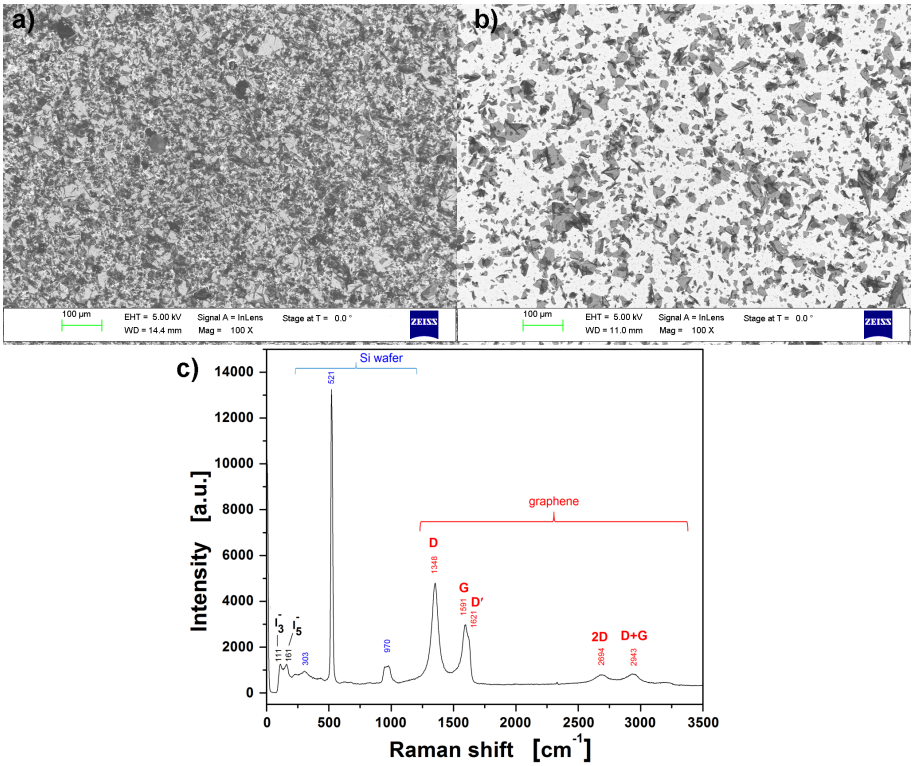

Figure 3.3: a) SEM image of a surface covered with a 1:80 dilution of the stock GO solution. This concentration was used for further fabrication of the FETs. b) Surface coverage of a 1:100 dilution. The coverage is too low with no overlaps between graphene flakes, which would not be ideal for the fabrication of a FET with 40 μm channel width. c) Raman spectrum of a rGO coated SiO_2 substrate for the GO from Bayreuth with a dilution of 1:80, for the same structure as shown in the SEM in figure 3.3a. Because rGO was measured and the 2D and D+G bands are smaller than the D and G bands, a film thickness of two or three graphene layers can be concluded for the measured spot. The peaks at low Raman shifts are contributed to residue of hydriodic acid.

The closest to a single or double layer of graphene flakes with only few overlaps but continuous coverage of the surface was found for a dilution of 1:80 with diH_2O (figure 3.3a). After reduction of the GO obtained from the University of Bayreuth with hydrazine, interestingly the resistances of the resulting FET devices were too high, mostly found in the range of 3 to 6 kΩ. Therefore, different reduction agents were tested to obtain suitable resistances. Ascorbic acid did not reduce the GO to the full extend, yielding very high resistances in ranges of MΩ, which would not be applicable. Furthermore hydriodic acid (HI) was used for the reduction and in contrast to the self-synthesized GO, the reduction efficiency of HI was better than hydrazine but only for the GO obtained from Bayreuth. To characterize if the better conductivity might result from residue of iodine containing groups, the surface was characterized by Raman spectroscopy, presented in figure 3.3c. The Raman spectrum showed some residue from the HI at low Raman shifts from 100 to 300 cm^{-1}. To reduce the iodine residue, an additional heating step for one hour at 180°C after reduction of the samples was used. This temperature is above the boiling point of the most iodine species. Furthermore, the use of FETs fabricated with rGO from the University of Bayreuth was limited to the applications where also a metal-oxide passivation layer is implemented to minimize possible interactions of the iodine residue to the solution or analytes. Utilizing optical microscopy, it was observed that the graphene from Bayreuth shows less impurities, propably due to more sophisticated filtering steps used during the synthesis of that GO.

3.3.2 Characteristic Curves

Electrical properties of the FET devices were tested analogously to [179]. I_DV_D measurements were performed in liquid-gated configuration first, showing no cutoff voltage before 4 V and a linear slope which is depending on the resistance of the measured FET (figure 3.6 shows an excerpt). The slope in the I_DV_D curves clearly followed Ohm's law, hence it was demonstrated that the electrical fabrication of the FETs induced no charge barriers. Because only Source-Drain bias of below 200 mV were used in the experiments, the cutoff voltage does not induce any limitations for the FETs.

The I_DV_G curves for different biases of the Source-Drain voltage (V_D) are shown in figure 3.4. It can be seen that for higher V_D also the slope of the positive and

negative branches in the $I_D V_G$ curves increases. This can be interpreted as an increase in charge carrier mobility, which is linearly dependent on the applied V_D.

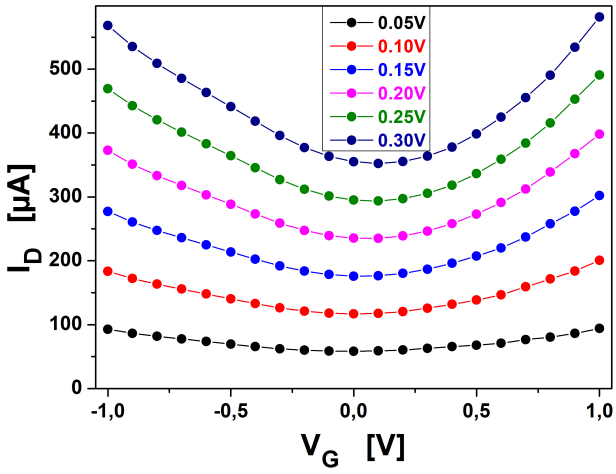

Figure 3.4: $I_D V_G$ transfer curve of the liquid-gated graphene FET under sweeping V_G for different Source-Drain voltages. The color codes for the corresponding V_D are shown in the insert.

For the majority of the tested FET devices ambipolar behaviour with a Dirac point at slightly positive V_G was found. In total an estimated 10 % of the devices showed n-type behaviour, with no observable Dirac point below 1 V. The transconductance g_m was mostly found from 1 to $5x10^{-4}$ S, regardless if an n-type or ambipolar device was used. The characteristic properties and curves of the rGO-based FETs fabricated in this work, are very similar to the results obtained for other rGO-FET systems using exfoliated graphene [107, 110, 179, 181, 182].

3.3.3 Hysteresis

Hysteresis phenomena were checked for several of the presented rGO-FETs. Therefore a cyclic voltage sweep at the Gate electrode was performed starting from negative to positive values. The initial direction was then changed for the following measurement, which should demonstrate that the effect of hysteresis is not dependent on the voltage sweep's direction. For the measurements a standard PBS buffer with pH 7.4 and an ionic strength of 17 mM was used. The area of hysteresis for the left curve in figure 3.5a was found to be $2x10^{-5}$ W, while the area for the right curve in figure 3.5b is $1x10^{-5}$ W. For the five FET devices tested for hysteresis in

average a hysteresis area of (1.28 ± 0.50)x10^{-5} W was found. This result shows the good reproducibility of the FETs with regards to hysteresis, all devices displayed very similar behaviour.

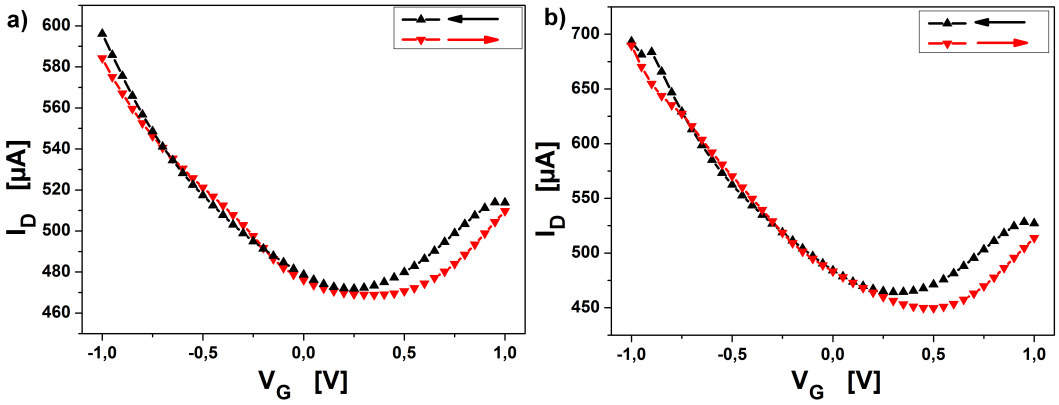

Figure 3.5: Hysteresis of the presented FETs. Measurements were performed in both directions for several devices. a) Representative measurement of a FET's hysteresis, from -1 V to 1 V (red line) and back to -1 V (black line). b) Measurement in the opposite direction: from 1 V to -1 V (black line) and then back to 1 V (red line).

Small areas in the hystersis curves demonstrate the reversibility of the FETs when switched between two states. The results from this study indicate high robustness of the fabricated devices. Furthermore, the displacement of the initial current to the final current after one cycle shows low energy loss of the FET. Since all measurements presented in this work are performed with Gate voltages from -0.4 V to 0.6 V, the effect of hysteresis should not be a limiting factor for the performance of the presented FETs.

3.4 FET Device Selection

The fabricated FET devices were characterized for their geomertic channel properties and outliers eliminated from the selection. Further selection was achieved by comparison of the channel conductivity in ambient conditions and liquid-gated configuration to minimize the leakage current. The obtained devices were then analyzed utilizing surface electrochemical microscopy to confirm the electrochemical activity of the FET channels.

3.4.1 Selection based on FET Measurements

The fabricated FET devices were analysed with respect to the graphene flake distribution by SEM, showing a uniform graphene distribution repeatedly (figure 3.6c). The electrode positioning and channel width were characterized using optical microscopy of 100 fabricated devices. While the desired channel width of the FETs was 40 μm, a variation of $\pm$ 30 % was found, resulting from shadow effects due to the evaporation technique used. Therefore, a selection of devices was performed so that the channel width was constant at (40 $\pm$ 4) μm. An optical image of a FET channel as used for all experiments with width of 40 μm and length of 4 mm is shown in figure 3.6b. In addition resistance measurements across the semiconductor

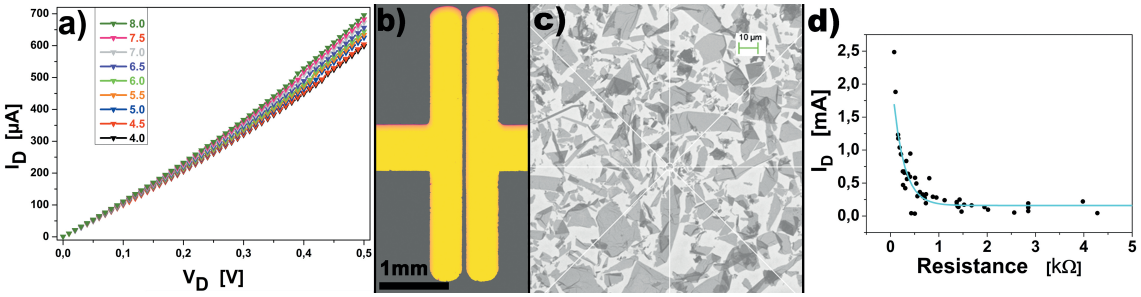

Figure 3.6: a) $I_D V_D$ characteristics of the FETs for pH from 4 to 8; b) optical image of the split geometry with channel width 40 μm and length 4 mm; c) SEM image of a rGO distribution like in the FET channel; d) Measured channel resistance in ambient conditions vs. measured channel current (I_D) in liquid-gated configuration. FETs were chosen with the maximal available variation in resistance for demonstration of the dry device resistance and the corresponding resistance in liquid phase. I_D remains constant at a minimum of around 100 μA with increasing channel resistance due to electrolyte conductivity.

channel at ambient conditions were accomplished to evaluate the graphene contact between (selection of 750 devices, data not shown). From these measurements, 50

devices in the range from 0 to 5 000 Ω were also measured in liquid-gated configuration of the FET. As experimentally verified, the FET baseline stability of I_D in a liquid-gated configuration stabilizes over time (after ≈ 60 min), hence a washing step is required prior to any measurement. After the washing step, the resulting I_D was recorded. The results from the measurements of the FET resistance in ambient condition and the corresponding I_D in liquid-gated configuration (PBS, 17 mM, pH 7.4) were superimposed and are shown in figure 3.6d. Based on Ohm's law, the relation is expected to be linear, if no leakage current is ocurring through the electrolyte. In figure 3.6d this is valid only for devices with resistances below 1 000 Ω, which indicates leakage currents for the used electrolyte if the conductivity of the FETs is lower. Only devices displaying a resistance of less than 1 000 Ω were chosen for later measurements, ensuring that the channel conductivity of these devices is higher than the conductivity of the dielectric isolator/medium layer. This approach created a low variation in the fabricated FETs with respect to the graphene distribution, resistance and channel size. Another good indication is the low energy loss demonstrated by hysteresis measurements of FETs with resistances below 1 kΩ, indicating that capacitative charging and leakage currents are minimized for the selected devices.

3.4.2 Surface Electrochemical Microscopy of Graphene

The devices resulting from the FET selection procedure presented in chapter 3.4.1 were used for further characterization of the electrochemical activity in the FET channel. Surface electrochemical microscopy (SECM) was used therfore. This procedure should verify the presented device selection and discuss the impact of the statistically random surface coverage of graphene in the channel on the applicability of the FETs. The insights obtained in this chapter were published in [183].

Advantages of Surface Electrochemical Microscopy

Wet-chemically synthesized graphene has the advantages of high yields, low production costs and easy application from the solution. On the other hand, problems with rGO are the uncertainty of reduction success and the random surface distribution of graphene flakes. Therefore, the surface coverage and the degree of reduction success of the GO sheets over a large area (detection channel) have to be characterized. A

characterization method like SECM, that allows for such inverstigations is ideal to obtain statements about the statistical quality of fabricated sensing devices. Although methods like Raman analysis or XPS can quantify the reduction rate by analysis of binding energies of the material or for quantitative characterization of the reduction success by examining the amount of sp^2-hybridized orbitals, with these techniques only a very small spot of the actual rGO surface is examined. The appliaction of SECM to evaluate the degree of reduction of the GO sheets is measuring the electrochemical activity and sheet distribution at once for a large area of up to a few mm^2 [184, 185].

Constant distance mode was used for the measurements, which has the advantage of decoupled electrochemical activity information from the topography [186, 187]. Thus, changes in the recorded tip currents originate only from variations of the electrochemical activity of the underlying substrate. Furthermore, the measured current correlates to the position of the tip on the surface and is recorded likewise. For comparison of the electrochemical activity before and after reduction, the electrochemical activity and the topography of a blank SiO_2/Si substrate, a GO covered substrate and a rGO covered substrate were measured. The devices used for these measurements were chosen by the use of the selection procedure, described in chapter 3.4.1. Figure 3.7 shows the 2D and the 3D images of tip currents of a blank sample (a & b), a GO-sample (c & d) and a rGO-sample (e & f) measured by constant distance mode.

Interpretation of the SECM Data

For the blank SiO_2/Si substrate the tip current was measured from 120 to 160 pA, indicating low electrochemical activity. Because the substrate is non-conductive it can't reduce the mediator, resulting in negative feedback (figure 3.7a&b).
The GO-sample shows tip currents around 220 pA along the whole surface, with no differences between GO-coated and blank areas, indicating non-conductive behaviour. As shown in figure 3.7c&d, a tip current of $\approx$ 200 pA was recorded at the beginning of the measurement and during the measurement small drifts of the tip current up to $\approx$ 230 pA were observed. The continous increase and decrease of the tip current with progress of the measurement (17 hours) and no found current peaks, indicate constant electrochemical activity of the surface. The drifting of the tip current over time has to be attributed to a baseline drift resulting from the

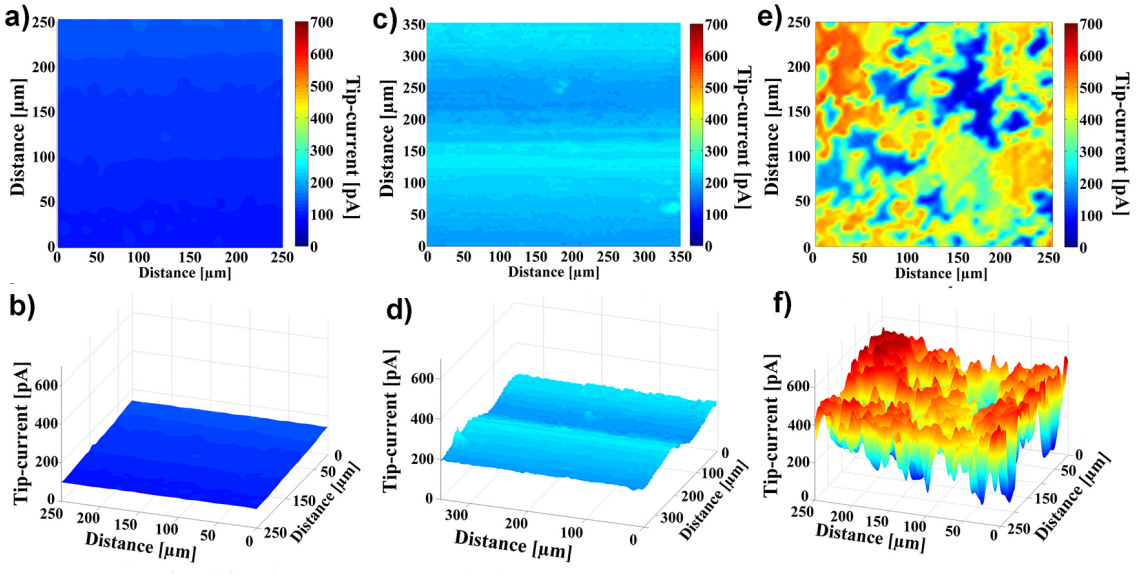

Figure 3.7: a) 2D and b) 3D constant distance SECM images of tip-current from the blank sample; Tip currents from 120 to 160 pA were measured, thus silicon dioxide is a non-conductive material and is not able to reduce the oxidized form of the mediator (negative feedback). c) 2D and d) 3D constant distance SECM images of tip-current from the GO-sample; During the measurement a continuous and nearly linear increase of tip-current from 200 pA up to approximately 240 pA was observed. However, no current peaks are found, indicating a localized electrochemical activity of the surface. e) 2D and f) 3D constant distance SECM images of tip-current of the rGO-sample; Blue and dark blue areas: electrochemical non-active areas; yellow and red areas: electrochemical active areas (rGO flakes), since the surface is able to reduce the oxidized form of the redox mediator.

evaporation of the electrolyte (increasing the redox mediator concentration) or by a change of the shear force unit SF-amplitude, resulting in a change of the distance between tip and surface. However, the response of the GO sample did not vary significantly in comparison to the response of the blank silicon wafer. The primary sp^3 hybridization of GO is the reason for it's insulating properties, hence the electrochemical activity was expected to be low [61].

The SECM measurements of the rGO-samples showed totaly different behaviour than both samples observed before. Blank areas, not covered with rGO result in electrochemically non-active areas and the measured tip-current for these was found from 150 to 200 pA (dark blue area in figure 3.7e&f). For these spots the result is the same as the results from the blank and the GO sample. Significantly higher tip-currents of about 400 - 650 pA were measured in areas overlapping with the rGO surface coverage observed by SEM (figure 3.6c) and are shown as the yellow and red areas in the SECM data in figure 3.7e&f. The highest current of 650 pA was recorded when the tip electrode surface was positioned completely over a rGO flake.

For the case, when the tip electrode covers only a portion of the underlying rGO flake, smaller currents were measured, corresponding to the average over the whole electrode. Depending on the observed area, the current was found from 150 pA for non-electrochemical-active areas (no rGO) up to 650 pA for electrochemically active spots (rGO flakes). The electrochemical active areas indicate successfull reduction of the rGO and good conductivity because the surface is able to reduce the redox mediator. Therefore, SECM is able to provide information about the rGO surface coverage and the rGO reduction success at the same time for large areas.

Evaluation of the FET Applicability using SECM Data

To validate the FET device selection protocol derived in chapter 3.4.1, the data from the SECM measurements was used. The distribution of the electrochemical active areas from the measurement of the rGO surface was cut into slices of 50 μm to demonstrate the contact behaviour if applied in a FET channel of the used geometry. Thereby the functionality and reproducibility of the rGO-FETs, which depends on the contact of Source-Drain via rGO was evaluated and the FET device selection procedure confirmed to be effective. At the same time this approach should prove the statistical balancing of the rGO distribution in the FET channel when using 4 mm long electrodes [1]. A visualization of this approach is given by a presentation of SECM data with graphical illustration of the electrodes and channel contacts and is shown in figure 3.8.

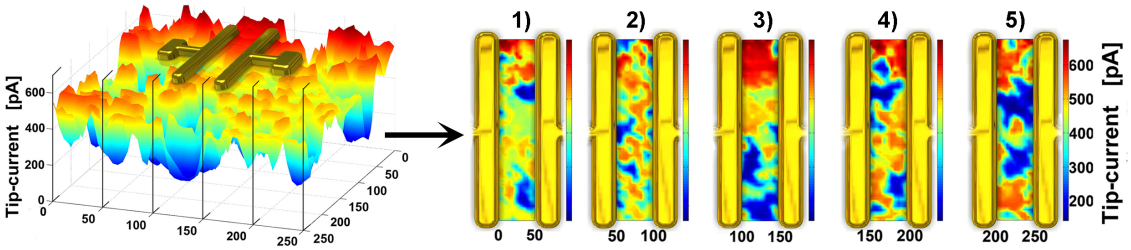

Figure 3.8: Five, equal-sized, parallel slices of 3D SECM data of a rGO sample with indicated Au electrodes on the edges of the slices for evaluation of the functionality of the rGO-FETs. The evaluated coverage density matches for slice 1: 79 %; slice 2: 74 %; slice 3: 64 %; slice 4: 67 %; slice 5: 57 %.

The slices measure 50 μm in width, which is close to the actually used channel width. The Source and Drain electrodes are fully connected by the electrochemically active area, hence electrical contact is provided. Five channels of the rGO-FET were cut out in order to calculate the sufficiency for conduction of the channel by the

electrochemically activite areas obtained by random graphene distribution. Areas with currents of $\geq$ 400 pA were defined as electrochemically active, resulting from comparison with the data of unreduced GO. The coverage density of electrochemically active areas was calculated via Mathlab (Mathworks, 7.13, R2011b), obtaining results for the surface coverage of the five slices: 79 % (slice 1), 74 % (slice 2), 64 % (slice 3), 67 % (slice 4) and 57 % (slice 5). It can be concluded that the rGO coverage density of 68 $\pm$ 7 % provides a very high probability of rGO electrical contact through the FET channel. Hence it has been demonstrated that the provided approach using long FET channels to balance to statistical variation of GO distribution and the described FET selection provide reproducible and applicable devices.

3.5 Calculations for the Graphene Field Effect Transistor

Although a lot of research on graphene was reported in the last years, only few work had been accomplished in combining theory and experimental results, especially in the field of graphene FET devices used as biosensors. Lacking a theoretical formulation for quantitative data analysis of the experimental results and a missing transformation of the established transistor theories to graphene FETs in the literature triggered our interest in presenting a mathematical approach in this work. The lack of theoretical models for graphene sensors leads to discrepancies of experimental studies, e.g. studies showed that CVD graphene transistors are insensitive to pH changes [188], yet other studies reported otherwise [110]. Despite the fact that a wide variety of biosensor devices based on graphene have been developed and optimized, the basic requirements for the construction of an applicable biosensor (reproducibility, a routine for signal prognosis and easy handling) have not been studied in detail so far. The following subsections present the methods used for the theoretical disquisition in chapter 4.

3.5.1 Calculation of the Source-Drain Current

For the calculation of I_D, firstly characteristic I_DV_G curves were investigated. As typical for rGO-FETs, all devices display ambipolar behaviour, with an almost linear slope for both charge carrier types below $\pm$ 1 V_G (figure 3.9).

Because the charge carrier mobility (μ) is an important material parameter which for further studies can be used to calculate I_D mathematically, it was determined by using the linear regime in the I_DV_G curves. This is possible because the mobility can be evaluated by the application of an external field, which corresponds to an Gate voltage. According to [189] the mobility can be determined from the responses in I_DV_G curves by the following equation:

$$\mu = \frac{1}{\alpha e}\frac{d\sigma}{dV} \tag{3.1}$$

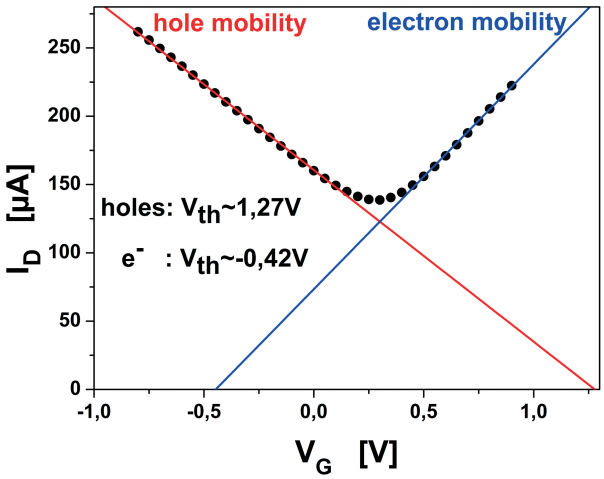

Figure 3.9: I_DV_G graph measured from -0.8 V to 0.7 V. Colored lines indicate fits for the linear regimes of holes and electrons respectively with intercepts defining V_{th}. Dirac Voltage is found around 0.3 V. [1]

where α is the induced carrier density by change of V_G for 1 V and e is the electron charge. For the linear parts in the I_DV_G curves the mobility can be calculated by equation 3.2, inserting the slopes as m_{lin} obtained by equation 3.1 using a similar approach as Tanaka et al. [189]. Then the electron and hole mobilities are obtained after the consideration of the devices properties and parameters, which can differ for fabricated FETs, therefore also the channel geometry has to be taken into account. From these considerations the following equation can be obtained:

$$\mu_{\text{eff}} = m_{\text{lin}} \frac{L}{W V_D C_i} \tag{3.2}$$

with m_{lin} being the slope obtained from the linear fits as described above, W and L are the channel width and channel length respectively. V_D is the Source-Drain voltage used for the observed I_DV_G curve and C_i the Gate insulator capacitance per unit area. The charge carrier mobility was calculated for FETs fabricated using the described protocols and was measured in the range from 10 000 to 50 000 cm^2/Vs for electrons, with relatively high variations depending on the fabricated FET batch. However, the obtained values are relatively high in comparison to other values from literature using rGO. The hole mobility was obtained in the same manner and measured from 7 000 to 30 000 cm^2/Vs, the values being always a little lower than for the electron mobility of the same FET. This indicates slight p-type behaviour of the FETs, which can originate from impurities obtained during the synthesis of the

graphene. In average the results are very consistent with data of other high mobility FETs that have been presented in another work on rGO-graphene [190]. Knowing the charge mobility, it is possible to obtain equations for I_D and electron density for both charge carrier types seperately using approaches used in MOSFET theory.

Furthermore, the threshold voltage (V_{th}) had to be defined for ambipolar devices. In standard MOSFET theory there is no ambipolar behaviour, therefore the definitions of the V_{th}, classically being defined the voltage at which the FET turns on, can't be used for graphene based FETs because the FET never is turned off. To solve this problem, a routine for the definition of the V_{th} of ambipolar devices had to be defined and therefore the branches in the characteristic I_DV_G curves were used, choosing the intercept of the linear fit with the voltage axis (figure 3.9). This leads to the voltage at which theoretically the FET would be turned off, although that state is not possible to achieve in reality. Nevertheless, two separate V_{th} are found for a single I_DV_G curve, which then has to be used for the calculation of the corresponding electron or hole mobility. The same approach is used for the formulation of the current in the linear model for metal-oxide FETs (MOSFETs) [191], where it is defined on the basis of the I_DV_D diagram, which would not be possible for a graphene based ambipolar FET. In this work the same calculation routine was transformed in such manner that it is applicable for the I_DV_G curve instead of I_DV_D which doesn't change any obtained values or their dimensions, but yields calculations of channel resistance a priori. For detailed calculation and adjustment to the structure of the FET used in this work, the oxide layer capacitance had to be replaced with the electrolyte capacitance due to the same effect in liquid-gated transistors of the electrolyte than in MOSFETs for the oxide layer capacitance. The electrolyte capacitance has to be considered a variable, because it can change during experiments, depending on liquid gate isolator properties which at the same time is the matrix of the measured analyte. The applicability of the approach was tested by measurements of I_D and comparison to the calculated and expected values and thereby was successfully confirmed. As explained before, the procedure for the calculation of I_D has to consider two cases, one for the more positive and one for the more negative voltages than the Dirac point voltage. The formulation for I_D, depending on the V_G, has to take into account the corresponding regime for either hole or electron charge carriers and their corresponding V_{th}. From these considerations it can be seen that the developed theory will not be accurate for results measured for V_G very close to the Dirac-Point. The oxide layer capacitance was replaced by the

electrolyte's capacitance and the relative permittivity of the electrolyte is a parameter needed for the calcluation of the capacitance. Because relatively low analyte concentrations were used for all experiments in the scope of this thesis, no change of viscosity, pH or ionic strength due to different analytes are expected. Therefore, the named parameters are considered to be constant for a single experiment and have not been implemented in the equation for I_D. For further studies it might be an advantage to also consider pH and ionic changes in the calculation, because only then the responses for different matrix types can be mathematically considered. The relative permittivity of an electrolyte can vary strongly depending on ionic strength, measurement frequency, temperature and viscosity and can range from 70 to 80 [127]. For the calculations in this work, the permittivity was estimated as 80 because the experimental settings fit best to this value as seen in the corresponding literature. Considering the equation taken from the MOSFET theory in the linear model and modifying it to satisfy the considerations of V_{th}, the liquids permittivity and capacitance for a PBS buffer with 170 mM total ionic strength and pH of 7.4, we obtain an equation for I_D at constant potentials:

$$I_D = \mu C_{ox} \frac{W}{L} (V_G - V_{th}) V_D \tag{3.3}$$

For oxide layer capacitance (C_{ox}) the capacitance of the interface from ionic liquid to the graphene surface was used, corresponding to 3 $\mu F/cm^2$, as shown in literature [192]. The capacitance which is observed (C_{obs}) can be split into partial capacitances in the following manner: $1/C_{obs} = 1/C_H + 1/C_{diff}$, where C_H is the Helmholtz layer capacitance and C_{diff} the diffuse double layer capacitance [193]. In total they yield the inverse additive of the observed capacitance which has to be used for the calculation instead of the C_{ox}, since no oxide layer is given in the measurement setup. Therefore, both capacitances used in the MOSFET system are reduced to a single capacitance of the electrolyte. This procedure allows for the use of the Grahame theory on the EDL as described in 1.3.2. Anyhow, the cases of the dependency of the total capaciatances can be split for different ionic strength, where at low electrolyte concentrations C_{diff} is lowered and C_{obs} becomes approximately equal to C_{diff} ($C_{obs} \simeq C_{diff}$). For high ionic concentrations C_{obs} is very close to C_H because C_{diff} becomes so high that the reciprocal value can be neglected. PBS buffers were used as electrolyte due to it's small solvated ionic radius and low viscosity, which remain constant throughout the experiments. The dissociated ion concentra-

tion remains the only variable with influence on the EDL capacitance due to the associated dielectric constant, which is varying with this factor. In an experimental check-up of at least 5 FET devices the channel current baseline level was in good correspondence with the calculations from equation 3.3. An average error of 2 % for the linear regime and an increased error if V_G is closer to the Dirac Voltage than 0.3 V due to the nonlinearity in this region were found. The highest deviations of devices measured for their baseline to the theoretical results have still been less than 10 %, which clearly underlines the applicability of equation 3.3. The accuracy of this equation was checked on devices measured at different V_G to demonstrate the range of applicability when changing V_G. For all calculations V_{th} were obtained from the $I_D V_G$ diagrams first, which had to be measured beforehand from the intercept in e.g. figure 3.9.

3.5.2 Protein Adsorption/Desorption Kinetics

The response signal ΔI_D from a binding event depends linearly on the surface coverage of the observed analyte bound to the binding sites at the graphene surface. The Langmuir formulation, which in detail is explained in chapter 1.4.1, can be transformed to ΔI_D and used for analysis of binding events. Hence a mathematical expression for the system can be obtained when binding constants are known or obtained from titration experiments [194]. Therefore the determination of unknown target molecule concentrations can be theoretically performed in advance or for comparison with obtained experimental results if a suitable equation with good accuracy is given by combination of the Langmuir binding kinetics and equation 3.3. The following equation for the channel current is thus derived and stated as followed:

$$I_{DS} = \mu C_{ox} \frac{W}{L}(V_{GS} - V_{th})V_{DS} + \theta(pH)(\frac{k_{on}[c]R_{max}}{k_{on}[c] + k_{off}})(1 - e^{-(k_{on}[c]+k_{off})t}) \quad (3.4)$$

with R_{max} being the maximum response signal, [c] the observed analyte concentration and θ(pH) the Heaviside-function determining the prefix defining if positive or negative detection signals are expected (θ(pH) being sign(pI - pH) for proteins, and (-1) for uncharged molecules). t defines the equilibrium setting time of the observed concentration, starting with 0 at injection. k_{on} and k_{off} are the affinity constants and are obtained from the linear fit in the Langmuir model. The formulation shows good agreement with experiments conducted on multiple FET devices, exhibiting a

maximum relative error of approximately 20 %. The drift of the baseline is not considered in this equation and the current is measured and compared to equation 3.4 after stabilization of the baseline to lower than drifts of 1 nA/s.

3.5.3 Theoretical Validation of the analytical Array Procedure

For the measurements in chapter 5.5 real-life samples and an array configuration are used. The validity of the simple approach for the subtraction of the response signals to obtain a readout of the response signal can be evaluated theoretically by using a general model for the electrostatic potential at electrolyte oxide interfaces [195]. Thereby the surface potential changes are ascribed to V_{th}, which can be measured from the $I_D V_G$ curves by linear extrapolation of the slopes for the negative and positive region (electron and hole mobilities) to the voltage corresponding to a hypothetical 0 A current flow through the FET channel. The model uses the corresponding equation proposed by Bergveld et al. [196], which states:

$$V_{th} = E_{ref} - \Psi_0 + \chi^{\mathrm{sol}} - \frac{\Phi_{\mathrm{Si}}}{q} - \frac{Q_{\mathrm{OX}} + Q_{\mathrm{SS}}}{C_{\mathrm{OX}}} - \frac{Q_{\mathrm{B}}}{C_{\mathrm{OX}}} + 2\phi_{\mathrm{f}} \tag{3.5}$$

where E_{ref} is the potential difference of the reference electrode, Ψ_0 is the electrostatic potential, χ^{sol} the surface dipole potential, Φ_{Si} is the silicon electron work function, q the elementary charge, C_{ox} the capacitance of the Gate oxide, Q_{OX} the charges in the oxide, Q_{SS} the charge of the surface states and Q_{B} the depletion charge. In the original publication ϕ_{f} describes the potential difference of the Fermi levels of doped and intrinsic silicon [195] because the model was developed using SiO_2 ion-sensitive FETs. It can be shown that the same relation works for other channel materials, essentially metal oxides. For the case of rGO-FETs, this potential difference could be ascribed to the Fermi levels of doped and neutral graphene sheets, keeping in mind that for rGO the synthesis and reduction process dope the surface with residues, shifting the Fermi level in comparison to e.g. CVD graphene. Interestingly for this equation, most factors are constant for a specific electrolyte used. To interpret the simple approach of subtraction of the response signals of two FETs in array configuration, expression 3.5 can be simplified because the FETs are compared using the same solution - the corn matrix - under the assumption that the variable AfB1

concentrations are not altering the solution's basic properties. Therefore E_{ref}, Φ_{Si}, Q_{OX}, Q_{SS} and Q_B can be seen as constants. Using the mathematical approach $|I_{D1} - I_{D2}|$ for the array, the formulation for I_D in equation 3.4 and substituting V_{th} with the expression in equation 3.5 after calculation of the resulting $|I_{D1} - I_{D2}| = \Delta I_D$ the following relation is obtained:

$$\Delta I_D = |2{\phi_f}^{(1)} - {\Psi_0}^{(1)} + {\chi^{sol}}^{(1)} - 2{\phi_f}^{(2)} + {\Psi_0}^{(2)} - {\chi^{sol}}^{(2)}| \tag{3.6}$$

The three factors that are left after subtraction of the I_D's are the only differing variables for both FETs in the array (the numbers in superscript in formulation 3.6 indicate the corresonding device 1 or 2 in the array). The difference of Fermi energy ϕ_f is depending on the doping of the surface, which in fact can differ for two FETs, because of the manual fabrication process in this work. A routine to adjust ϕ_f for all fabricated transistors to the same potential could be achieved by directed doping of the surface after the fabrication process. The same applies to the surface dipole potentials χ^{sol}, which also are not constant for two different devices. When measuring in array configuration with two FETs, the normalization of the curves for a given blank corn extract induces the correction of the differing χ^{sol} and ϕ_f, because the electrostatic potential Ψ_0 for the same electrolyte without any surface binding to antibodies is constant for both devices. Therefore the dipole potential and ϕ_f are the only variable factors for the reference solution (blank corn extract). The difference in these variables is evened out by the multiplication of the non-targeted FETs response curve with any constant which modifies the curve in such a way that $\Delta I_{D1} = \Delta I_{D2}$. This leads to $|I_{D1} - I_{D2}| = 0$ for the reference solution. When normalization is performed in this manner, it will be shown later that $|I_{D1} - I_{D2}| = 0$ also for other non-contaminated food samples used in this work.

Therefore $|I_{D1} - I_{D2}| > 0$ only when binding to either the target or non-target antibody is occurring. During specific detection of AfB1 from corn extracts, the used corn matrices can be of different nature, because the used corn samples in this work were naturally contaminated and therefore origin from different plants and crops. Nevertheless ϕ_f is a material parameter which is independent of the used analyte and is evened out by the normalization routine described above and can therefore be seen as a constant after normalization. χ^{sol} changes for different corn extracts and may vary for different concentrations, but because one observation is performed only for a certain corn matrix for one concentration at a time, the surface dipole

potential is assumed to be constant, which simplifies equation 3.6 to:

$$\Delta I_D = \Delta I_{D(non-target)} - \Delta I_{D(target)} = c(\Delta {\Psi_0}^{(1)} - \Delta {\Psi_0}^{(2)}) + \beta \tag{3.7}$$

where β is the Langmuir-like last term in equation 3.4, which turns to 0 for the non-targeted FET and is concentration dependant for the targeted FET. The factor c is a scalar constant obtained from all non-variable factors and Ψ_0 is the surface potential, which can be influenced by binding events at surface immobilized antibodies as explained in chapter 4.6.1. Therefore the observed difference in response signals for the targeted and non-targeted FET devices in array configuration is defined by equation 3.7, with the binding term β and the surface potential Ψ_0 as convoluted variables. Under the assumption of $\Psi_0 << \beta$, the equation can be further simplified and yield results that are interpretable by the Langmuir binding theory.

Chapter 4

Measurements in buffered Solutions

4.1 Introduction

The presented graphene FETs were partly developed in my diploma thesis [135] and are the basis for the characterization and applications performed in this work. Some basic characterization, particularly ionic strength dependence, protein detection and pH responses have been studied before and the basic measurements are not shown in this work, although they are fundamental for the presented research. Nevertheless all measurements shown in this chapter are based on or are derived from measurements previously done. The presented results were also published in *Graphene-based liquid-gated field effect transistor for biosensing: Theory and Experiments* [1] and are discussed here in more detail.

4.2 Dependency of the Charge Mobility on pH

For $I_D V_G$ curves of solutions having different pH, a shift of the Dirac point and a change of the slopes for electron and hole mobility can be observed. Titration curves and $I_D V_G$ relations were measured with PBS buffers with pH values varying from 6 to 7 and at constant ionic strength in [1, 135]. These results were confirmed and are shown in figure 4.1a. The similarity to the response curves obtained for measurements performed earlier in [135] is very high, although the responses are

found at 5.8 μA for a pH change from 6 to 7, which differs to 0.3 μA from the previous experiment. Again, steps of ΔpH = 0.1 were chosen for the reproduction, keeping all other system parameters constant and equal to the results shown in [1]. pH titrations with a range from pH4 to pH8 in steps of Δ pH = 0.5 were also shown in that work and are displayed in figure 4.1b. The derived equations for the calculation of the electron and hole mobilities were applied for these $I_D V_G$ curves separately, fitting the linear regime. From m_{lin} obtained by the linear fits in the branches aside of the current minimum the electron and hole mobility of the underlying rGO layer for varying pH have been calculated. This in turn gives information about the graphene-liquid interface and the interactions of liquids with the graphene itself. The responses of a graphene FET for changes of pH can result from two different effects. Firstly the formation of the EDL, which for the solutions with different pH can change the surface charge at the graphene-liquid interface and hence change the mobilities of the electron cloud, which is the nearest neighbour to the charged Holmholtz layer at the interface. Secondly, also the effect of intercalations as explained in chapter 1.1.3 of the introduction can change the FET conductivity. The intercalated water layer between two layers of graphene is also part of the electric circuit which electrons have to pass when travelling from Source to Drain if any overlaps of multiple graphene layers are given on their path. In that case a given electron would have to tunnel from one graphene flake to the other, which is easier if the interspacing of two flakes is lower or the intercalated water layer has higher conductivity due to increased ionic strength. Since the ionic strength of the used solutions is constant, only a change in distance of two overlapping flakes could result in a change of conductivity. This effect could be induced by a change of the pH value due to the electrostatic forces of two overlapping graphene flakes might be changed with respect to the pH of the intercalating solution. This would also change the Zeta potential and therefore the potential and hence the interlayer distance. The experimental study of this effect was conducted by a detailed analysis of pH values from 6 to 7, obtaining titration curves, which are shown in figure 4.1a. Again exponential fits were applied for the kinetic parameters of each pH step's time dependent change to evaluate the influence of the curvature of pH titrations. The exponential fits show consistent behaviour, in that regard that for changes of ΔpH = 0.1 the same coefficients have been found as for changes of ΔpH = 0.15 as shown in the insert in figure 4.1a. Furthermore also for changes of ΔpH = 0.5 the fits applied had constant exponential factors for all pH changes. The interpretation of this effect can be easily performed when assuming

the time-dependent build-up of a Gouy-Chapman diffuse EDL at the surface when the pH is changed. The EDL is being established across the channel length with a reaction rate having constant k. This rate is depending on the length of the channel and the liquid flow speed, which determine the liquid exchange speed across the FET channel. Interestingly, the fitted exponential factors for pH changes seem to be dependent on the applied V_G and are contant for pH changes as long as the applied V_G is constant. An exact evaluation of this time-dependence to the applied potential still remains to be clarified.

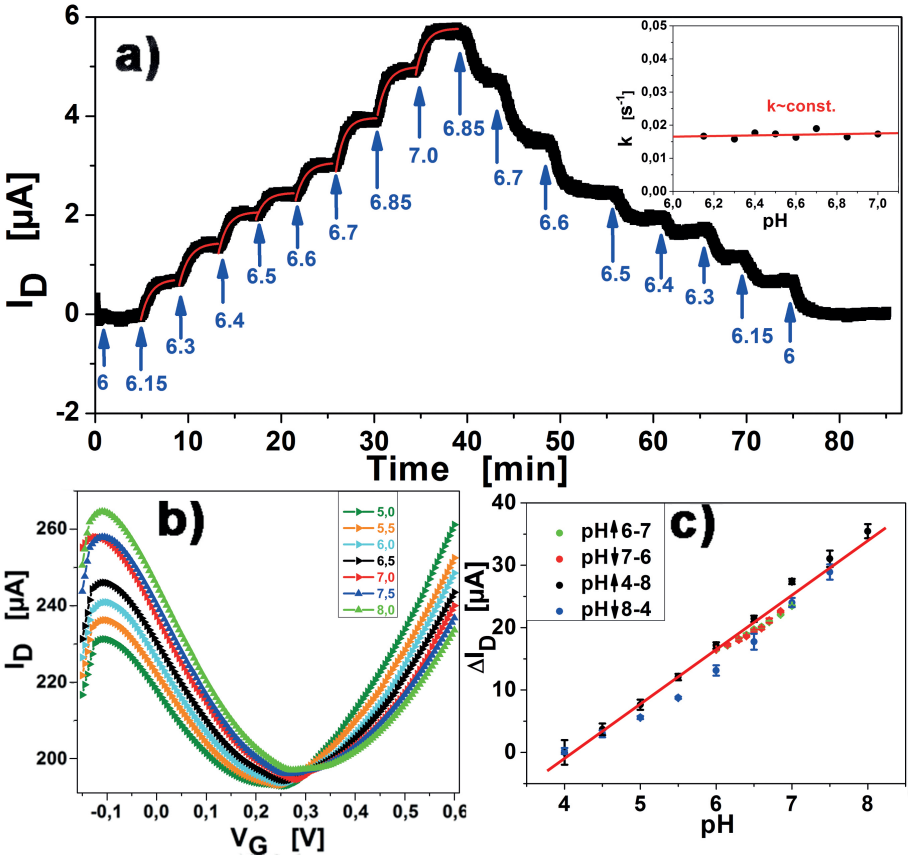

Figure 4.1: a) Titration of the pH of the buffer from pH 6 to pH 7 in steps of ΔpH = 0.1 and 0.15, showing reversibility of the measurements. Exponential fits (red lines) have been applied for each pH transition. The insert shows that the transition rates are constant for varying pH with an average value of k = 0.017. b) $I_D V_G$ curves for pH values in the range pH 5 - 8, in steps of ΔpH = 0.5. c) Regression of change in channel current with pH value of four different measurements normalized in such way that the response for pH = 4 was adjusted to 0 μA response. Arrows indicate if data was obtained from ascending or descending pH value titration. [1]

On the other hand, the linear relation of conductance and pH change was found to be 30 μS per pH, and the relations for four different measurements are all shown in

figure 4.1c where the responses have been normalized in such way that any given response to pH 4 (either really measured or interpolated) is normalized to 0 μA. The relation is indicating that the relative surface potential and the surface charge changes have a linear relation.
This relation is crucial for the success and applicability of any given rGO-FET because it is essential for the quantitative detection of biomolecules in variable matrices. The slope of 30 μS per pH is in good accordance with experimental results and theoretical considerations shown elsewhere [197]. The shift of the Dirac point of the I_DV_G diagrams for different pH values is also in good accordance to literature [193] and was confirmed with an offset from 0.175 V for pH 4 to 0.31 V for pH 8, corresponding to a dependency of 0.034 V/pH (figure 4.1b).

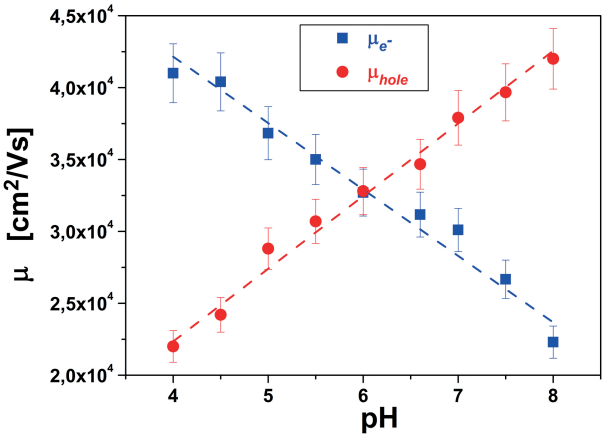

Figure 4.2: Charge carrier mobility for electrons and holes in dependence on the pH of the electrolyte. (Obtained from fits of I_DV_G measurement in figure 4.1b.) [1]

The mobilities of electrons and holes have been derived from fits of the I_DV_G relations and their dependence on the pH value is shown in figure 4.2. A transition of the majority charge carrier type from electrons to holes can be seen at around pH 6, meaning that below pH 6 electrons are the most prominent charge carriers and holes become more prominent above pH 6. From this fact a further intrinsic property of the rGO is obtained, showing the dependency of the charge carriers and conductivity of the material on the pH. It gives a good estimation at which pH n-type or p-type behaviour of the rGO-FETs is to be expected. Similar to the isoelectric point, which defines the charge of proteins depending on the matrix pH, an analogy for graphene is used and therefore the point is called "isomobility point" of rGO, which in our experiments is found to be around pH 6. Furthermore in these experiments

the corresponding current to the Dirac point was confirmed to be constant and independent of the pH. For other measurements of the ionic strength it could be shown that I_D is increased for higher ionic strength. At the same time the voltage of the Dirac point stays constant and the conductivity of the FET devices increases only slightly with increasing total ionic strength of the electrolyte.

The Debye-length λ_D of the system is depending on the ionic strength of the used electrolyte and defining the interactive radius of molecules in the medium and is defined by the thickness of the EDL. As stated by the Debye theory explained in chapter 1.3.1 an increase in ion concentration lowers the effective λ_D in the liquid. The EDL at the graphene-liquid interface is forming a stronger charge separation due to the increased ion concentration, which is resulting in a higher potential at the surface and also exhibits a stronger electrostatic force on charge carriers in the rGO. The direct consequence of an increase in the ionic strength therefore is a slight increase in charge carrier mobility, which again can be calculated using the procedure explained in this chapter.

4.3 Impedance Spectroscopy

Impedance spectroscopy is a powerful analytical tool, which can characterize the used graphene FETs, yielding further information about the transistors behaviour for a wide range of analytes and/or solutions. Apart from the information obtained by measurement in direct current (DC) mode, which is basically only the readout of the I_D, impedance spectroscopy delivers frequency dependent information about the resistance of the FETs. In contrast to DC measurements, the obtained dimension is the conductivity $|Z|$ of the FET, which can be used to calculate I_D via Ohm's law, but can have it's limitations if the leakage current to the Gate electrode isn't negligible. Here impedance spectroscopy was used as an additional characterization tool, to evaluate the responses of buffers with different ionic strengths. The analytical detection of analytes (AfB1) still was performed in DC measurements. Impedance spectroscopy rendered useful for the analysis of unknown responses from matrix effects, as shown in chapter 5, since it is possible to de-convolute signals from ionic strength change and adsorption to the graphene surface.

For a more detailed characterization of the FETs response to ionic strength changes

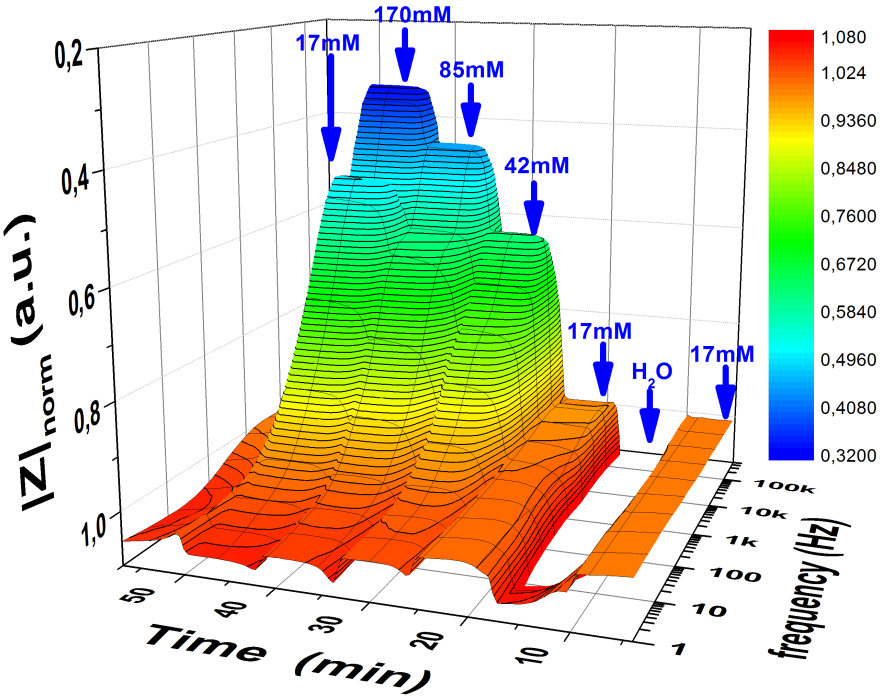

Figure 4.3: Result from the impedance spectroscopy of a blank rGO-FET, performing a titration of PBS buffers with pH 7.4 and ion strengths from 170 mM to 17 mM. The graph was normalized to the baseline obtained by the injection of 17 mM. Therefore the negative peek, resulting from the measurement of diH_2O, is not displayed in this figure.

in the used solution, a titration curve of PBS buffers with different ionic strengths was performed, analogously to the measurements in DC mode (shown in my diploma thesis [135]). Each buffer solution was washed over the sensor surface for 10 minutes, using total ionic strengths of 17, 42, 85 and 170 mM as well as diH_2O. An example for an impedance plot is shown in figure 4.3.

4.4 Application as microfluidic Flow-meter based on Graphene

During this work different response signals on rGO-FETs, depending on the flow rate of the liquid were observed. This observation was novel at the time of discovery, hence a patent was submitted and accepted for the method of flow velocity detection utilizing graphene FETs. The corresponding Patent ID is 14162292.8 [198]. Commercial flow-meters for very slow flow rates are only found in very high price ranges, however the fabrication of the presented FET based on wet-chemically produced graphene can measure and distinguish very slow flows down to at least 50 μm/sek (lower pump speed could not yet be tested). Several possible application areas could benefit from a price efficient and accurate measuring device for liquid flows (medicine, biosensing, lab equipment).

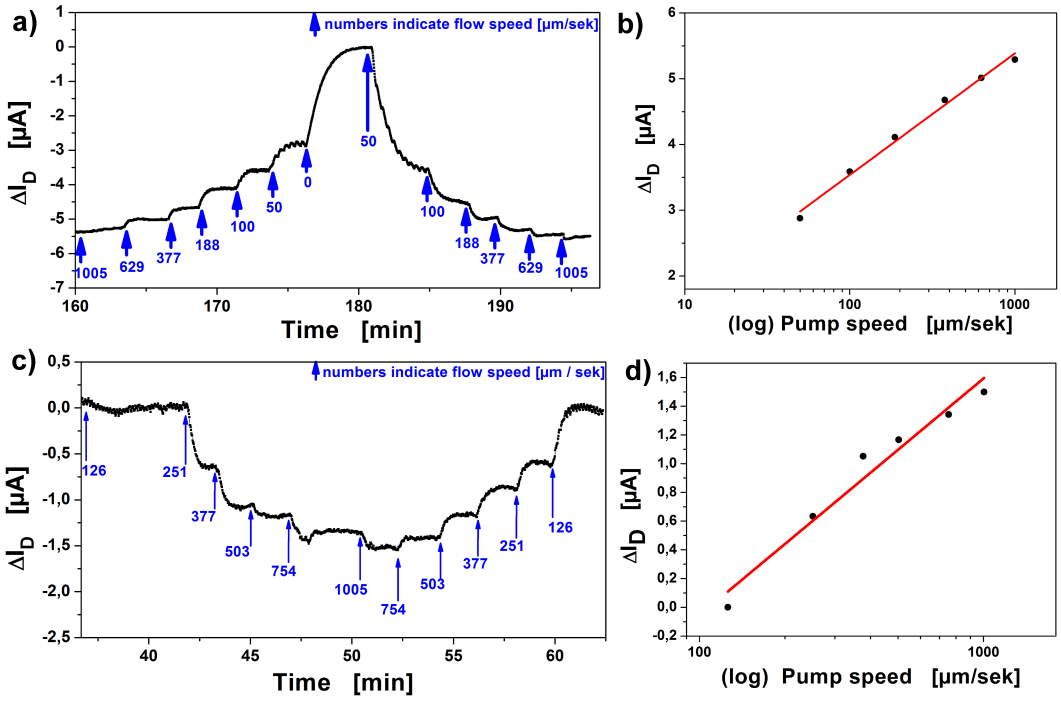

Figure 4.4: a) Measurement for low pump speeds. b) Logarithmic regression of the detection signal from figure a. c) Measurement for higher pump speed and d) the corresponding logarithmic regression of signal to pump speed for the measurement shown in figure c.

State-of-the-art flow-meter devices usually determine flow speed and/or mass transportation of high speed flows, ranging down to 500 μL/min, with geometries that require large amounts of sample liquid. The lowest measuring range of instruments

on the market is achieved by the technology of thermal mass flow meters, which measure down to 100 μL/min but are much more costly in production than the wet-chemical graphene FET devices. Furthermore, scientific work has been published by Newaz et al. [199] based on a CVD graphene FETs, but with the flow speed detection limit already at 4 mm/sek, while the FETs presented in this work can outperform that by a factor of 80. Additionally the CVD of graphene is more costly and requires bulky equipment, while wet-chemically synthesized graphene can be produced at very low cost with minimum equipment. Papers by Proctor et al. [200, 201], determining the basic effects of pressure on graphene can be seen as background for all following advancement and applications based on graphene-surface force interactions ("Graphene under hydrostatic pressure"). Also another patent was released in China by another group [202], but using graphite alkene and a different buildup for the determination of gas pressure and flow speeds.

The measurements were conducted at constant V_G using a Ismatec high Precision Multichannel Dispenser device for speed adjustment with step-by-step increasing of pump speed after a constant signal is detected for the previous speed step. Distilled water was used as transport medium. The relation between signal output (I_D) and flow speed was found to have exponential character. The Fit for this relation shows concordance between 96 % and 99 % when plotted on logarithmic scale.

4.5 Measurements of the Debye-length Dependency

For the detection of proteins in solutions various parameters like the variation in λ_D or changes in carrier mobilities induced by the electrolyte's ionic strength have to be considered. At low ionic concentrations in the electrolyte λ_D increases but at the same time the electron mobility and the double layer capacitance decrease, which in sum yields to a higher response signal of the system for the detection of BSA [1]. The titration curve obtained when using the ideal parameters for the detection of BSA is presented in the paper. Furthermore, the sole dependecy of the responses of any given analyte on λ_D is of interest. Therefore experiments with surface-immobilized anti-BSA were performed for the detection of BSA from PBS solutions with differing ionic strengths and the responses were compared with the theoretical curve from the Debye theory. The obtained experimental data from this study is in good agreement

with the Debye-theory for ion concentration variation and is presented in figure 4.5b. Since the λ_D can only be calculated with the correct capacitance and ionic strength, both factors have been considered variable and adjusted for the calculation of every response separately. The response signals for these measurements of 50 μM BSA injections have a dependency with a factor of 28.6 ± 2.9 nm/μA for the calculated λ_D in dependence on the surface potential. A fit of this relation is shown in figure 4.5b. Hence it can clearly be seen that λ_D influences the observed detection signals and protein detection has to be conducted in a suitable aqueous environment. For the experiments with BSA good system properties were found when using a buffer of pH 7.4, clearly above the isoelectric point (iP) of BSA, which is stated in literature at pH 5.4 [203]. The molecules are negatively charged for pH 7.4, which was chosen because of comparability to physiological conditions. The detection signals are then predicted to have a negative prefix and the signal response in PBS buffers, with changing ionic strengths was tested in such manner that a quantitative evaluation of the dependency of sensitivity on the corresponding λ_D variation is obtained.

The increase of total I_D with decreasing ionic strength (figure 4.5a) can be associated with the change of the capacitance in the EDL interface and the charge carrier density in the graphene, respectively. With lower ion concentrations, the charge mobility slightly decreases, but increasing the capacitance of the gate insulator plane generates a higher total current flow for voltages close to the Dirac Minimum in the I_DV_G plots (V_i). For higher voltage, V_G-V_i (further away from the Dirac voltage), the effect of charge mobility predominates the decrease in capacitance change and the total current increases with ionic strength of the electrolyte. The results from figure 4.5a have been superimposed with the calculated curve for the λ_D dependence on ionic strength from the Debye theory (figure 4.5b). For the λ_D calculation a variable capacitance and ionic strength have been considered. Following this procedure shows a good agreement of the calculated Debye curve characteristics with the measured experimental data for 50 μM BSA injections, linked by a factor of (28.6 ± 2.9) nm/μA.

The readout current can be written in form of the surface potential by simple use of Ohm's law, converting the current to the conductivity of the FET. The surface potential and surface charge are related and can be calculated from each other by use of the λ_D for known system parameters as stated in the Grahame equation (equation 1.9).

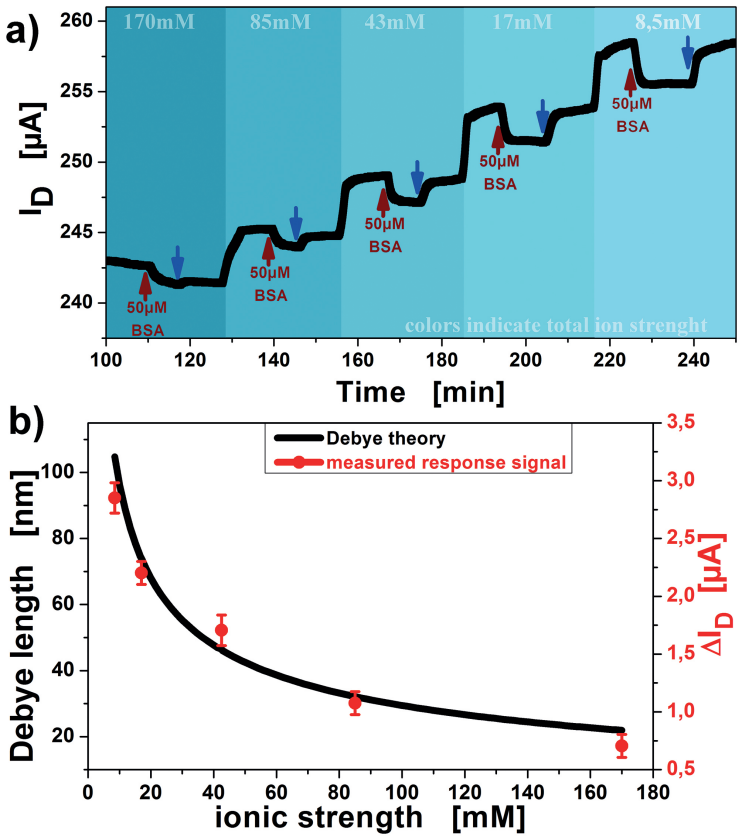

Figure 4.5: a) Measurement of detection signal behavior for 50 μM BSA, gradually decreasing the ionic strength (indicated by background color change) from 170 mM to 8.5 mM at V_G = -0.2 V. Blue arrows indicate rinsing with the same buffer solution used for the associated BSA injections. b) Overlap of responses from figure a) and the expected dependency calculated from the Debye-theory for electrolytes.

The relation can therefore be simplified for low potential cases (valid for the presented rGO-FETs) and leads to the equation:

$$\sigma = \frac{\epsilon\epsilon_0\Psi}{\lambda_D} \tag{4.1}$$

where σ is the surface charge, ϵ the dielectric constants, Ψ the surface potential and λ_D the Debye length. The simplicity of the equation for aqueous systems allows the calculation of the distance dependent potential normal to the surface. Furthermore it helps to understand the principle of signal transduction from biomolecules immobilized onto graphene surfaces with known distance to the graphene layer.

4.6 Biosensing of Aflatoxin B1

For the approach presented in this work, detection of AfB1 was performed using the corresponding AfB1 IgG antibodies which were immobilized to the graphene surface via pyrene chemistry (PBSE linker). AfB1 can interact or bind to the antibody either via hydrogen bonding or hydrophobic interactions [204]. Because of the charge neutrality of AfB1, a suitable V_G has to be used for the formation of an EDL. Charge displacement of that EDL at the protein during a binding event will then also interfere with the surface charge density and therefore modify the conductivity of the underlying graphene layer in such a manner, that a detection signal is obtained. The isoelectric point (pI) of the AfB1 antibody usually is found in the range of pH 6 to pH 7 [205, 206], therefore the used buffer solutions for the detection of AfB1 were adjusted to pH 8 with an addition of 1 % acetonitrile as solvent when measuring in buffer. In this case, the antibodies are negatively charged, which would point to the use of a positive V_G, since the EDL charge at the surface would then be positive and displaced more significantly for binding events or conformational changes of the antibodies at the surface. For the detailed characterization of the biosensor, studies on the dependency of the response signal on the ionic strength of the used buffer solution, the displacement of characteristic I_DV_G curves, the behaviour during a titration of low AfB1 concentrations and the non-specific interactions of AfB1 to the rGO layer are performed. Furthermore, the cross reactivity of the antibodies is studied, using four different types of antibodies and based on the results a supplier for the AfB1 antibody was chosen for all further experiments.

4.6.1 Basic Sensing Principles

As the first step for the detection of AfB1, IgG-antibodies supplied by Romer Labs® were immobilized with a concentration of 5 μM using the PBSE linker. Firstly, the suitability of the sensing platform was investigated by the injection of a fairly high AfB1 concentration (10 μM) during different ion concentrations of the corresponding matrix which in this case was a standard PBS buffer. The measurement was performed for increasing as well as decreasing ion strength to evaluate the system reversibility and dependency of an observed response signal on previous binding events. From these measurements, shown in figure 4.6 and figure 8.1, it can be seen

that high AfB1 concentrations like 10 μM can be detected in aqueous solution also for physiological ionic strength of 170 mM. However, the detection signal increases when the ionic strength of the used buffer is decreased due to the dependency on λ_D.

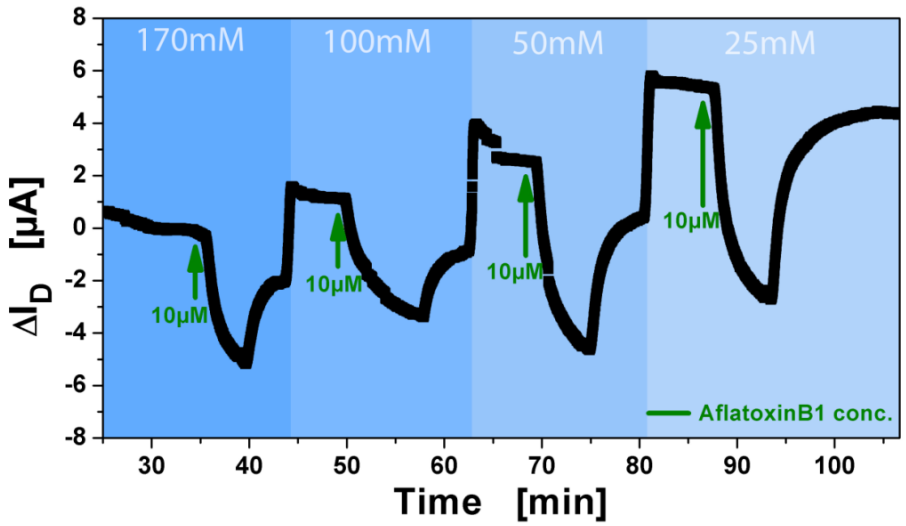

Figure 4.6: FET response curves for injections of 10 μM concentrations of AfB1 at different ionic strengths, which are indicated by the background colors and molar values. A higher detection signal was observed between 25 mM and 50 mM ionic strength, as expected due to a change of λ_D. The same measurement was performed for decreasing ionic strength and is shown in figure 8.1, reproducing the results and demonstrating the reversibility of the specific signal in regard to the ionic strength of the used electrolyte.

The responses of the FET to concentrations of 10 μM AfB1 were 5.5 μA at 170 mM ion strength, 5.2 μA at 100 mM, 7.4 μA at 50 mM and 9.2 μA at 25 mM. The decrease of the signal strength is in good correlation to the theoretically predicted results from the Debye equation for electrolytes. The exception of the response for the 170 mM solution (which is higher than expected) can be explained due to the high concentrations of AfB1. At this ionic strength surface saturation is already taking place and therefore the Debye theory is not applicable. The saturation at this high concentration is to be expected for the sensor surface but can further be adjusted using different V_G (a more detailed explanation follows).

The same measurements were performed for lower AfB1 concentrations of 100 nM with the same parameters as explained for the measurements shown in figure 4.6 and 8.1. Furthermore, a test experiment, adding 0.1 % of Tween®20 to the buffer solutions to test the change in graphene FET behaviour due to this compound was performed. Tween is widely used as a detergent to promote solubility of toxin dur-

ing the extraction of real-life samples [207, 208], for the inhibition of non-specific binding [209] or as an excipient to stabilize toxins in solution [210], while it does not affect protein activity. As result of the performed AfB1 titration, no change in transistor behaviour and characteristics could be observed for such low concentrations of Tween®20, indicating that no binding of Tween®20 to the graphene surface occurs (figure 4.7). Similar measurements were performed with Tween®20 concentrations up to 1 % in all solutions (figure 8.2). This experiment was performed to further demonstrate the influence of Tween®20 to the graphene surface and hence the channel conductivity. Apart from slightly worse baseline stability, no significant change in the FET behaviour was observed, independant of the Tween®20 concentration (comparison of figure 4.7 and figure 8.2).

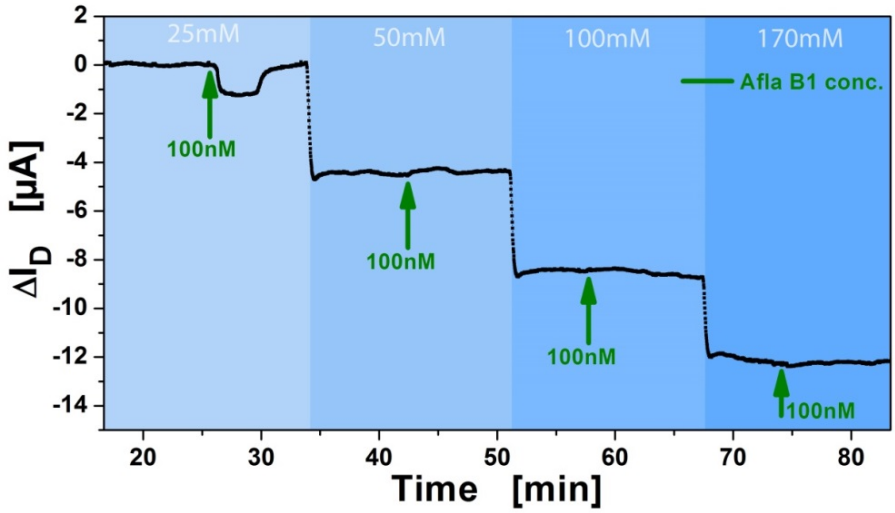

Figure 4.7: AfB1 detection in PBS buffers of variable ion strength with an addition of 0.1 % Tween®20 in all solutions. A low toxin concentration of 100 nM was chosen for proof of low LOD. A good response signal for nanomolar toxin concentrations was obtained only for PBS buffers with total ion strength of 25 mM.

Based on the results for the detection of AfB1 in PBS buffers of various ionic strengths and various concentrations of Tween®20, the standard buffer for the detection of AfB1 in aqueous solution was chosen to be PBS buffer with a total ionic concentration of 17 mM and 1 % of acetonitrile. Due to the fact that no influence of Tween®20 or acetonitrile at concentrations below 1 % were observed, Tween®20 was used for the measurements in real-life food samples, while acetonitrile was used for AfB1 detection in buffer solutions for easier handling. For further characterization of the binding affinity of AfB1 to the used antibody, $I_D V_G$ characteristics of the graphene FET were measured for different concentrations of AfB1 in the nanomo-

lar concentration range. Since a slight baseline drift was observed for almost all fabricated FET devices, the measured I_DV_G curves were normalized by the slope calculated from the linear baseline drift. Therefore the responses at 0 V were chosen as reference and the remaining part of the I_DV_G curves were normalized in such manner that the current at 0 V is not decreasing due to the baseline drift. From this measurement (figure 4.8) it can be seen that at the correct V_G, a detection limit in the low nanomolar or picomolar concentration range can be expected in a controlled environment using a buffered solution as matrix. Since the I_DV_G curves for different concentrations of AfB1 diverge at positive V_G, a positive V_G ideally higher than 0.4 V has to be used to obtain concentration dependent response signals during titration.

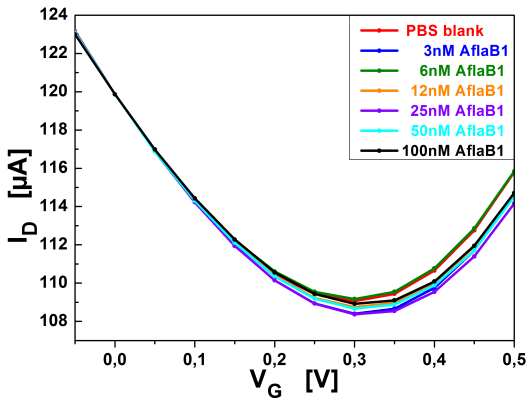

Figure 4.8: I_DV_G distinction of nanomolar AfB1 concentrations in dependence of V_G.

4.6.2 Evaluation of the Surface Binding Kinetics

Optimization of the binding kinetics following exactly the Langmuir theory was not the main focus of this work due to the fact that for the construction of the presented biosensor the LOD, the standard deviation of the data and the specificity have much higher impact on the applicability of the designed device than the binding affinity obtained from the Langmuir fitting procedure. Furthermore, a useful dependency of the response signal on the AfB1 concentration was observed only in the range of pico- and nanomolar AfB1 concentrations. For higher concentrations the response signal's signum changes and a complete Langmuir titration analysis is therefore not possible for AfB1 concentrations in the micromolar range. The region of concentrations having a viable dependency to the response for Langmuir theory fitting can

be altered almost linearly by changing the applied V_G. As shown in figure 4.8, the characteristic curves for different AfB1 concentrations have several crossing points which are defining the signum of the response signals during a titration experiment, depending on which V_G the experiment was performed. The signum of the response change will then be dependent on the concentration range of the supplied analyte during the I_Dt measurement. Therefore for different V_G also different saturation concentrations can be observed, depending on the magnitude of the analyte concentration and the signum of the responses. This FET behaviour was not seen as a limitation, since the concentration dependent detection of such high concentrations of AfB1 was not targeted in this work. The suitable areas for the assessment of a Langmuir titration curve are in the domain of 0.4 V_G up to 0.6 V_G for nanomolar up to micromolar concentrations. For negative V_G above -0.2 V, a difference in the characteristic curves for picomolar and nanomolar concentrations was observed, using a buffer with pH 8. However, Gate voltages above $\pm$ 0.6 V are not applicable due to high capacitative effects and leakage currents which increase the noise level for several magnitudes. They also impair the stability of the immobilized antibodies which can have disturbed functionality when exposed to high voltage potentials. The variations for negative V_G aren't depicted in figure 4.8 due to the correction of the baseline drift and the graph selection. The initial point for the baseline correction was chosen at 0 V_G because the detection of AfB1 should lead to displacement of the curves at positive voltges. When using buffers with pH higher than the pI of the antibody, detection is theoretically expected to be more effective when using positive V_G. However, this turned out to be true for nanomolar and micromolar concentrations, but for the detection of even lower concentrations down to picomolar concentrations, negative V_G promoted the linearity of the response signals and was used for the assessment of the LOD in buffer, which can be seen in figure 4.9a where the lowest detectable concentration is 33 pM.

Different titration curves of AfB1 binding to surface immobilized antibodies were measured and an evaluation of the affinity constant was obtained by the titration of five different concentrations, starting with low picomolar concentrations up to the 10 nM of AfB1 while using a V_G of -200 mV.

The fit of the k_{off} in the time-dependent measurement after the titration (rinsing step) corresponds well to the k_{off} obtained from the linear fitting procedure ($1.1x10^{-2}$), which is a good indication for the fitting consistency and accuracy. The

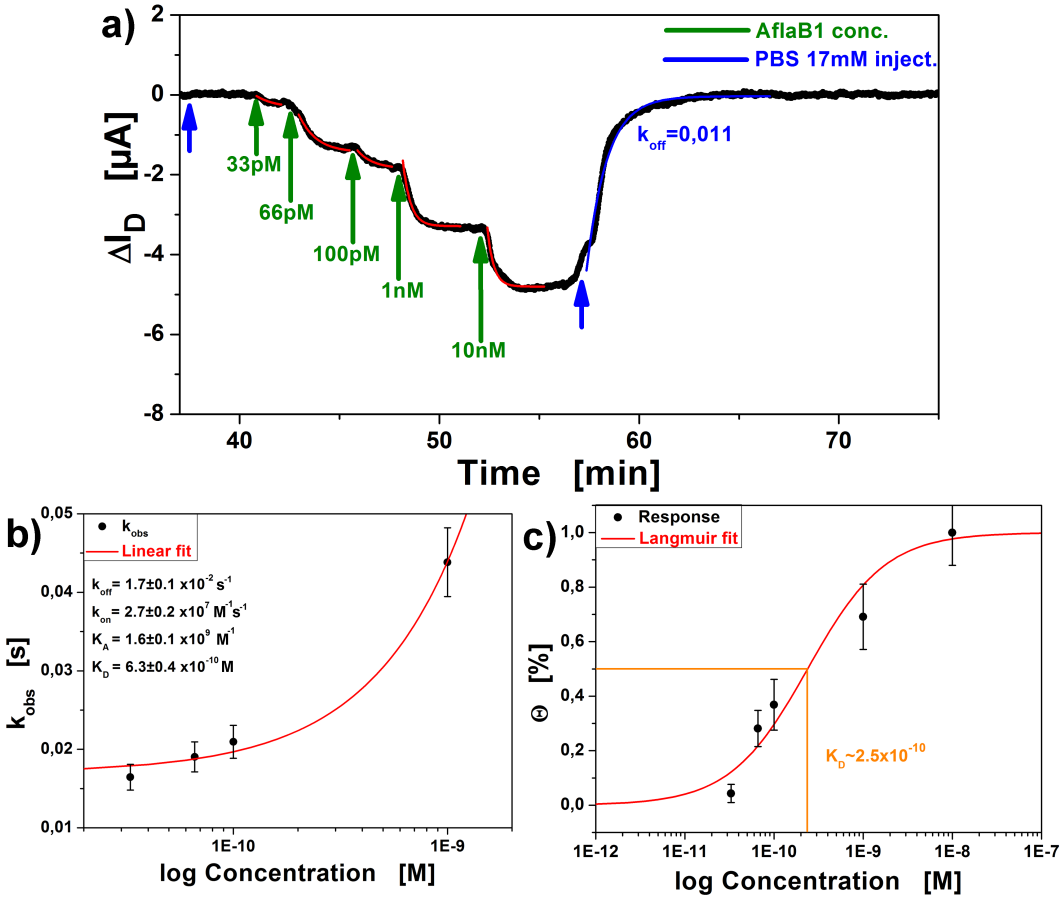

Figure 4.9: a) Titration of AfB1 with fitted binding parameters k_{obs}. Figures b) and c) below show the analysis of the obtained parameters and fitting corresponding to the Langmuir theory. b) The binding affinity obtained from the linear relation of k_{obs} to the concentration was found to be 630 pM. For better illustration of the measured data the concentration scale is shown in a logarithmic scale. c) The result for the binding constant K_D from the relation of response signal to concentration was found at 250 pM. The result was normalized to 1 for the highest concentration and plotted as the surface coverage of the graphene FET according to Langmuir binding. The IC_{50} concentration is marked by the orange line.

obtained binding constants K_D from both fitting procedures are in the same magnitude, being 250 pM and 630 pM which again is a good indication for the validity of the results obtained from the titration of AfB1.

Literature values for the affinity constants were compared to the results obtained in this work. As shown by Li et al. [204], the IC_{50} values for AfB1 antibodies produced by different methods, using different antibodies (monoclonal or polyclonal) can range over the order of three magnitudes, from 4 pM up to 7 nM. Since the IC_{50} values were obtained in the same way as the binding affinity K_D, when not analysing the kinetic interactions, both factors are comparable. The obtained binding affin-

ity from figure 4.9, being approximately 0.5 nM is in the same range as shown in publications using different analytical methods and matches the range described by Li et al. [204]. The obtained LOD of around 33 pM can be compared to the data of other electronic methods for measurements of AfB1 in a controlled environment like PBS buffer. A liquid-gated FET based on silicon nanowires has demonstrated a LOD of 3.2 nM [170], a fluorometric immunoaffinity biosensor showed a LOD of 320 pM [169] and a photosensitive silicon photodiode FET a LOD of 16 nM [211].

4.6.3 Unspecific Binding

Measurements for the evaluation of unspecific binding were performed, because an interaction of AfB1 with the bare graphene surface is possible. For a good comparability with the specific measurements shown above, a non-targeted antibody was immobilized on the graphene instead of the specific anti-AfB1. Because of the comparable size (anti-AfB1 size is around 150 kDa, while the anti-BSA is around 69 kDa), properties and availability, BSA antibodies were chosen for those experiments. Nanomolar concentrations of AfB1 were washed over the anti-BSA immobilized surface and the response signal was measured using the same buffer and FET parameters as for the specific detection. A representative curve from these experiments is shown in figure 4.10.

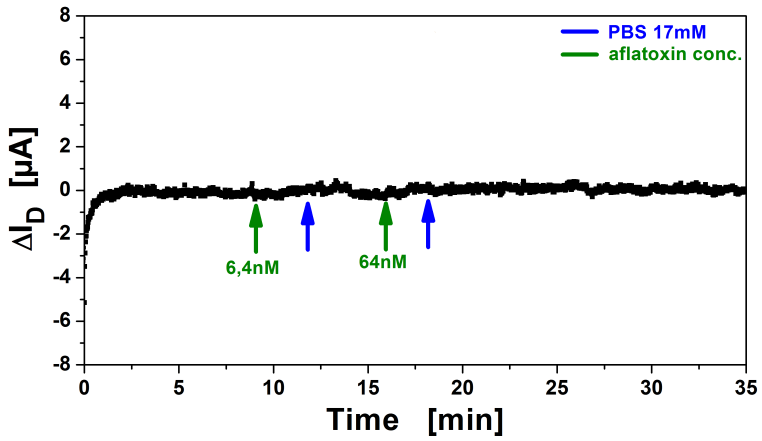

Figure 4.10: The unspecific responses for AfB1 were measured on graphene FET's with immobilized PBSE-linker and BSA antibodies. For all tested devices no response signal was observed, indicating that no binding of AfB1 to the graphene surface, linker or non-targeted antibody is occurring.

The same measurements were performed beforehand, using only the bare graphene surface with no linker or antibody and results from these measurements show signif-

icant binding of AfB1 to the graphene surface. These results are shown in figure 8.3. However, these measurements are not representative, since the surface structure differs from the specific case and the unspecific signals from aflatoxins binding on the graphene surface are expected to be further minimized when a linker and antibody are used. The pyrene $\pi - \pi$ stacking of the PBSE linker to the graphene during the formation of a self-assembly monolayer can protect the surface from molecules binding, as stated in literature [212]. When using non-targeted antibodies (BSA), the binding was diminished in comparison to bare graphene as well as to the detection with immobilized aflatoxin antibody. Hence a shielding effect of the linker has to be supposed, which would fulfil the Debye-Hückel law [213] by lowered total charge and therefore increased relative λ_D from the graphene surface. Furthermore, a foresighted view of this work implies that a passivation of the surface has to be developed anyhow, since the measurement in real-life samples most definitely will include compounds that evoke non-specific signals as a result of the interaction to the graphene surface. Hence a detailed analysis of AfB1 binding to the graphene surface is not needed.

4.6.4 Cross-reactivity

The cross-reactivity and specificity of a biosensor are crucial properties for the applicability of an in-field biosensing device. For the graphene FETs used in this work, these factors mainly depend on the antibody used for the sensing experiments. Firstly, an antibody supplied by the cooperation partner Romer Labs® was used for sensing experiments in buffer solutions. Before measurements in real-life samples like corn extracts can be conducted, a validation of the sensor specificity has to be performed. At first this was done using the supplied antibodies by Romer Labs®. Five different toxins were tested which all are common for grains. Deoxynivalenol also known as vomitoxin and zearalenone also known as F-2 mycotoxin are commonly found in corn, rye and barley and are some of the widest spread toxins and most hazardous to health of live stock and consequently humans. Ocratoxin A is also one of the most common toxins and is found in a very wide range of foodstuffs including wine, coffee, peppers etc. Aflatoxin B2, just like AfB1 are produced by the same species of fungi and therefore are found contaminating the same plants. Furthermore aflatoxin B2 has a very similar structure as AfB1 (only one double-bond difference) and is assumed to have the highest potential for cross-reactivity to

the immobilized antibodies.

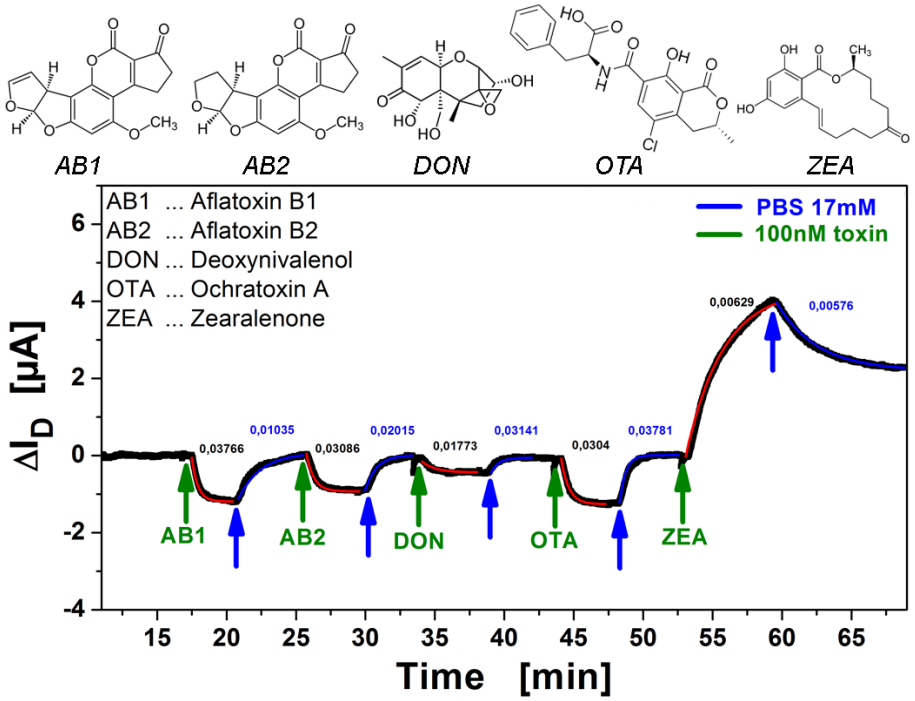

Figure 4.11: Cross selectivity of the antibody used for the measurements in buffer. This experiment was performed in buffer with 100 nM toxin concentrations for any of the tested toxins. The antibody shows very low specificity, having the strongest affinity constants for AfB1, aflatoxin B2 and deoxynivalenol. The structures of the used toxins are shown on the top of the figure.

The first measurements of the cross-reactivity of the antibody supplied by Romer Labs® and the observed kinetic constants as well as the chemical structures of the used toxins are shown in figure 4.11. It can clearly be seen that the used antibody is not suitable for specific detection from real-life samples. Therefore a chromatographic pre-step of the antibody was performed in forefront and showed that only around one third of the used material correspond to the molecular sizes expected for this type of antibody. Therefore the antibody was purified using a magnetic bead-based purification kit from Thermo Fisher and after purification another chromatography showed that approximately 60 % of the used material is in the size-range of antibodies after the purification (see figure 8.6 in the appendix). The same cross-reactivity measurements as shown for the non-purified antibodies were then conducted using the purified antibodies. The purification of the Romer Labs®-supplied antibody slightly increased the selectivity, but still showed a cross-reactivity to aflatoxin B2 of around 70 %. The high affinity of the non-purified antibody to zearalenone was diminished after purification to approximately half of

the initial signal and the affinity to deoxynivalenol was completely cleared. The affinities of all different toxins were evaluated by exponential fitting of the binding and wash-off curves and the results are shown by the numbers next to the corresponding injections in figure 4.11. The obtained values still show the highest affinity for AfB1 (0.038), slightly lower affinities for aflatoxin B2 and ochratoxin A (0.031 and 0.030) and the lowest affinities for deoxynivalenol and zearalenone (0.018 and 0.006). However, the cross-selectivity was still not seen to be sufficient for the fabrication of an useful biosensor, because the obtained responses in a more complex sample should be ascribed to a single specific toxin for proper evaluation of the contamination of the food samples.

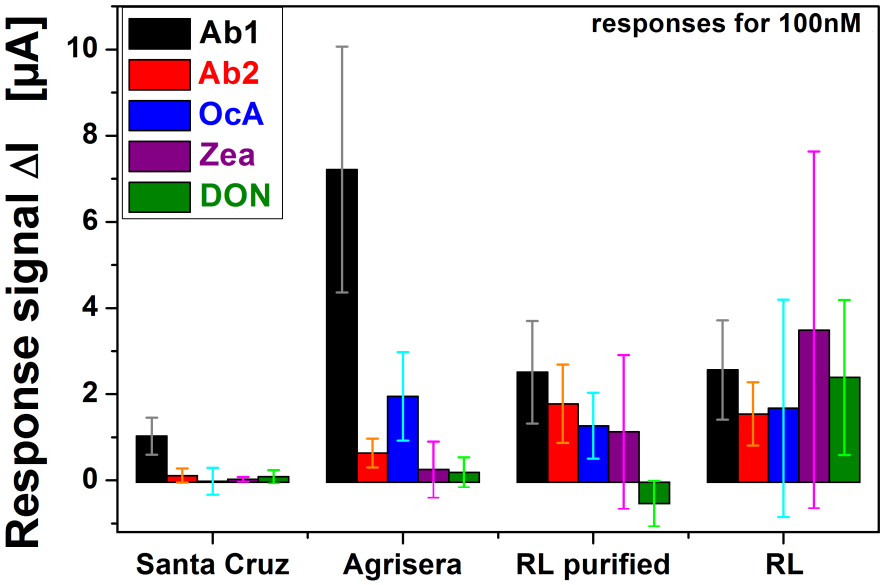

Figure 4.12: Cross selectivity of AfB1 antibodies. For each antibody type four measurements, each using five different toxins with concentrations of 100 nM were performed. The mean values of signal response and the standard deviation for all measurements is shown in the block chart. Antibodies from Santa Cruz and Agrisera show the best specificity.

Furthermore different suppliers for the AfB1 antibodies were tested accordingly. Significant differences in selectivity and sensitivity are observed for all different antibody types, while Agrisera polyclonal antibodies show the strongest responses with good selectivity and the Santa Cruz monoclonal antibodies show by far the best ratio of specific to non-specific response with a significantly lower response. From the direct comparison of the antibodies, using the same parameters and solutions, it can be concluded that the non-specific response signals origin from the antibodies itself. This is a good indication for the reliability of the biosensor, since differences between antibodies were expected and could be demonstrated sufficiently by the

use of graphene FET system. The responses of the cross-reactivity testing for the Santa Cruz and Agrisera antibodies are shown in figure 8.4 and are compared in figure 4.12. The detection in real-life samples requires high selectivity, since the matrices for analysis may contain different types of unknown contaminants, implying a high possibility of false positives, which would limit the applicability significantly. Therefore the antibodies with the highest specificity, namely the supply by Santa Cruz, were chosen for further experiments, although this antibody showed the lowest total response signal and therefore most probably will also have the worst LOD. In this work the choice between sensitivity or selectivity was made for selectivity.

Chapter 5

Measurements in Real-life Food Samples

For the measurements in real-life samples, naturally contaminated and grounded corn and wheat were supplied by Romer Labs® and used for the experiments in this work. Since the extraction from both grain types results in a low pH of the obtained extract (usually between pH 4 and pH 5), the antibodies immobilized to the FET channel are expected to be positively charged. Also because of the different nature of different corn or grain types the pH is expected to shift from extract to extract, therefore it has to be readjusted to constant value after extraction for comparable measurements.

To evaluate the non-specific binding and molecular adsorption of real-life foodstuffs to the bare graphene sensor surface, a series of measurements was performed using different types of grain extracts (extraction protocol is given in chapter 3.2.1). This approach was chosen to elucidate the key factors of any given grain type and the corresponding behaviour of the FET. The measurements were performed in DC and alternating current (AC) mode. In a next step the responses of the FET to corn extracts were tested, different passivation layers developed and a suitable linker for the immobilization of the antibodies to the passivated surface found. Subsequently the responses of corn extracts were tested in DC and AC mode and compared to the responses from ionic changes. Furterhmore, an array detection system was established and theoretically evaluated. Finally dose-response curves for AfB1 concentrations in corn extracts were measured, a calibration curve plotted and the obtained results compared to the requirements of the food safety legislature.

5.1 Impedance Spectroscopy of Grain Samples

Since the responses when using DC do not give any detailed information of the origin of the response signal, impedance spectroscopy was performed using the same flow cell, chip geometry and working materials as used for all other measurements in this work. The advantages and disadvantages of impedance spectroscopy are described in chapter 4.3.

Six different corn types were used in this work: rye, barley, corn whole, corn ground, soy and wheat. For a better impression of the texture, dimension and condition of the used samples, photos of the used samples are given in figure 8.8. Extracts from all corn types were measured with a FET initializing impedance spectroscopy. Therefore a baseline was recorded using a PBS buffer (pH 7.4, 17 mM ionic strength) for approximately ten minutes, followed by the injection of the first grain extract and switching back to PBS after another ten minutes. This procedure was repeated for all grain extracts. Ultimately the results were compared to the results from the ion strength titration in figure 4.3 to obtain an approximate measure of the influence of ionic components from the grain samples.

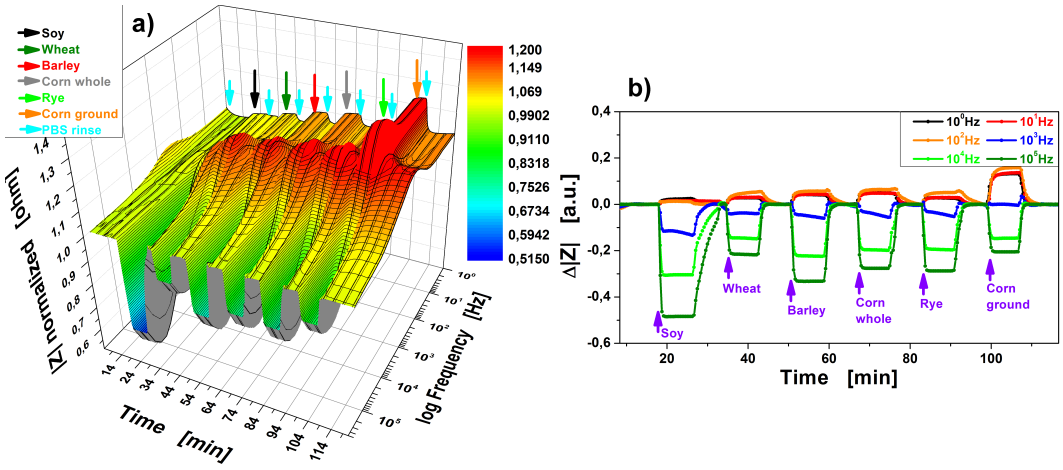

Figure 5.1: a) Normalized impedimetric measurement of different grain types. The arrows mark the injection using the color codes on the top left. b) 2D representation of the same measurement for grain type responses at different frequencies.

As can be seen from figure 5.1, the responses at higher frequencies decrease the impedance of the FET, while the responses for lower frequencies are increasing the impedance. The de-convolution of the responses from real-life food samples are almost impossible to analyse in detail since there are plenty of factors resulting from

the food ingredients that can influence the sensors impedance. Therefore, only an estimation of the origin of the observed signal can be perforemd here, but the results from the ion titration shown in chapter 4.3 show a very strong response of the FET to the change of ionic strength of the used solution and can therefore justify an approach in which the influence of ion strength is compared to the responses of the grain types. Indeed, the measured impedance spectrum for grain types show a very similar behaviour for high frequencies as it can be observed when using standard buffers with variable ion strength. Keeping this in mind, a simple calculation of the ionic strength of the grain extracts can be provided using the results from PBS ion titration as a standard calibration curve at high frequencies. Results obtained from this procedure can then be compared again with the ionic strength measured directly from the extracts and lead to an estimation of the influence of ion strength change after extraction. Also a comparison of the Bode plots obtained from the ion titration with the responses for the grain types was accomplished. As a third route for comparison of these results, an equivalent circuit for the graphene FET system was used and the fitting parameters were plotted against the calculated ionic strength to evaluate if the resistance of the grain extracts change in accordance to the ionic strength of these solutions. The sum of these results still gives no prove of the origin of the nonspecific signals observed from matrix effects, but gives an overview and allows an estimation of the impact of ions that are contained in different concentrations in different grain samples.

In detail, firstly a calibration curve resulting from the ion strength titration in figure 4.3 was plotted using a simple exponential fit. The exponential fit for every magnitude of frequency can be seen in figure 8.5. Interestingly, the dependency for lower frequency becomes almost linear with a change of the reactions exponential k value from negative to positive. For a frequency of around 20 Hz no responsive behaviour of the FET should be observed. All frequencies below 20 Hz display only a slight slope, which could also be fitted linearly, which was done for the measurements of ionic strength shown in previous work. Anyhow, for the calculation of unknown ionic strength of the grain extracts, the exponential fits were used as calibration curves and the evaluation was performed for 10^3, 10^4 and 10^5 Hz. The results for the calculation at 10^5 are shown in figure 5.2a. The deviations and results for the calculations at different frequencies are shown in the block diagram in figure 5.2c and table 5.1. As can be seen in that diagram, the results have a deviation of up to 25 %, depending on the frequency used for calculation. Also there is no trend

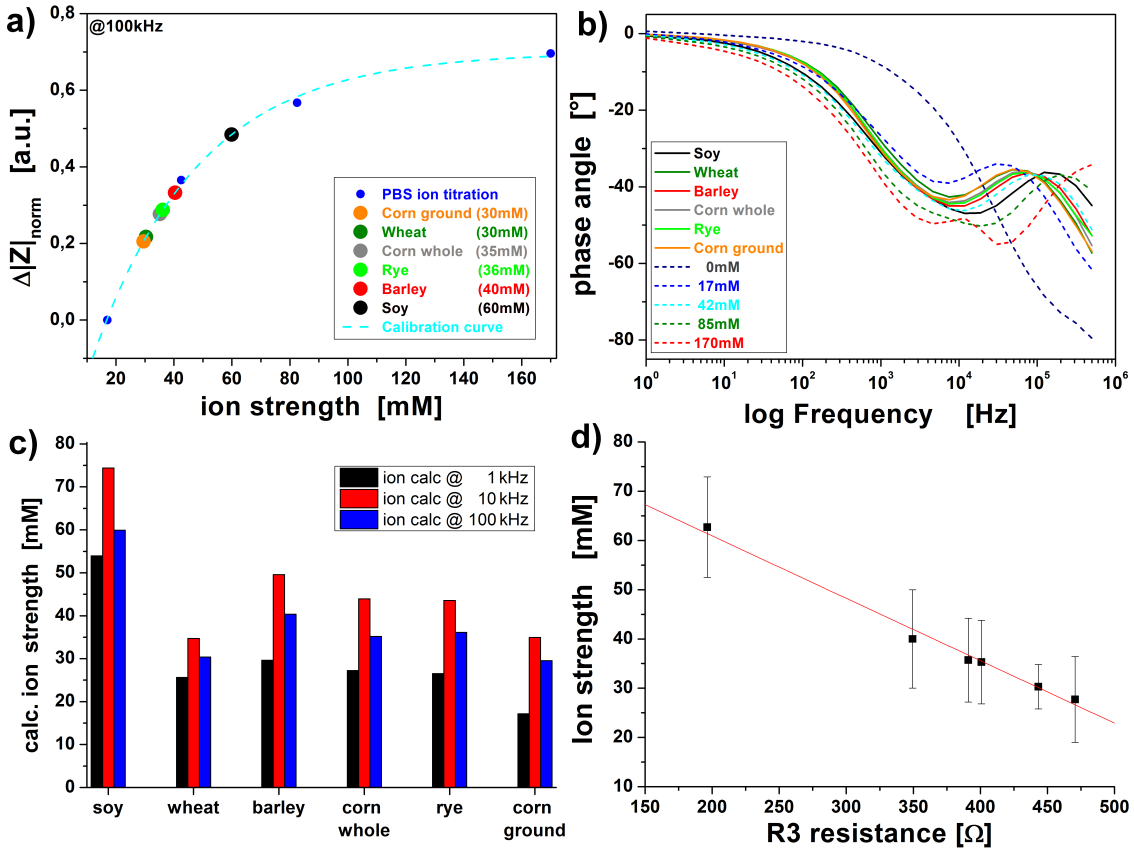

Figure 5.2: a) The results from the ionic strength titration in figure 4.3 are shown as dark blue data points, and the calibration curve (dashed light blue) was fitted using a simple exponential fit over the ion titration data. The changes in impedance for all grain types were correlated to the ionic strength and are shown as coloured dots. b) The Bode plots of the responses from the ion titration are shown as dashed lines, while the results from the measured grain types are shown as solid lines. c) Results for the evaluation of the ionic strength for all grain extracts, using different frequencies for analysis. d) The fitting parameter of the equivalent circuit R3, which corresponds to the conductivity of the used matrix (the grain extracts), plotted against the calculated ion strength. Error bars were calculated from the deviations using different frequencies for the ionic strength calculation.

observable for the relation of the calculated ion strength to the frequency used for calculation, yielding the maximal results for 10 kHz. The mean value and standard deviation was then calculated from the results of all three frequencies and used for comparison with the equivalent circuit, developed for the presented system. The equivalent cirquit used here was developed in the framework of a diploma thesis by a student under my supervision [214]. The curves from the Bode diagram (figure 5.2b) were fitted using the equivalent circuits equation, yielding values for all equivalent circuit parameters, which contain the capacitance, the resistivity of the graphene layer and the resistivity of the used solution (resistor R3). Because the

conductivity of an electrolyte is linearly dependent on the ionic strength of the liquid, a linear fit for the relation of the conductivity to the calculated ion strength was performed and is shown in figure 5.2d. The accordance of that fit is a further indication of the high impact of ions on the properties of the obtained extracts from different grain types. The Bode plots of the ionic strength measurements in buffer as well as in grain extracts are shown in figure 5.2b and were used as a control for the results of ion strength calculation as described above. All curves for the extracts have the same shape as the curves from the ionic strength measurements in buffer. They also progress in the same manner as the results calculated from the impedance and are located exactly between the two curves for 17 mM and 42 mM. The result of the Soy extract is an exception and gave a calculated ionic strength of 60 mM, hence lies at the half way between the curves for 42 mM and 85 mM. This observation corresponds well to the results obtained by titration and direct measurement of the conductivity. For validation of the obtained results the conductivity of the grain extracts was also measured with a water conductivity meter and the values from that measurement were used to calculate the corresponding ionic strength of the solutions and are shown in table 5.1. The ionic strengths found by impedance measurements for most of the grain extracts are very close to the ionic strengths obtained by the conductivity meter, which underlines the applicability of the presented approach and validates the results obtained by the rGO-FET system.

Table 5.1: Comparison of the results for the ionic strength of the grain extracts obtained by impedimetric measurements to the results from measurements with the water conductivity meter.

Grain type	*Impedance*	*Conductivity meter*
Soy	54 mM	53.9 mM
Barley	29.6 mM	34 mM
Corn ground	17.2 mM	32.8 mM
Rye	26.5 mM	29.3 mM
Wheat	25.6 mM	28.1 mM
Corn whole	27.2 mM	26.9 mM

Concluding, it can be said that a full proof of the origin of the responses for injections of real-life samples could not be stated so far, but it is highly likely that the main effect responsible for changes observed in DC is the change of ionic strength. On the other side, impedance spectroscopy has been shown to be non-sensitive against changes of the pH [214], a factor which could also play a major role in DC mea-

surements. Therefore this investigation focuses only on the ionic strength, while the change in pH during extraction was evaluated by a simple pH electrode measurement. Further effects like the adsorption of materials to the surface definitely overlap with the observed behaviour, but the good correspondence for all three applied calculation routines of the ionic strength indicate that the effect obtained by ionic strength is the most prominent reason for non-specific response signals when measuring different grain extracts. With this knowledge a passivation mechanism could be found to shield the surface from these effects while still allowing a specific measurement of the desired analyte from real-life food samples.

5.2 Grain Extract Responses in DC Mode

The responses of different grain types to the sensor surfaces were also studied using DC measurements. Because the final sensor should be working in DC mode, this evaluation type is very important due to the high comparability with the results aimed for the finished devices. Firstly, a series of measurements using only two different grain types was performed in such manner, that a baseline was established for a given FET device and then the injection of the grain extract was performed, measuring the I_D. Thereby attention was paid to the baseline level and the correlation to the response signals obtained by grain type injections to answer the question if the conductivity of the transistor would define the response signal strength for a given grain extract. The goal was to find a mathematical approach of normalizing the response to a certain extract from the measurement data and hence extracting only the aflatoxin binding responses from the read-out curves. Fifty devices were measured in that way, half using corn extracts and the other half using a wheat gluten extract. Both solutions were not tested on a single device because it can not be excluded that

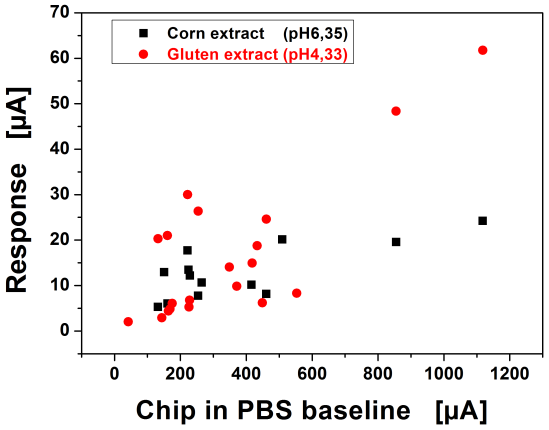

Figure 5.3: Dependency of the response signals for corn extracts (black) and gluten extracts (red) on the baseline level of the corresponding FETs. A linear trend is observable, but the variation of the data is too large for analytical interpretation.

the matereial is not washed off the surface, which would tamper the significance of the results. The relation of baseline levels to the grain extract responses is shown in figure 5.3.

As can be seen from these measurements, the dependency of the responses on grain extracts are not directly dependent on the conductivity of the corresponding FETs. A basic linear dependency can be observed, but the I_D range of interest around 400 μA shows the highest variation of data and therefore can't be used to predict the response levels of corn extracts for different FETs with known resistivity. Arguably several other factors, like the number of intercalations of graphene sheets in the channel, the surface potential of these sheets, different affinities of the devices to the extracts or also the non-homogeneous nature of the grain extracts itself can have significant impact on the responses for the grain extracts obtained by the graphene FETs.

To compare the results from impedance spectroscopy, where ionic strength was assumed to be a major factor for the responses on the grain extracts, a correlation of the responses for ionic changes to the baseline level of the corresponding FETs was evaluated. The relationship of the responses of eleven different graphene FETs when changing the ionic strength from 85 mM to 42 mM to the baseline level of the corresponding devices was evaluated and is shown in figure 8.7. As can be seen from that measurement, also for the change of ionic strength no defined relationship of the devices conductivity to the responses can be observed. This means that the conductivity of the fabricated FET devices is not crucial for the expected level of response when changing the ionic strength of the used electrolyte. This result gives further indication that the main share of the response signals obtained by grain extract responses is originating from variations in the ionic strength of the extracts.

In other work it was shown that the conductivity of graphene layers is modified by the binding of aromatic structures [215] by dispersion reactions of the π electrons [216], oppositely charged molecules [217], hydrophobic compounds [218] or materials binding covalently by carboxylic or hydroxyl groups to the surface [219, 220]. During such non-specific binding events the local carrier concentration is modified and leads to step-like changes in the conductivity [62]. A real-life food sample, like the studied grain extracts, containing a vast variety of different molecular compounds most likely also contain a non-negligible amount of biomolecules that can

form or adhere via some of the mechanisms described above. Therefore a total passivation of the surface is most likely only possible if the entire graphene surface is spatially isolated from the analyte solution. It can be concluded that for the reproducible detection of aflatoxins from real-life food samples either the extraction process has to be modified or a passivation for the graphene FETs has to be developed, minimizing the non-specific signals.

5.3 Surface Passivation

Since the responses of the graphene FETs to real-life food extracts apparently have a dependency on several factors, a technique has to be developed for the normalization, elimination or predictability of these signals. For the fabrication of an automatized detection system for toxins from food-stuffs an approach utilizing the application of a passivation layer and measurements in array configuration with two or more graphene channels were chosen in this work.

A definition on what a passivation layer is, is given by the Electrochemical corrosion nomenclature in [221] and states as followed:

Passivation is the process of transition from the active to the passive state by formation of the passivating film. Passivation is achieved by... the presence of an oxidized substance in the neighbouring solution which passivates by being reduced (passivator).

A passivation layer has to be found which shield the graphene surface from the interaction with the samples, ideally gives predictable and reversible results but also allows the application of linker molecules and surface antibodies while still function in such manner that the detection principle is not changed. In principle two types of such protective layers can be applied:
a) A single layer of molecules, chemically binding to the graphene surface and the linker molecules which do not hold a protein. The advantage of this approach would be the unchanged structure of the transistors, not significantly changing the dielectric properties and therefore not minimizing the response signals but only bringing the surface potential to another level. Unfortunately changes of the ionic strength in the real-life food samples still would influence the conductivity of the graphene layer undamped in comparison to the case of bare graphene, which would

again give unpredictable signals because of unknown ionic strength of the foodstuff extracts additionally to the arguments in chapter 5.2 (also see figure 8.7).

b) A solid layer of a high-K material, preferably a metal oxide would completely shield the graphene surface from contact with the food samples, but would also minimize the detection signals. The measure of signal loss is dependent on the ratio of layer thickness and electrical permittivity of the chosen material. The disadvantage is that the coupling chemistry for surface antibody immobilization has to be changed when using a non-graphene-like surface.

5.3.1 Chemical Protective Layers

Materials which are widely used in literature for the passivation of graphene, but also materials with an appropriate chemical structure were tested. The range of measured extracts was minimized for this study in such means that only corn extract was used. All further measurements for the passivation of the graphene FETs were performed using the same protocol for the extraction of the corn sample and the pH of the obtained corn extracts was adjusted to pH 5 for all samples.

The testing was performed using different V_G, since the EDL could also manipulate the binding behaviour of the extract to the graphene surface because of the change of the surface potential for different Gate voltages. Firstly, a standard curve was measured using a blank graphene FET. The measurement was performed by injection of the food sample at different V_G's and was used for further comparison with the responses obtained by passivated devices. Also a 800 mM glucose solution was prepared in PBS buffer for comparison to the responses obtained by corn samples (data shown in the appendix figure 8.10).

The three materials tested for the passivation of the graphene surface are 1,4-Di-n-butylbenzene, fluorobenzene and polyethylene glycol (PEG). From literature PEG is known to have a good effect as a surface passivation agent on graphene, minimizing the unspecific binding and being used by many groups therefore [215]. For comparison of different passivation agents again signal normalization was applied for the observed Baseline level (I_{D0}) of the measurement. The results for the tests of the passivation effect of these materials on graphene are shown in figure 5.4. 1,4-Di-n-butylbenzene, and fluorobenzene show only minor change of the responses in

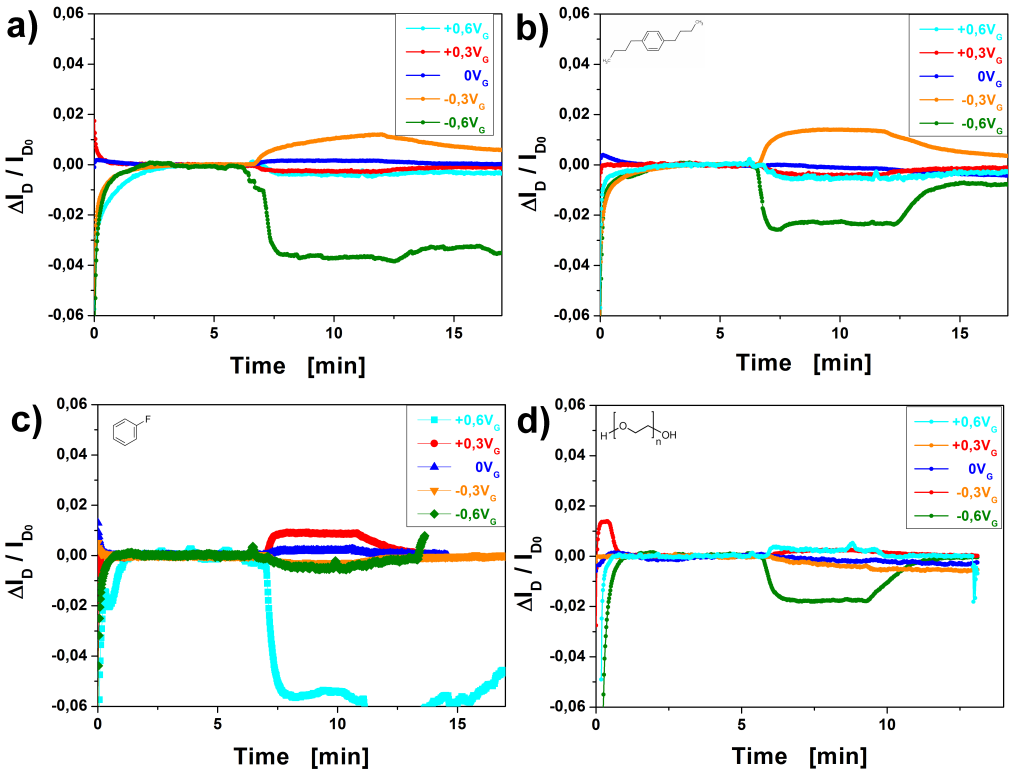

Figure 5.4: Corn responses to a) bare graphene, b) graphene coated with 1,4-Di-n-butylbenzene, c) graphene coated with fluorobenzene and d) graphene coated with PEG. The chemical structures of the used materials are shown in the top left of the corresponding measurements.

comparison to bare graphene and hence are not suitable as passivators. PEG showed the most diminished response signals for negative V_G, but still does not completely passivate the surface against corn extract response signals. In literature PEG is often presented as a powerful passivation agent. Hence a detailed study of the passivation properties of PEG for corn extract signals was performed. Therefore variation of PEG concentration, incubation length and the use of PEG in combination with the linker used for antibody immobilization (PBSE) were tested (data not shown). The effects of PEG passivation are diminished when applied after linker immobilization, pointing at an interaction of the corn extracts with the linker molecules.

5.3.2 Metal Oxide Passivation Layers

A different approach for surface passivation was tested by using a high-K metal oxide layer. The surface was covered completely with an insulating layer of Ta_2O_5 by reactive sputtering. A metal oxide was used for this purpose due to it's inert surface,

insulating properties and high electrical permittivity which allows the detection signals to couple through the layer to the transducing unit, the graphene layer. Because of previous experiences with this material for the fabrication of protective layers [222], a Ta_2O_5 layer applied by reactive sputtering in a defined thickness was chosen to be the best suitable for this approach. Due to it's high dielectric constant Ta_2O_5 is widely used for the fabrication of capacitors in electronics [223]. Tantalum oxide films also display very high chemical and thermal stability [224], low interfacial reactivity [225] and reactive sputtering allows for the formation of films with low surface roughness [226], which decreases the surface area and allows for more planar distribution of immobilized biomolecules. The dielectric constant of Ta_2O_5 films strongly depends on the films thickness, the lattice structure and states of oxidation [227]. A realistic estimation for the dielectric constant ϵ_r of Ta_2O_5 is around 20 [224].

The technique used for the application of the Ta_2O_5 layers was reactive sputtering, which used a solid Tantalum target and oxidises the material during the sputtering using a specific ratio of Argon-O_2 as reactive gas. O_2 is introduced into the chamber and also reacts with the sputtering targets, which in the presented case is the graphene surface and will oxidise during the sputtering process, therefore the conductivity of the FETs is lowered. It was observed in the framework of this thesis that the resistance of the FETs after the sputtering process can increase even hundredfold if the sample is exposed too long. The target voltage, emission from the plasma, the partial gas pressure and the sputtering time were optimized for the lowest possible exposure time of the samples to the reactive gas and plasma to keep the oxidation of the rGO layer as low as possible. The disadvantage of higher sputtering rates are that this can result in a less homogeneous layer of the sputtered material. Pinholes in the sputtered layer can occur even for thicker layers when using shorter process times.

To evaluate the effect of the metal oxide layer on the graphene surface, a series of test measurements was performed and the results are shown in figure 5.5c-f. FETs were fabricated using 10 nm and 50 nm thick Ta_2O_5 films, but also a negative control was performed in means of a FET with no underlying graphene layer but only the Ta_2O_5 layer as the semiconducting material. Ta_2O_5-FETs have been fabricated before and were applied for the detection of ionic changes and pH [228]. It could be argued that the Ta_2O_5 itself can be used as the transducer and semiconductor

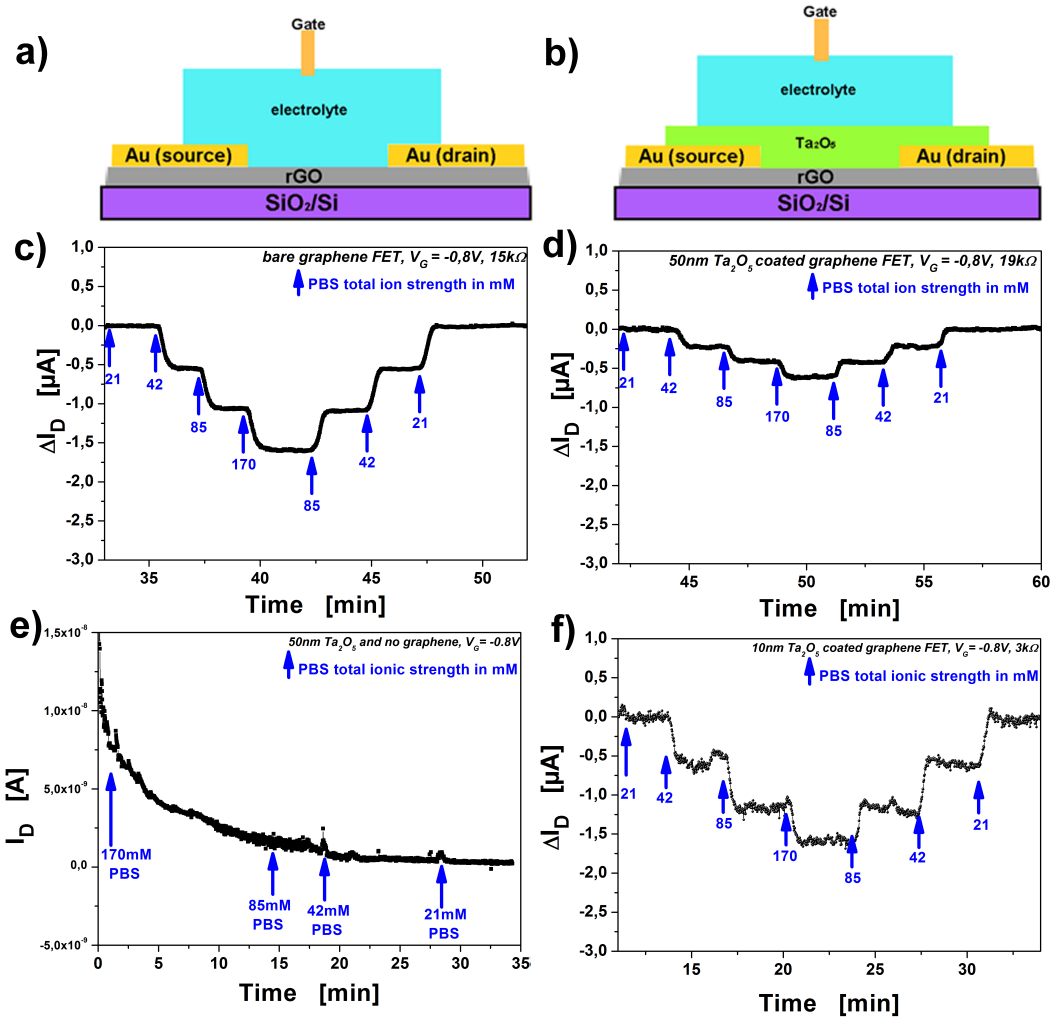

Figure 5.5: Schematic structures of a) an non-passivated FET and b) a Ta_2O_5 passivated FET. Titrations of PBS buffers with various ionic strength were performed for the following FETs: c) Bare graphene. No passivation layer was applied. d) Graphene with a 50 nm coating of Ta_2O_5. e) A 50 nm thick Ta_2O_5 coating with no underlying graphene layer. This measurement was used to prove the insulating properties of the Ta_2O_5 layer. f) A 10 nm thick Ta_2O_5 layer.

of the FET, but the conductivity of this layer is much lower than the graphene layer's and therefore is not expected to supply a relevant part of the charge transport. With the measurement in figure 5.5e these concerns were eliminated, because the total current through the Ta_2O_5 layer was found around $1x10^{-10}$ Ampere after stabilization of the baseline, which is about five orders of magnitude lower as for the same film with a basal plane of graphene shown in figure 5.5d. The slow stabilization in this measurement can be accounted to capacitative charging effects of the surface when the potential is applied. To achieve good comparability of the non-passivated and passivated FETs, devices with very similar conductivity have

been chosen. As described in chapter 3.4.1 for the detection of biomolecules, only FETs with a resistance below 1 kΩ were initially selected. Because of the sputtering process re-oxidation of the graphene layer of the sputtered FETs takes place and therefore for good comparability also blank devices with higher resistances were chosen: 15 kΩ for the non-passivated FET (figure 5.5c) and 19 kΩ for the FET with a 50 nm Ta_2O_5 layer (figure 5.5d). In comparison to the FETs without a passivation layer as shown in figure 5.5c, the responses to changes of the ionic strength of the FETs with a Ta_2O_5 layer have a higher noise level and lower response signals. The device fabricated with a 10 nm thin film of Ta_2O_5 shows a particularly high noise level, which is resulting from the porous structure of such thin films sputtered under the adjustment for quick sputtering to reduce the exposure time to the Ar-O_2 reactive gas.

It was shown by Christensen et al. that a 500 nm thin Ta_2O_5 layer, applied by the sputtering technique used in their work has a pinhole density of 3 cm^{-2} [222]. These layers were amorphous and had to be annealed first to achieve polycrystaline structures. However, the dielectric constants of these films have been studied and it was shown that a higher crystal structure also leads to higher electrical permittivity [229], which is desired for the fabrication of a biosensor because of the better coupling to the base transducing layer, the graphene. Contrary to that, other studies showed that annealing below 600°C will increase the leakage-current and provided TEM observations which prove that annealing at lower temperatures increases the pinhole size [230]. As for the scope of this work no annealing aperture which could reach such high temperatures was available and therefore (to not increase the pinhole size) annealing was not performed. Nevertheless the pinhole density was measured by CV, as already demonstrated in other work a viable tool for the testing of the porousness of a insulating film [231, 232]. Therefore a droplet of ferrocenemethanol was applied on the Ta_2O_5-coated FET surface and the working electrode was positioned 2 mm over the surface in direct contact with the electrolyte. The protective metal oxide layer should prevent a redox reaction of the mediator [233]. The same measurement was performed for a non-passivated graphene FET and the results compared. From the difference in area of the volotammograms the ratio of leakage current through the Ta_2O_5 layer can be estimated. The corresponding measurement is shown in figure 5.7b. AFM of a 30 nm Ta_2O_5 film sputtered with the same parameters as the passivating films for the FETs was performed to evaluate the roughness and porousness of the layer. Evaluating the results, a root mean square

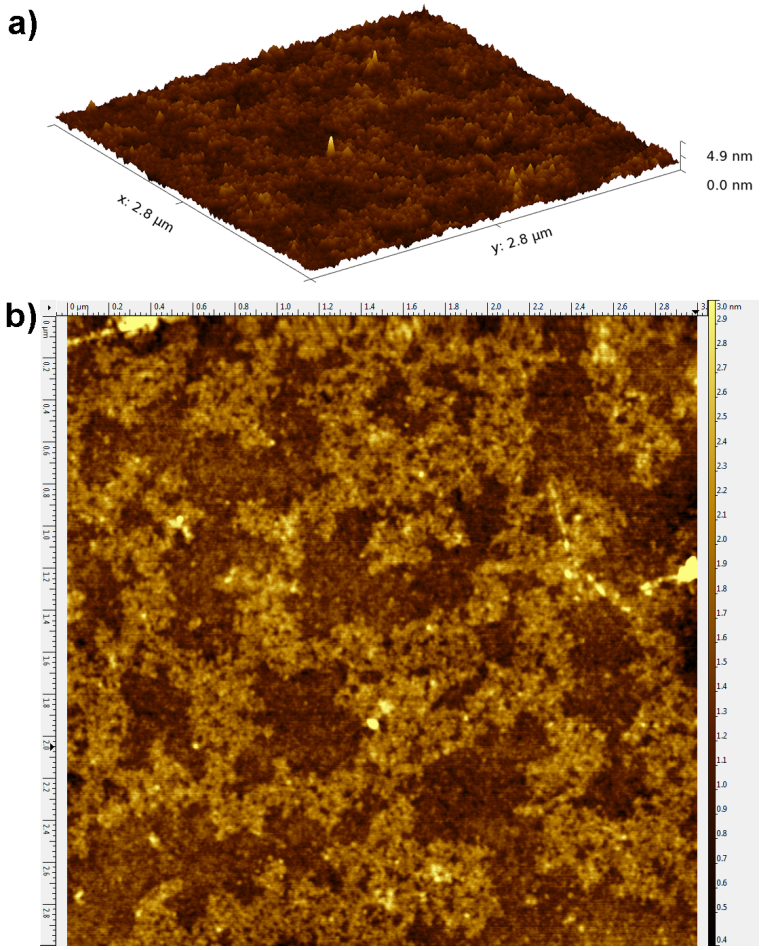

Figure 5.6: a) 3D view of the Ta_2O_5 surface structure measured by AFM. Impurities/contaminants are seen as the yellow spikes in the structure. b) Top view of the same area as shown in figure a, the structure of the underlying graphene flakes is visible as the brighter areas, with the difference in height of this areas and the darker areas being a little less than 1 nm in average, which corresponds to the height profile of graphene flakes.

for the surface roughness was found to be 0.45 nm, which is very low. Besides a few impurities which resulted in 2 nm high features, the rest of the surface seems to have even lower roughness values. The shape of the underlying graphene flakes also is seen through the Ta_2O_5 as an imprint of the structure which is shown in the AFM image in figure 5.6.

Furthermore, the binding behaviour of corn extract samples to the surface was studied by Quartz Crystal Microbalance with Dissipation (QCM-D) measurements. Two comparable devices with similar conductivity were used for these measurements, establishing a baseline with PBS, followed by injection of the corn extract for 30 minutes and then was washed with dH_2O for another 90 minutes, followed

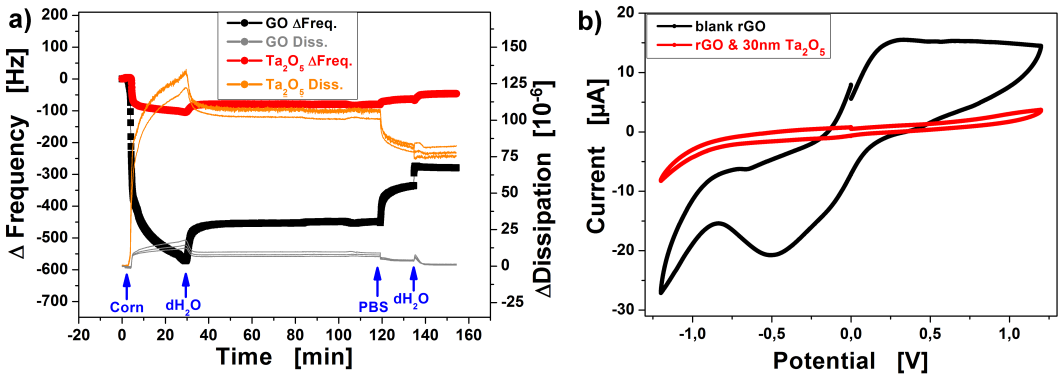

Figure 5.7: a) QCM-D monitoring of a graphene FET coated with a 15 nm layer of Ta_2O_5 (red and orange data) in comparison with a non-passivated FET (black and grey data). The frequency shift is lowered for about 80 %, which indicated less mass adsorption at the sensor surface for the passivated FETs. b) CVs of a non-passivated graphene FET (black curve) and a FET coated with a 15 nm layer of Ta_2O_5. The curve area is lowered for only about 40 % which indicates a porous film.

by rinsing with PBS buffer again. The results are shown in figure 5.7a and indicate that the Ta_2O_5 layer protects the surface in such way, that only about 20 % of the material from the extract binds to the surface. This can be concluded due to the fact that the frequency shift for the bare graphene layers was found around 650 Hz and that for the Ta_2O_5 layers around 120 Hz. The relation of frequency shift to the mass absorbed to the sensor surface has a linear dependency, while the dissipation (orange and grey curves) give a measurement of the rigidness and density of the adsorbed material on the surface. Higher dissipation and more broad distribution of the overtones, which are shown as separate lines in the same color in figure 5.7a, stand for higher viscoelasticity or softness of the adsorbed layer and can be seen as indication for the passivation of the surface with less dense binding in comparison to the bare graphene surface. At the same time the leakage current measured in the CV in figure 5.7b is lowered for about 95 % (calculated from the area of the curves), which corresponds to good shielding of the surface and reduction of the charge transport through the metal oxide layer. Anyhow, these results show only the preliminary testing for the fabricated devices and indicate that a thicker layer of Ta_2O_5 could deliver more homogeneous surfaces with less pinholes and at the same time protect the surface from molecular adsorption even more than the devices fabricated with passivation layer thickness of 15 nm like they are shown in figure 5.7. Because thicker metal oxide layers also increase the sputtering time and therefore the oxidation of the graphene surface, a trade-off of layer thickness and conductivity-loss had to be found. Investigations on thicker films of Ta_2O_5 have

been performed in the framework of an associated diploma thesis [214], where it was shown that a 30 nm thick layer is sufficient to decrease the leakage current in CV measurements for more than 90 %.

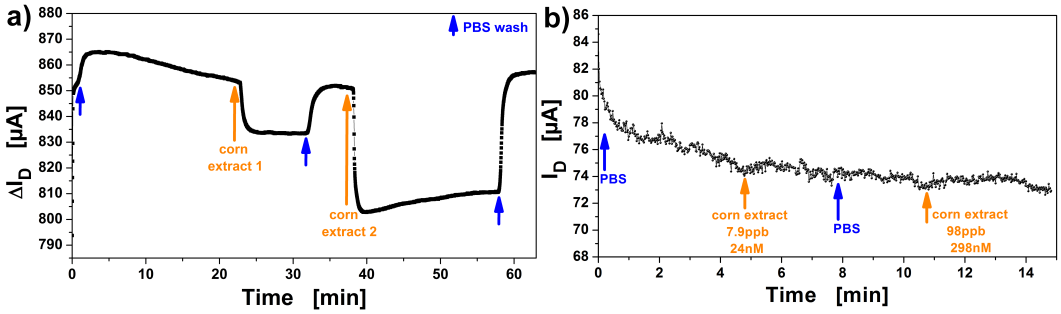

Figure 5.8: a) Interaction of corn extracts to the graphene surface of the FET. For both corn extracts different response signal strengths are obtained with signal strengths of approximately 20 μA and 50 μA. b) Interaction of the same corn extracts with a Tantalum passivated surface. The resistivity of the FET is lowered, but no responses for the corn extracts are obtained and wear off in the noise of the baseline, which is higher for the passivated devices.

Interestingly, the major advantage found for the application of Ta_2O_5 layers is the increase of comparability and predictability of different FETs. In opposite to the results shown and discussed in chapter 5.2, the responses of different FETs passivated with Ta_2O_5 have a consistent relationship of response signals and device conductivity. It should be therefore possible to find a normalization routine to increase the comparability of the conductivity and sensitivity of the FETs which, non-passivated, has a high variation due to the variations resulting from the fabrication process.

Linker Chemistry on Metal Oxides

For the coupling of antibodies to the sensor surface a suitable linking agent has to be found. The linker of choice for the immobilization on graphene was PBSE, which is bound to the surface via a pyrene $\pi - \pi$ interaction. On a metal oxide surface another method has to be used and for this purpose two different linkers have been used during this dissertation. For the testing of the applicability of the linking materials 3-Glycidoxypropyltrimethoxysilane (GPTS) and 11-Pentafluorophenylundecanoatetriethoxysilane (PFDTS) have been tested. Test of the unspecific binding of corn extract, AfB1 detection in aqueous buffer solution and assessment of electron mobilities were performed for the characterization of these linkers. The experiments were performed for FETs with 15 nm layers of Ta_2O_5 as well as for 30 nm of Ta_2O_5 protective layers.

PFDTS (11-Pentafluorophenylundecanoatetriethoxysilane) was tested as linker for the immobilization of proteins on Ta_2O_5 coated surfaces with Ta_2O_5 thickness of 15 nm and 30 nm. Therefore a 1 μM linker concentration was diluted in Tetrahydrofuran (THF) and applied on the Ta_2O_5 surface of the FETs. Tests were carried out in PBS buffer to exclude effects from the corn extract. AfB1 detection was successfully performed in PBS buffer solution as matrix medium. For the detection of lower Aflatoxin concentration in PBS the measurements were reproduced on a 15 nm Ta_2O_5-coated FET. In comparison to experiments performed without linker and antibody on Ta_2O_5 coated FETs an unspecific signal from the corn extract is observed when using PFDTS. This indicates to nonspecific adsorption or binding of the corn extracts ingredients to the linker or the immobilized antibody. I_DV_G curves were measured for FETs before and after linker immobilization, showing a change in charge carrier mobilities when the linker is applied, which indicates successful binding to the metal oxide surface. Furthermore I_DV_G curves were recorded when washing with buffer as well as for the injections of corn extracts and a significant displacement of these characteristic curves is observed on PFDTS functionalized surfaces (data not shown). Also a relatively higher noise level was observed in comparison to non-functionalized surfaces, again indicating interactions of the corn extracts to the linker molecules. Furthermore a titration experiment of AfB1 was performed in buffer and in corn extract, testing the responsive behaviour of the FET when using PFDTS as a linker molceule. The Signal-to-Noise-Ratio was not sufficient for a proper analysis of the binding data, although peaks for concentrations of 160 nM (50 ppb) and 16 μM (5 ppm) were observed, proving the functionality of the linker.

As for the second option in the choice of linker molecules, GPTS was tested in the same way as it was performed for PFDTS. Again, Ta$_2$O5 thickness of 15 nm and 30 nm were used, detection was performed in buffer and in corn extracts and I_DV_G characteristic curves were recorded before and after corn extract injections. The obtained data shows much more stable responsive behaviour of the biosensor when injecting corn extract samples, but still showing a response when injecting uncontaminated corn samples, less than for PFDTS, but clearly indicating an interaction of the corn matrix to the linking molecule. Also a titration curve using immobilized GPTS linker and the corresponding antibodies was performed, obtaining responses for even lower concentrations than for the PFDTS linker and all in all confirming the functionality of GPTS as a linker for the antibodies on metal oxide surfaces. The

much better signals when using GPTS in comparison to PFDTS can be explained by the relatively shorter structure of GPTES and the resulting increase in Debye length. Unspecific binding of corn extract onto the surface or linker was observed to be much lower (only 200 nA) than with PFDTS linker. Transistor characteristics were obtained and charge carrier mobilities were found to be diminished for only about 50 % in comparison to the same device before Ta_2O_5 coating. The direct comparison is shown in the I_DV_G graph in figure 8.9.

Due to the findings in this chapter, GPTS was chosen as the linker for antibody immobilization on Ta_2O_5 for all future measurements conducted in the scope of this work.

5.4 Array Configuration

A new approach is to measure the response of corn on two FET devices simultaneously with the goal to establish sensor arrays in seria. The first of those separately measured devices should contain the linker and specific antibody, while the second device is immobilized with a linker and an unmatched antibody (anti-BSA). By comparison of the results of the two devices, a calculation of the specific signal is possible. A sensor array was created by serial connection of two FETs and the corresponding measuring equipment, see figure 5.9a. The figure shows a photo of the preliminary measurement setup. Two flow cells and FET devices are connected serially and flushed with the same solutions while read-out is performed on two measurement channels. A 15 second measurement delay is induced by the liquid pumping times, which was subtracted from the shown data and hence the FET responses were synchronized. Measurements were performed by immobilization of a target antibody and a control antibody onto the chips separately.

For the detection of AfB1 in PBS the sensor array shows that a response signal is only obtained for the devices with the target antibody, while the Anti-BSA immobilized devices shows no response (figure 5.9b). An increased read-out performance is achieved by serial measurement and peaks can be ascribed to specific AfB1 binding due to the automatically included negative control. It was also shown that the LOD is well below 6.5 ppb (21 nM) which corresponds to the results measured for the characterization of binding affinities for the AfB1 - antibody interaction shown

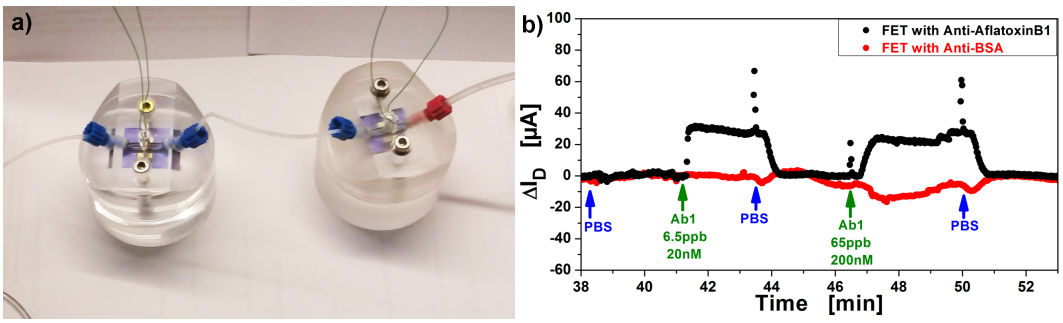

Figure 5.9: a) Image of the array setup as used for the array measurements using a serial connection of two separate flow cells and FET devices immobilized with targeted and non-targeted antibodies. b) Detection of 20 nM (6.5 ppb) and 200 nM (65 ppb) of AfB1 using the array buildup with targeted (black curve) and non-targeted (red curve) antibodies. No responses can be seen for the control measurement, while the other FET with the targeted antibodies responds with a signal of almost 30 μA.

in chapter 4.6.2. Also the change in direction of the detection signal at around 33 ppb (106 nM) was confirmed and the data recorded is shown in figure 8.11 in the appendix.

The array shows a better performance if the device comparability is improved for further analysis, hence great attention has to be spent to the fabrication routine of the FETs. Because the fabrication in this work was performed completely manually, the operators error increases the deviation in the FET characteristics, which is not ideal for the approach of comparative array measurements. Nevertheless, the principle of this detection method was used for further measurements in real-life samples because it seems to be the most viable tool to tackle the challenge for the detection of low concentrations of AfB1 from real-life food samples.

5.5 Array Measurements in Corn Samples

5.5.1 Application of the Array Configuration for the Detection of Aflatoxin B1 from Corn Extracts

Normalization

For the array measurements with corn extracts following protocol was used: First a baseline is established with PBS. Then two corn extracts from different corn samples without any AfB1 contamination were injected (GGU corn and Victor corn types, obtained from Romer Labs®). This step is supposed to give a valid comparison between the used FETs as they might slightly differ in device parameters. The responses for both sensors in the array configuration are then normalized to these two responses in such manner, that the responses obtained for the used V_G give the same total change in device conductivity. Therefore a constant is multiplied to the negative control FET in that way that the responses from blank corn extracts have the same size in both curves. This procedure does not affect the characteristics of the obtained curves, furthermore it is only scaling both curves to the same size. The relation for the responses of contaminated corn extract injections is still differing from the responses of blank corn injections if a specific binding event was monitored successfully.

Reversibility

After every corn injection washing with PBS buffer is done to confirm that the signals are not originating from irreversible binding events on the surface. If the baseline level is reached again, all signals obtained from blank corn samples should then originate from a surface potential change (reversible). Finally the contaminated corn extracts were injected and the responses of the devices compared to obtain the difference which is then ascribed to the binding of AfB1 to the targeted antibodies. The difference of the response signals ($|I_{D1} - I_{D2}|$ or ΔI_D) from the FET with the target antibodies and the negative control should then give the signal portion corresponding to the specific binding of aflatoxin to the antibody on the targeted

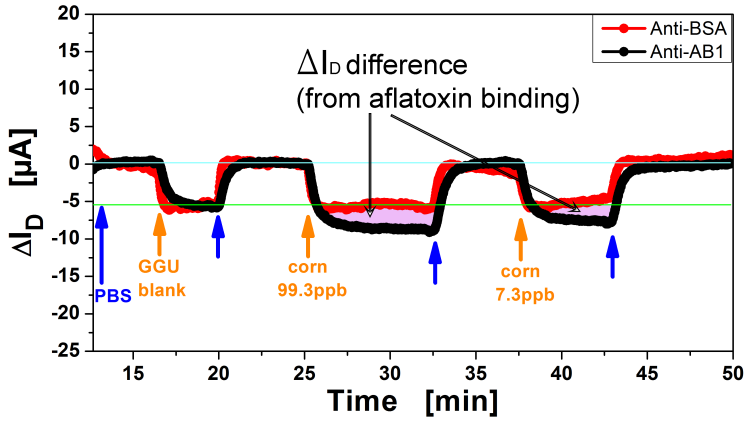

Figure 5.10: Array measurement of an uncontaminated corn reference sample (GGU blank) and two contaminated corn samples with AfB1 concentrations of 99.3 ppb (320 nM) and 7.3 ppb (23 nM) on a FET with targeted antibodies1 and a nontargeted FET with BSA antibodies. The pink area marks the response signal area, the blue horizontal line indicates the stable baseline level, while the green horizontal line shows the signal obtained by surface potential changes due to the injected corn extracts, which is in accordance to the response levels for the nontargeted FET.

FET (marked with a pink area in figure 5.10). As a proof of principle, for different measurements the sequence of contaminated sample injections with 7.3 ppb (23 nM) and 99.3 ppb (320 nM) was altered to proof that the detection signal is being independent of previous injections. This was verified by eight measurements, altering the sequence for every second and obtaining the same results independent of previous corn extract injections and a sample of two of those curves is shown in figure 5.11.

Response Signal Prefixes

Likewise to the detection-signal-prefix-change of AfB1 detection in buffer (see chapter 4.6.2), a response signal prefix change can also be observed in corn extracts. The specific signal from AfB1 binding to the antibody and the surface potential change due to corn extract injection are merged in the readout of the curves. When a prefix change occurs, the difference of the target FET and the negative control FET also has a negative prefix but the sensitivity is not affected. Because there is a negative control curve generated by the second FET in the array, a simple calculation of $|I_{D1} - I_{D2}|$ gives the response signal due to specific binding of AfB1 and indicates the presence of toxin in the solution. The response signal (again indicated by pink area) has the same characteristics, as in measurements with a positive overlap of signals, only the prefix changes and a demonstration of this effect is given in figure 5.11a,

where a positive ΔI_D is oserved and in figure 5.11b where ΔI_D is negative. This effect could be suppressed by using graphene with defined ratios of p- and n- dopands.

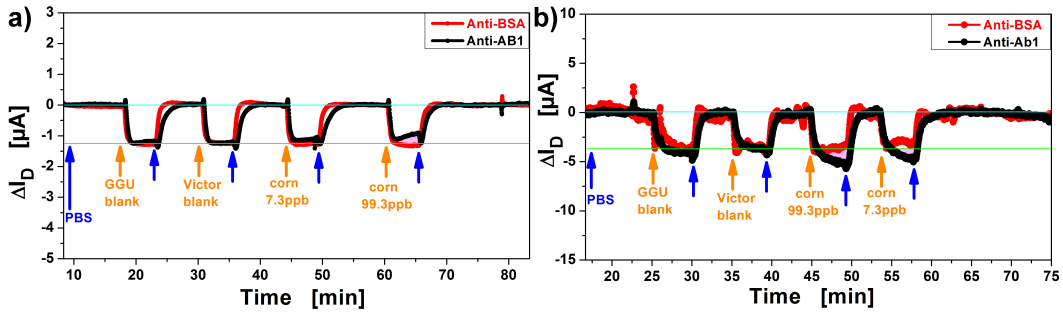

Figure 5.11: Test measurements with normalization of the baseline to the obtained signal levels from two different blank corn extract samples (GGU and Victor) with no AfB1, followed by the injection of contaminated samples: a) first, the low concentration (7.3 ppb or 23 nM) is tested, followed by the higher concentration (99.3 ppb or 320 nM), for both concentrations the baseline level is reached again. b) first the high concentration was tested, followed by the low concentration and again the signal regenerates to the baseline level. Although fabricated in the same batch with the same parameters, the devices used in measurement b display much higher noise ratios than the devices in a.

Noise Levels

The devices used for test measurements and the proof of principle for the array detection were fabricated using the same protocols and 30 nm of Ta_2O_5 layers. Anyhow, they have a variation in resistance from 300 Ω up to 3 000 Ω and different noise levels, which seem to be mostly independent of the resistance of the corresponding device. Only for very high resistances above 2 kΩ always a high noise level was observed. On the other hand, some FETs with lower resistances also display high noise levels (like the FETs in figure 5.11b, with resistances of 450 Ω and 300 Ω) in contrast to other devices with comparable resistance but much lower noise levels (like the FETs used in the measurement in figure 5.11a, with 280 Ω and 350 Ω). The reason for this effect could not be evaluated in the scope of this work, but the noise level was used for the calculation of the error bars for the detection signals in such way that higher noise levels also lowered the certainty of the obtained results and the error bars were constructed from multiplication of the mean noise level to the standard deviations obtained by integration of the area for the analysis of the response signals.

Negative Control Measurements

Negative control measurements have been performed using a FET sensor array with both devices being coated with 30 nm Ta_2O_5 and used without linker or antibody. The same corn extract solutions as in the experiments for specific sensing of AfB1 were used for the negative controls. Negative control measurements showed that the response signals for all solutions were overlapping for both FETs within an error range of up to 10 % of the response signal level (e.g. 120 nA for 1.8 μA response). This results can be interpreted for the determination of the LOD for AfB1 sensing using the FET array. The specific detection of aflatoxin was possible for concentrations of 7.3 ppb (23 nM) with a variation in response signals around 10 % in the worst cases. In regard to the results from the negative control measurements the LOD then is approximately lower than 7 ppb (22 nM). Therefore calculation of the LOD from the negative control measurements with use of antibody yields approximately the same results as for the negative controls without antibody – the LOD is found in the magnitude of very low ppb concentrations.

5.5.2 Measurement of a Calibration Curve for the Detection of Aflatoxin B1 from Corn Extracts

For the quantitative analysis of AfB1 concentrations from food samples, calibration curves have to be established first. These calibration curves would build the standards for comparisons of future detection, give proof of the system usability and demonstrate the device reproducibility. For measurement of the calibration curve 6 different corn samples were provided by Romer Labs® in the range from 5 ppb (16 nM) up to 99.8 ppb (320 nM), including a blank corn sample which was used for the normalization of the curves. The same basic sensing parameters and FET properties were used as for the measurements for the proof of principle in chapter 3.5.3. The signal strength was evaluated by integration over the time span of corn injection for the FETs immobilized with the AfB1 or BSA antibody. The obtained areas were subtracted one from the other and then plotted versus the AfB1 concentration. Since the area of the curve difference between two curves is intended to be the response signal, a device for time controlled injection of the analytes is needed. Only in that manner a exact comparability between two different injections is possible,

which is needed to fit a calibration curve with an error that is as low as possible. An automatic titration pump was used for the injection of every single concentration, so that the response signal length is always adjusted to exactly 300 seconds. In that way the responses of different injections stay comparable, because the area is always calculated from the response signal multiplied by the length of injection, which in this way is held constant. A calibration curve fulfilling the Langmuir theory is expected and the obtained responses are fitted onto that curve. Standard errors were obtained from integration over the area multiplied by the mean noise level of the curve. The noise in the I_DT curve is implying a large error when integrating over some curves, as discussed in chapter 5.5.1. Therefore additional noise reduction will be performed by using lower time-resolutions during the measurements, obtaining less data points, but averaging over the noise so that the resulting noise is lower than for high time resolutions.

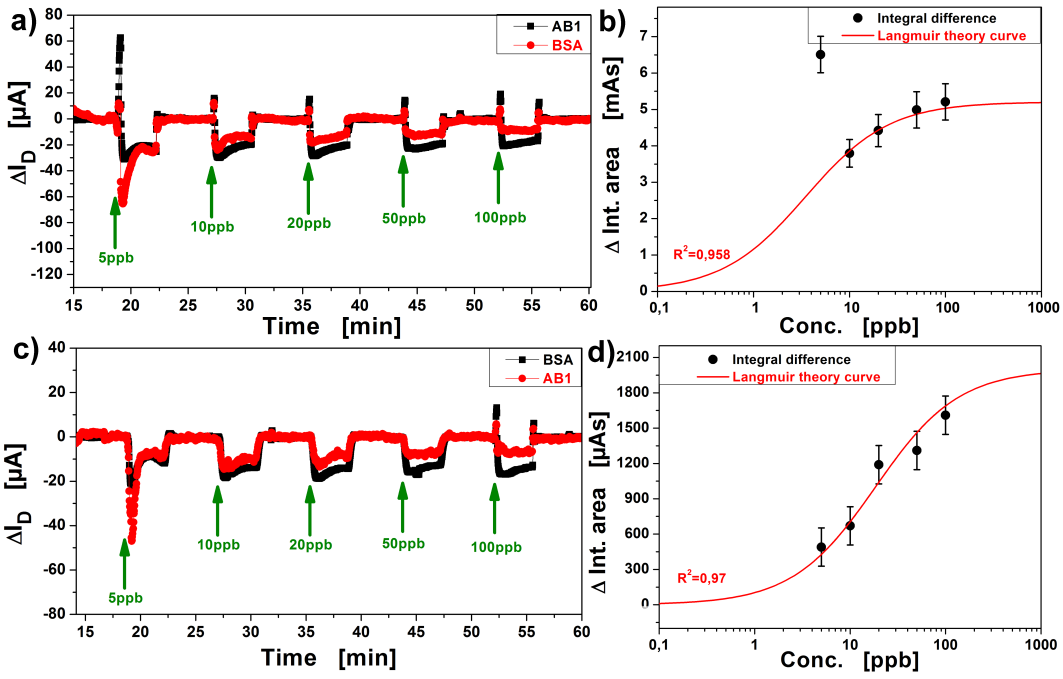

Figure 5.12: Two representative curves for the array detection of AfB1 contaminated corn extract samples containing concentrations from 5 ppb up to 100 ppb, corresponding to a range from 16 nM up to 320 nM. a) Normalized response curves of two FETs with resistances of 190 Ω (target) and 1 300 Ω (non-target). The response for 5 ppb is a outlier because of an air bubble, which caused the peak at the beginning of the injection (green arrow) and was not considered for the Langmuir evaluation. b) Langmuir isotherm for the measurement in figure a, using the difference in integral area as the response signal. c) Normalized response curves of two FETs with resistances of 1 100 Ω (target) and 120 Ω (non-target). d) Langmuir isotherm corresponding to the measurement in figure c.

From six array measurements, two of which are shown in figure 5.12, a calibration curve was fitted. Therefore all Langmuir isotherms obtained for separate measurements were plotted together in one figure and the non-weighted average was used as the calibration curve. The problem with the use of this approach are the divergent values for the saturation level. Since the calibration curve in the saturation regime is having a slope close to zero, a small variation in the response level for the injection of a unknown solution will give either no corresponding and valid concentration value (if the response is even incrementally higher than the saturation level) or will have a very high error (if the response is below the saturation level). Therefore such a calibration curve using the Langmuir theory curve is much more accurate at lower concentration, further away from the saturation regime. Since the main aim is not to quantify concentrations higher than the limits of non-toxic concentrations as given in the food safety regulations, a calibration for the lower concentrations already is satisfying the given requirements. The observed saturation level at around 100 ppb (320 nM) is too low for the evaluation using the USDA-GIPSA protocols, because of the limitations in accuracy emerging from the detection of concentrations in the saturation region, as described above. Therefore a optimization of the sensor has to be performed, adjusting V_G to a voltage in which the saturation is reached for higher concentration than 100 ppb (320 nM) only. Evaluating the shift in V_G necessary to obtain saturation at higher concentrations from the measurements of $I_D V_G$ curves in corn extracts from figure 8.12 it could be concluded that the outlook for better accuracy for higher concentrations would at the same time imply a shift in the LOD to higher values, which on the other hand would disqualify the sensor for competitive use due to this regard. A second approach to tackle this problem would be to use a different mathematical routine for the calibration curve itself, which until now was assumed to follow the kinetic analysis given by the Langmuir isotherm. A widely used approach is the use of a Rodbard function instead, which is supposed to overcome uncertainties from measurements much better [234]. In contrast to the Langmuir isotherm binding theory, the Rodbard function can't be deduced from physical or chemical backgrounds, but uses four distinct parameters which are not associated with any defined system properties. The function works for a wide range of application and is used for calibration curves for systems like immunoassays without the considerations of physical parameters implied in the function. It can be written in the form of:

$$y = \frac{a - d}{1 + (X/c)^b} + d \tag{5.1}$$

where a, b, c, d are the four parameters, y is the response variable and in this case x corresponds to the measured concentrations of the analyte. To obtain results for the response variable which can be written as the surface coverage of the FET in a meaningful range, the equation has to be adjusted in such way that the function converges towards 1 for increasing x. This can be achieved by setting the fitting paramter d = 1 and was done for the fitting of the calibration curve in the Rodbard model. Anyhow, the approach using the Rodbard function was also tried for the fitting of the obtained data and the construction of a calibration curve (Rodbard fit in figure 5.13). It is showing the same problem as for the Langmuir fit: for high concentrations the accuracy is decreased due to the low slope and therefore high error of readout in the saturation region.

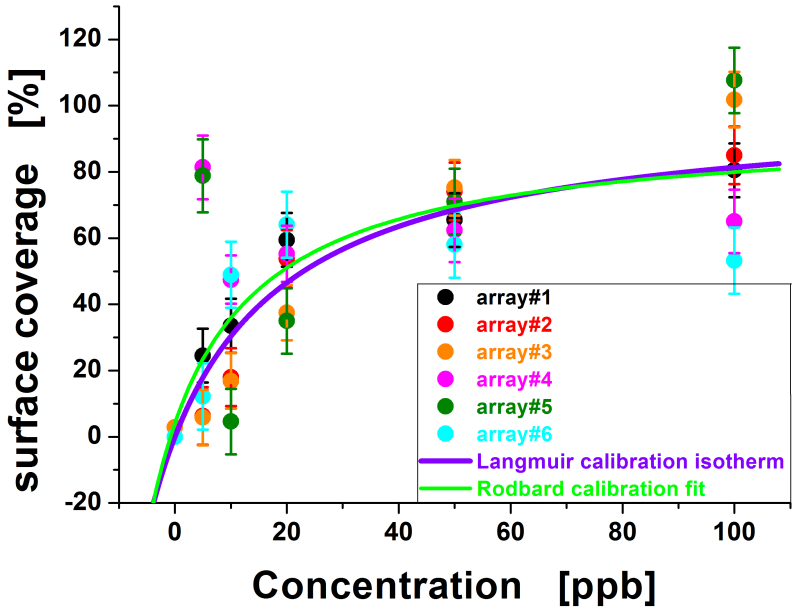

Figure 5.13: The response signals, calculated in surface coverage of the transistor from the saturation concentration against the corresponding injected concentrations of AfB1 in the corn extracts used for analysis. The violet curve is the best fitted Langmuir isotherm for all six array measurements, while the green curve shows the best fitted Rodbard function.

The slope of the Rodbard curve for lower concentrations is higher than for the Langmuir curve, which in comparison gives too low values with higher error for low

concentrations. On the other hand, the accuracy for the concentrations of 10, 20 and 50 ppb (32, 64 and 160 nM) is higher for the Rodbard fit than for the Langmuir isotherm, shown in figure 5.13. Because of these reasons, the results obtained for the measurements using the parameters and measurement like shown in figure 5.12 were used for comparison with the food safety legislation and can only be seen as a proof of principle for the construction of a label-free AfB1 sensor array based on rGO-FETs with a Ta_2O_5 passivation layer. Figure 5.13 shows the median of all Langmuir fits (violet curve) and Rodbard fits (light green curve) given in the six array measurements considered for the derivation of the calibration curve.

5.5.3 Evaluation of the established Setup following the USDA-GIPSA Requirements

As already discussed in chapter 5.5.2, a comparison to the USDA-GIPSA legislature for food safety protocols was performed for the evaluation of the applicability of the presented biosensor for the aflaoxin B1 analysis from food samples. Therefore the measured responses were handled as if they were unknown concentrations and then the respective concentration was calculated by comparison with the calibration curve. The values obtained in this manner were then again compared to the real injected concentration to evaluate the deviation and therefore the viability of the calibration curve as well. For all six arrays and five samples of corn extracts a total of 60 responses of FETs was measured and out of these 60 responses there were 6 outliers, disqualifying 4 of the the 30 total response signals, which have not been taken into account for the evaluation in this chapter. The outliers can mainly be assigned to air bubbles which create a strong but short change in the conductivity of the FET. During the short time they pass through the channel of the flow cell, the Gate electrode is cut off from the sensor surface due to displacement of the electrolyte. One of these outliers can be found in figure 5.12a. In the evaluation of the curve in figure 5.12b the response was not considered for the fitting of the Langmuir curve. Furthermore all results obtained in this manner were compared to the requirements stated by the food safety regulations, namely the USDA GIPSA protocol, which are shown in table 5.2.

The results from the evaluation of the six array measurements used for the demonstration of the sensor capabilities using the Langmuir isotherm as the calibration

Table 5.2: USDA-GIPSA requirements for AfB1 analysis

Conc. (ppb)	Max RSDi (%)	Stdev.	Range
5	25	1.25	2.5 - 7.5
10	22	2.2	5.6 - 14.4
20	20	4	12 - 28
50	n.a.	n.a.	n.a.
100	16	16	68 - 132

curve are shown in table 5.3, while the results when using the Rodbard function as the calibration curve are shown in table 5.4. It has to be taken into account that the toxin concentrations as given in the table are referring to the corn samples in solid state before extraction. The extraction efficiency was not taken into account for the evaluation of the data because it was still unknown. But it can be argued that the extraction efficiency is definitely lower than hundred percent and the recognised concentrations of AfB1 are even lower than the numbers given. To make sure that the LOD and sensitivity are not biased by wrong assumptions, the extraction efficiency was treated as if it was 100 % which leads to higher concentrations and therefore the presented sensitivity is worse than it would be after survey of the extraction efficiency.

The ranges and standard deviations found by the calibration curves in table 5.3 and table 5.4 exceed the allowed limits stated by the USDA GIPSA protocol. To evaluate the results in detail, first the results obtained by the Langmuir isotherm will be discussed.

Calibration using the Langmuir Isotherm

For the results obtained by calibration with the Langmuir isotherm it can clearly be seen that the mean value of the measured intervals has an offset to the actual expected concentration. For the 5 ppb (16 nM) injection a mean of 2.4 ppb (7.7 nM) was measured, for 10 ppb (32 nM) a mean of 4.8 ppb (15 nM), for 20 ppb (64 nM) a mean of 15.8 ppb (51 nM), for 50 ppb (160 nM) a mean of 31.4 ppb (101 nM) and for 100 ppb (320 nM) a mean value of 75.6 ppb (242 nM) was measured. For all concentrations the mean value found for the AfB1 concentration is found below the actually injected concentration, partially with a error of more than 50 %. This

Table 5.3: Results of the evaluation using the Langmuir isotherm as calibration curve.

Conc. (ppb)	Max RSDi (%)	Stdev.	Range
5	41	2.3	0.9 - 5.1
10	36	2.6	2.8 - 7.7
20	25	7.1	7.6 - 19.8
50	25	9.8	25.1 - 44.6
100	29	33.2	42.1 - 120.4

effect can't be ascribed to the extraction efficiency, because the extraction of the corn extract solutions was performed for all solutions simultaneously with the same parameters, so that it can safely be assumed that the efficiency is less than 100 % but constant for all solutions. Therefore, if the extraction efficiency would be taken into account, it would result in the shift the calibration curve to lower concentration but would not alter the shape and slope of the curve. To correct the offset from measured concentrations to injected ones in such manner that the mean would also be found at the desired value, the slope of the calibration curve would have to be smaller for low concentrations and therefore another calibration curve needs to be used. The high values of the Max RSDi are a direct consequence of the mean concentration offset of the measured responses, because the Max RSDi is calculated from the maximal deviation of the reponses to the expectancy, which would be smaller if the offset could be minimized. The standard deviation (Stdev.) is not affected by this effect, since it calculates relative values, independent of the expectancy value. Anyhow, comparing the standard deviations found in the performed experiments with the USDA-GIPSA requirements, still the Stdev. is about twice to high to fulfil the requirements.

Calibration using the Rodbard Function

Similar to the calibration using the Langmuir isotherm, the mean values for the detected concentrations have a offset from the actual concentrations. In detail the offset of the mean values from the expected values were 2.6 ppb (8 nM) for the 5 ppb (16 nM) concentration, 4.8 ppb (15 nM) for 10 ppb (32 nM) injection, 21.1 ppb (67 nM) where 20 ppb (64 nM) were expected, 44.9 ppb (144 nM) for the 50 ppb (160 nM) concentration and 122.2 ppb (391 nM) for 100 ppb (320 nM) concentration.

Table 5.4: Results of the evaluation using the Rodbard function as calibration curve.

Conc. (ppb)	Max RSDi (%)	Stdev.	Range
5	44	3	0.6 - 6.1
10	35	3.4	3.1 - 9.6
20	26	10.1	9.5 - 26.9
50	16	15.7	33.7 - 66.1
100	19	30.8	61.9 - 123.3

In total the offset for low concentrations is very similar to the offset obtained from the Langmuir calibration curve for low concentrations (5 ppb and 10 ppb), while the Rodbard function works better as a calibration curve for concentrations of 20, 50 and 100 ppb where the offset is in an acceptable range. Due to this reason also the Max RSDi values for the named concentrations are very close to the necessary range. On the other hand, the standard deviations obtained from the Rodbard function are higher for every concentration except for 100 ppb, being three times higher than necessary to fulfil the requirements of the USDA-GIPSA protocols.

Calibration Curve Efficiency

To conclude it can be said, that no suitable calibration curve was found for the fabricated FETs because the differences between the devices are significant when observing the saturation level concentration. Therefore a more normalized distribution of the saturation concentrations for different FETs has to be found. Up until this point all FET devices were fabricated using synthesized reduced graphene oxide, which leads to strong variations in the surface coverage with graphene. Since the surface coverage with graphene which is the transducing material has a significant impact in the saturation levels of the Langmuir curve, a more homogenous surface distribution could be advantageous.

Also the mean value for the obtained concentrations from the calibration curve in regard to each actually injected concentration, are not at the half of the stated interval. This indicates that the Langmuir isotherm and Rodbard function (despite it's accuracy in theory) may not be the ideal curves for the generation of a calibration curve, while the Rodbard function shows good accuracy for concentrations above 20 ppb (64 nM), but needs to be modified to fit better for even lower concentrations.

In direct comparison the Rodbard function is more applicable than the Langmuir isotherm, yielding lower offsets of the mean values, better ranges of measured concentrations but also worse standard deviations which can be ascribed to the lower slope of the fitted Rodbard function and therefore higher read-out intervals.

The fabricated devices in this work display worse sensitivity than most ELISA methods [165, 166] but better than some HPLC sensors [168] and not as sensitive as the best devices fabricated for the purpose of AfB1 detection. Anyhow, the sensitivity and selectivity of the device show the best outcome for the electronic detection of AfB1 to our knowledge. This may result from only very few applications which try to detect AfB1 using an electronic principle and therefore the presented approach demonstrates an innovation to the field of biosensing.

Chapter 6

Summary and Conclusions

Summary

In summary firstly graphene-oxide was synthesized using a variation of the Hummers method and a second type of rGO was obtained by collaboration with the university of Bayreuth. The graphene-oxide flake distribution on the silanized Si/SiO_2-wafers was optimized to obtain the best possible surface coverage by characterization of the distribution by SEM and SECM. The surface coverage found by SEM is estimated around 70 % with no significant overlaps of the graphene flakes. A suitable reducing agent was investigated by comparison of hydrazine and hydriodic acid and it was demonstrated that hydrazine is a better reduction agent but the surface is less damaged by the use of hydriodic acid. Source and Drain electrodes were then applied using thermal evaporation and the resulting rGO-FETs were measured for resistance, defining the suitable range of resistances used for biologial experiments. The electrochemical activity of the obtained rGO surfaces was evaluated by SECM measurements and thereby it was demonstrated that the geometry of the channel is suitable for randomly distributed graphene flakes to form a conductive bridge with high probability for the outcome of applicable devices with good resistances when using the described graphene oxide and 40 μm channel width. Further basic characterization was performed by measurements of ionic strengths and pH from buffer solutions and characterization of the electron and hole mobility in liquid-gated configuration. Furthermore the hysteresis effects of the FET devices was evaluated and it was found that only minor energy loss is occurring due to hysteresis measurements. Furthermore also the reversibility of the devices and the dependency on the

Debye length were demonstrated. The influence of the solutions flow speed when using liquid-gated configuration was experimentally evaluated and a logarithmic dependence of flow speed to the Source-Drain current was found. For the detection of aflatoxin B1 firstly the influence of solvents was tested using acetonitrile and Tween 20 at different buffer ion strengths to test the dependency of the response signals to the Debye length in regard to the concentrations of the used solvents. No influence of the solvents was observed and saturation of the transistor surface was found for concentrations in the micromolar concentration range. For the specific detection of aflatoxin B1, the corresponding antibodies were immobilized to the graphene surface using a PBSE linker and the binding kinetic were evaluated measuring titration curves. A binding affinity constant of $6x10^{-10}$ M was found, which is in good agreement with literature values. The LOD in buffer was found at approximately 30 pM. Unspecific binding was analysed and it could be demonstrated that binding of alfatoxin B1 to the graphene surface is happening if no linker molecules are attached to the surface, but as soon as the surface is functionalized with the linker and any protein, the unspecific binding is diminished due to a shielding effect of the linker. The specificity of the used antibodies was tested and it could be seen that the antibodies used in first place induce strong interactions with other non-targeted toxins. Therefore different suppliers of antibodies have been tested and a comparison of the specificities was performed, where it was seen that the monoclonal antibodies have the highest specifity but lowest detection signal strength, while polyclonal antibodies show much stronger signals but way less specificity. Due to the aimed measurements in real-life samples the monoclonal antibodies were chosen for further experimentation. As the next step different protective/passivation layers where tested in regard to the responses of the passivated FET to different corn extracts. Therefore impedance spectroscopy was used to evaluate the origin of the signals obtained by corn extract injections and it was shown that with high probability the major factor for the change of graphene conductivity when brought into contact with corn extracts is the change of ionic strength, which was calculated and measured for different grain types using a calibration curve obtained by titration of buffers with different ionic strengths. The results were compared to the responses seen for the injection of corn extracts in direct current mode. PEG, different aromatic molecules and metal oxides were tested as passivation layers by observation of the responses to the corn extracts under different Gate voltages. Ta_2O_5 showed the most promising results and also encapsulates the graphene surface completely from

the contact with the foodstuffs containing the analyte. The Ta_2O_5 layers were applied by reactive sputtering, characterized by CV, QCM-D and AFM measurements to evaluate the pinhole density and binding behaviour to the surface. A suitable linker was tested for the metal oxide surfaces, where GPTS showed the best properties, attaching the proteins to the surface via an epoxy group. To solve the problem of deconvolution of surface potential changes due to the used food extracts to the potential changes induced by specific binding events, an array configuration of two rGO-FETs was assembled and tested in buffer solutions. A mathematical validation of the used approach using the surface potential equation was presented and measurements from real-life corn foodstuffs contaminated with aflatoxin concentrations from 5 ppb (16 nM) to 100 ppb (320 nM) was performed for the presented array. The results were reproduced until satisfying amounts of data for the construction of a calibration curve have been obtained. The calibration curves were based on the Langmuir binding theory and the Rodbard fitting function and evaluated seperately. Thereby it was demonstrated that the Rodbard function gives results that are closer to satisfy the food safety legislature stated by the USDA-GIPSA protocols. Anyhow, the aimed LOD was achieved for the presented setup, but the variation in means of RMS and standard deviations when using the presented calibration curves could not satisfy the criteria of the food safety legislature. The deviations from the desired accuracy stated in the food safety legislature was about 30 % of the measured concentration error. Anyway the applicability of the presented biosensor was demonstrated, which also fulfills the desire of cost efficiency, sensitivity and selectivity for measurements in real-life food samples.

Conclusion

The presented approach for the fabrication of rGO based FETs has the advantage of good reproducibility of the results of the FET due to the chosen method for selection of the devices explained earlier in chapter 3.4.1. It further allows a theoretically prediction of the devices without the use of complex equipment like lithography during fabrication steps. At the same time fragile production steps, as it often is the case for manual positioning of the graphene flakes in other systems, are avoided. Other studies have demonstrated good reproducibility [235] but need a lot of effort for the positioning of the graphene and electrodes for the fabrication of a single device. Methods like CVD [236] allow easy material positioning due to the fact that large and

uniform films are obtained. In comparison to liquid-dispensed graphene much more bulky and cost intensive equipment is needed and the fabrication speed and number of devices fabricated at once is limited. The rGO from wet chemical synthesis used in this thesis is easy to apply and large numbers of devices can be fabricated at once, but the surface distribution of applied graphene sheets is not exactly controllable and results in mostly random distribution structures after the adsorption from the liquid onto the surface. The casting parameters can be optimized and the problem hence minimized because very uniform flake distributions can be obtained by the use of suitable rGO dilutions and rotation speeds for spin coating. Statistical balancing of the electronic properties of these randomly arrange rGO flakes is achieved by the choice of a relatively long conducting channel, which in our case was chosen to be 4 mm (hundredfold longer than the width). The approach used here is different to most standard methods where single flake are positioned exactly in the channel of the FET, which enables the use of small and short channels. For the FETs used in this work, the statistical balancing of the graphene-covered surface area over all separate graphene connections in the channel, achieved by the channel geometry, was investigated by SECM. Thereby the reproducibility of this procedure has been proven and demonstrated in chapter 3.4.2. The results show good reproducibility for the device fabrication with 68 $\pm$ 7 % of the surface being electrochemically active. The deviation of the devices obtained is comparable to other methods which need more costly equipment and have much higher production costs. Furthermore, the evaluation of the presented rGO-FETs in this work demonstrates that the ion strength and pH dependence of the response signals is linear and characterizes the shift of charge carrier type with pH. The measured dependency of 30 μS per pH is in good accordance with literature values for other ultrasensitive FETs [197]. A mathematical expression for the Drain current of the FETs was developed and compared to experimental results. The results were in good agreement with the mathematical formulation, which confirms the suitability of the theoretical considerations.

The biosensing capabilities were tested by sensing of BSA in different buffer solutions. Thereby the response dependence on Debye length was investigated at once. BSA concentrations of 10 μM were detected successfully and the dependence on the ionic strength showed good correspondence to the Debye theory. Considerations and experiments on the Debye length demonstrated that it can be used as a working parameter rather than a limiting factor, as it is the case for other publications. Furthermore, a logarithmic dependency of the flow speed on the I_D of the FETs was

demonstrated. The sensing capabilities of the sensor for Aflatoxin B1 have been successfully demonstrated in buffered solutions. The LOD found at 33 pm is not as low as for methods like ELISA or HPLC, but it has to be taken into account that in contrast to these methods the presented biosensor in this work could be used for portable, real-time measurements. Furthermore, the LOD found at 33 pm was measured with the use of antibodies supplied by Romer Labs®, while other measurements in this work have shown that monoclonal antibodies from Agrisera show much higher response signals. Therefore, it can be concluded that a significantly lower LOD could be found when using more sensitive antibodies. In the comparison to other liquid-gated FETs, only a publication for the detection of toxin were found. One of these devices utilizes carbon nanotube FETs with monoclonal antibodies for the specific detection of ϵ-toxin [237] and found a LOD of 2 nM in buffer. ϵ-toxin has a size of 33 kDa and is a much bigger molecule than AfB1. Furthermore, FET measurement based on silicon ninowires with the enhancement by gold nanoparticles have been used for the detection of aflatoxin B1 in other work [170]. The LOD found there was 3 nM in buffered solution by the use of the indirect competitive immunoassays. Both publications have higher LOD's than the biosensor presented in this work. A liquid-gated FET, based on AlGaN for the detection of botulinumtoxin (149 kDa) has been shown to have a LOD of 7 pM. The LOD is in the same range as the biosensor shown in this work, but in contrast to AfB1, botulinumtoxin is charged and a much bigger molecule, expected to induce a higher surface charge when binding. Another simililar device is the single walled carbon nanotubes paper biosensor for the detection of microcystin-LR (995 Da) [238]. The LOD in buffer was measured at 600 pM and is comparable to the device presented in this thesis.

For the measurements in real-life food samples, different antibodies were tested and the one with the highest specificity was chosen for further experiments. The choice was suitable to ensure the specific origin of response signals, but sensitivity would be increased with the use of other antibodies at the disadvantage of higher cross-reactivity. The use of metal oxides over chemical components for the passivation of the rGO was distinct. The experiments have clearly shown less non-specific signals for metal oxides with the disadvantage of lower sensitivity and conductivity of the FETs in comparison to other chemicals. The demonstration of binding signals being transduced through the metal oxide layer could have high impact for the future fabrications of biosensor FETs and is seen as a major result of this work. By measurements of corn samples it was demonstrated that a concentration of 20 nM

can be sensed by the array configuration of the FETs and the LOD in food samples is at least lower than that value. Other biosensors, e.g. single walled nanotube FETs for the detection of ϵ-toxin have shown a comparable LOD of 10 nM [237] and were passivated with PEG. In comparison these devices were operated with higher voltages and used for the sensing of a very large and charged molecule. Another carbon nanotube based FET was used for the direct sensing of *A.flavus* in rice [171]. That sensor was passivated with Tween20 and gelatine and showed a LOD of 10 μg *A.flavus* per 1 g of rice, which is a relatively high value in relation to the size of *A.flavus*. Hence it can be concluded that the sensor presented in this work shows the potential to overcome the sensing limitations of other electronic devices for the sensing of pathogens from foodstuffs. Anyhow, measurements of the calibration curve showed that a significant percentage of the devices exhibit problems in device stability due to the long measurement times for all seven concentrations of the calibration curve. Impurities in the corn extracts, air bubbles and other undesireble effects partially led to spikes in the device signals and therefore some measurements had to be considered as outliers and were not used for the statistical evaluation. The deviations for the food samples with the highest toxin concentrations were too high for fulfilment of the requirements of the food legislature. Anyhow, for the limitations explained, the RMSi and the standard deviations resulting from the calibration curves were close to the requirements (less than 30 % deviation) and could be optimized to fulfil the requirements by optimization of the system.

Chapter 7

Outlook

For future applications regarding the biosensing of Aflatoxin B1 with rGO FETs, more detailed studies of the passivation layer have to be performed. Due to high variety of metal oxides available, a deep analysis of different metal oxides has to be performed for the choice of the best suitable material. Furthermore, also alloys of metal oxides could be applied in different ratios to obtain the best possible transduction while further reducing unspecific signals. For further improvement, the linker molecules used on metal oxides could also be synthesized in such manner, that the bound protein is located closer to the surface, resulting in shorter Debye lengths and therefore higher sensitivity of the biosensors. A further improvement of the system would be a miniaturization of the measurement setup and FETs. Smaller channel widths than 40 μm would have a better reproduction rate when using rGO with partially random distribution. Therefore, the noise level of the devices is then minimized and the sensitivity increased, resulting in lower LOD's due to a better signal to noise ratio. Another approach to increase the sensitivity of the devices would be the use of antibodies with higher response rates and good selectivity. The discussion on the specificity of the antibodies in chapter 4.6.4 showed that for the same concentrations of the analyte, significantly different specific responses can be observed, depending on the immobilized antibody. Hence the use of a more sensitive antibody would also optimize the LOD and yield better statistical quality of the data for the concentration ranges used for the measurement of the calibration curve. Furthermore, a novel approach is the application of aptamers instead of antibodies [175], which showed promising results and could also be tested for the device presented in

this thesis. Signal amplification for graphene based FETs could be achieved by the use of indirect competitive immunoassays like methods utilizing gold nanoparticle for amplification [170]. Also the implementation of de-noising filters could optimize the statistical quality of the measured data. Thereby the requirements by the food legislatures could be satisfied more accurately. The development of portable devices is a long-term aim of this work, implying miniaturization and the availability of commercial micro-electronics. The criteria for an in-field sensor imply the use of defined configurations and high reproducibility of the device fabrication routine. Therefore an automatic fabrication of the rGO and the sputtered metal-oxide layers would be needed to minimize the variations caused by user handling.

Chapter 8

Appendix

For better overview of the data and reading flow, several data sets have been moved to this chapter and are referenced in the text accordingly. Anyhow, only data sets with further significance have been printed in this chapter, omitting reproduction data and curves with low scientific output. However, data sets including or demonstrating the reversibility of a measurement, the functionality under different set-up conditions or working materials are shown in this section for a thoroughly investigation of the topic.

Measurements in buffered solutions

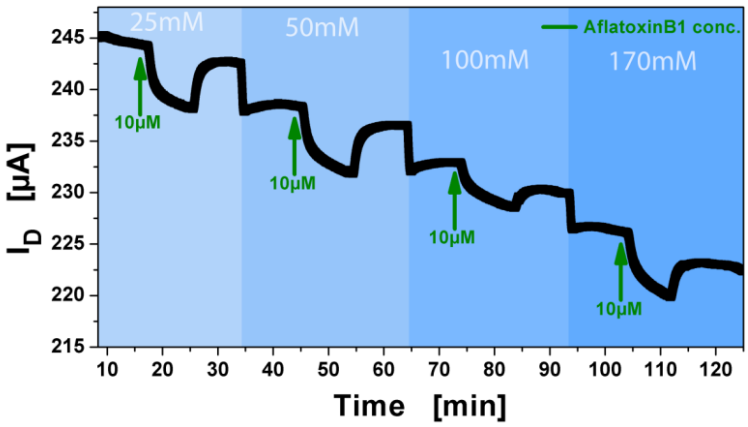

Figure 8.1: A 10 μM concentration of AfB1 was detected in PBS buffer of different ionic strengths, starting with low concentrations. The blue areas in the graphic mark the region within the corresponding ionic strengths. A stronger response for a 10 μM AfB1 concentration is observed in electrolytes with lower ion strengths as stated by the Debye length theory.

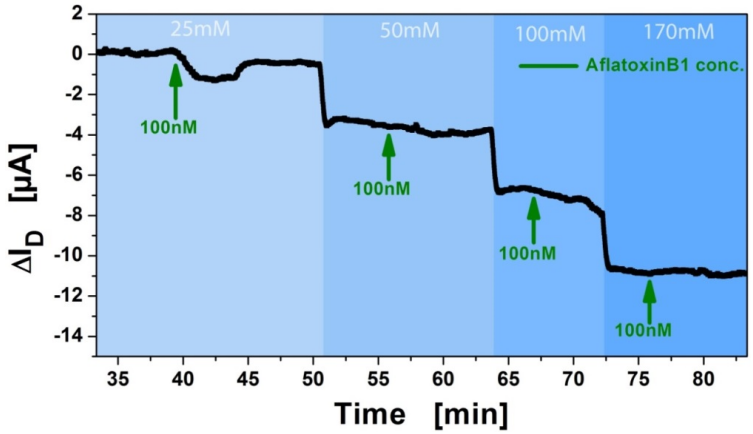

Figure 8.2: Aflatoxin B1 detection in PBS buffers of variable ion strength with an addition of 1 % Tween in all solutions. Again a 100 nM toxin concentration was tested and could be detected only for 25 mM ionic buffer.

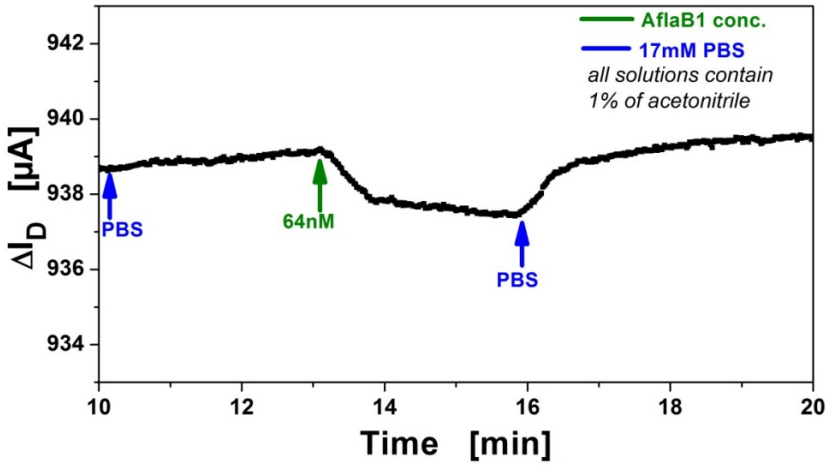

Figure 8.3: For the analysis of the binding affinity of aflatoxins on bare graphene surfaces test measurements were performed using blank FETs. Signal strengths for nanomolar concentrations were found to be only around 10 % than for the measurements where the target antibody was used.

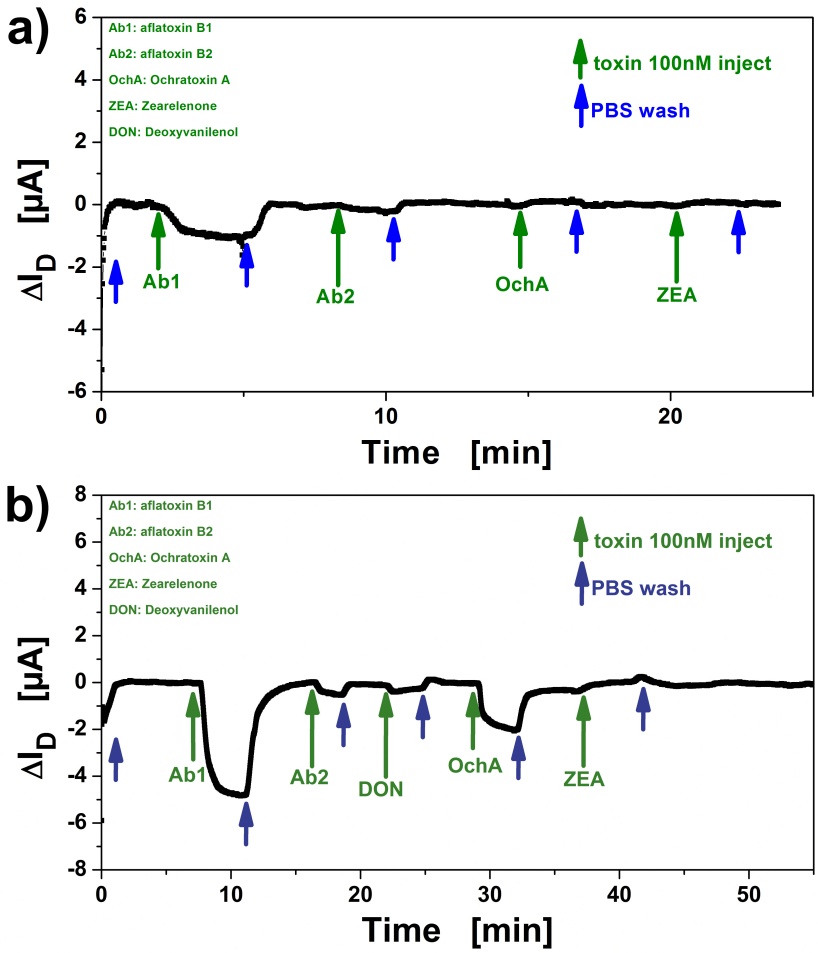

Figure 8.4: Cross-selectivity measurements of a graphene FETs with: a) Santa Cruz monoclonal antibodies. A response of 1.2 μA is obtained for AfB1, while no responses are observed for the other toxins. b) Agrisera polyclonal antibodies. A response of 5.3 μA is observed for AfB1. The other toxins also interact with the antibody, with ochratoxin A showing the strongest unspecific response.

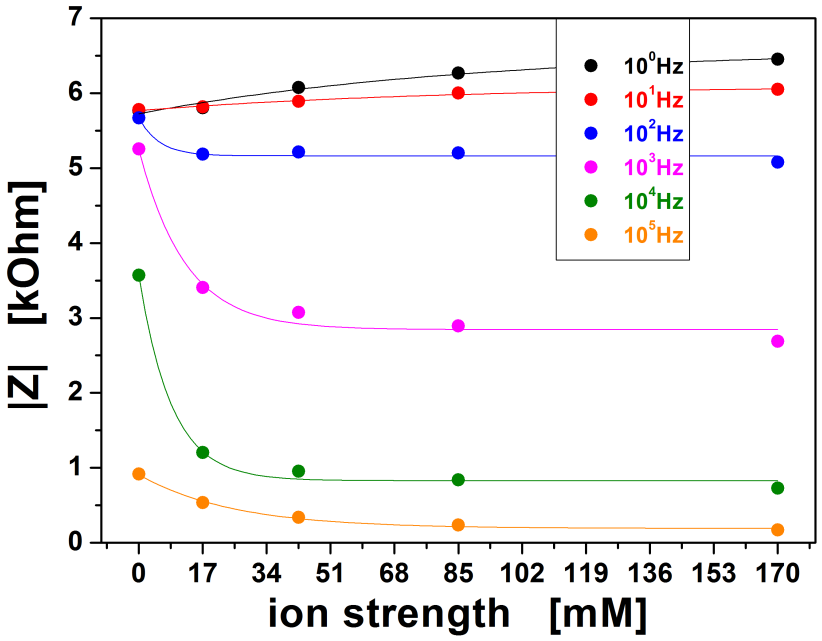

Figure 8.5: The responses for different frequencies for the measurement shown in figure 4.3. The lines are simple exponential fits over the data and converge with a R^2 of 0.99, which points to an exponential dependency of the ionic strength to the corresponding response signal.

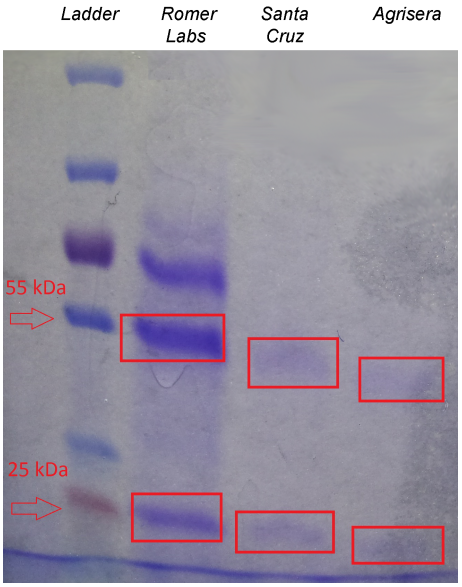

Figure 8.6: SDS page for the purified Romer Labs antibody and for the commercially obtained Santa Cruz and Agrisera antibodies. It can be seen that also after purification the Romer Labs antibodies contain significant amounts of molecules with molecular sizes not corresponding to antibodies. The commercial products show only sizes of around 55 kDa and 25 kDa, which are in the expected range.

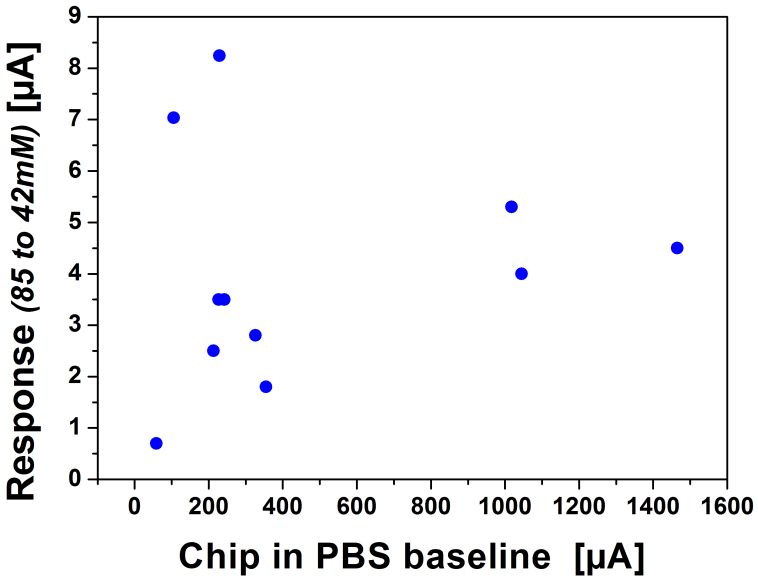

Figure 8.7: Baseline level in relationship with the responses obtained from a change of the buffer's ionic strength from 85 mM to 42 mM. V_G was set to 0 V and a I_{DS} of 200 mV were used. No clear dependency can be observed, meaning that the resistivity of the graphene FETs in not defining the sensitivity to ionic changes.

Figure 8.8: Pictures of the different grain types used for analysis. Extraction was performed according to the standard protocol, described in chapter 3.2.1.

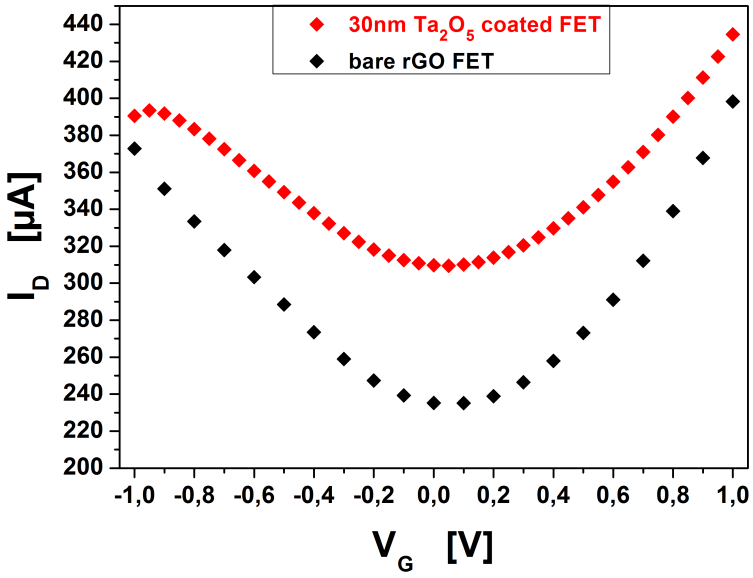

Figure 8.9: $I_D V_G$ curves of a rGO FET withour passivation coating (black) and a 30 nm Ta_2O_5-coated FET (red). Two different devices with similar resistance were chosen for this comparison. A decrease of charge mobilities can be observed for the Ta_2O_5-coated FET can be observed. The mobilities for this device are $\mu_{e\text{-}} = 18\,000$ cm^2/Vs and $\mu_{holes} = 28\,100$ cm^2/Vs, which is lower than for the bare rGO FET, where the mobilities are $\mu_{e\text{-}} = 25\,800$ cm^2/Vs and $\mu_{holes} = 39\,200$ cm^2/Vs. The mobility is therefore decreased ≈50%.

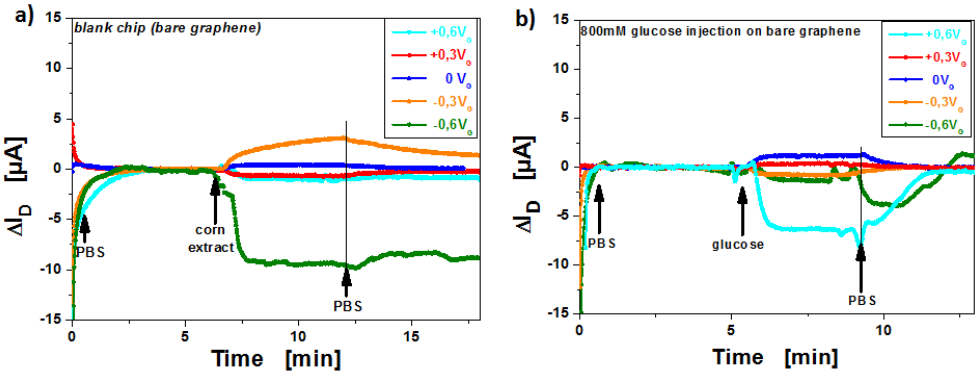

Figure 8.10: Responses of a blank graphene FET with no passivation layer to a) corn extracts as used as the matrix for the detection of aflatoxin B1 and b) injections of 800 mM glucose in PBS buffer. The responses obtained for different Gate potentials are not comparable for the responses of corn and glucose, indicating that the glucose parts in the corn samples don't have a significant effect. The response signal strength is very comparable for both materials, but 800 mM is a by far higher concentration than can be expected in the corn solutions.

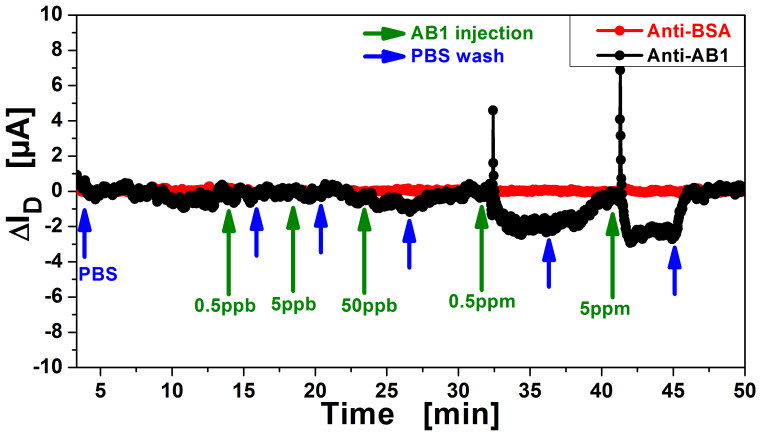

Figure 8.11: Titration of Aflatoxin B1 concentrations from 0.5 ppb (1.6 nM) up to 5 ppm (16 μM) in array configuration. The LOD for this measurement is found around 50 ppb (160 nM) for responses with negative signal change, while the higher concentrations give negative response signals for the used Gate voltage. This effect is ascribed to the crossing points of the characteristic curves in the $I_D V_G$ graphs.

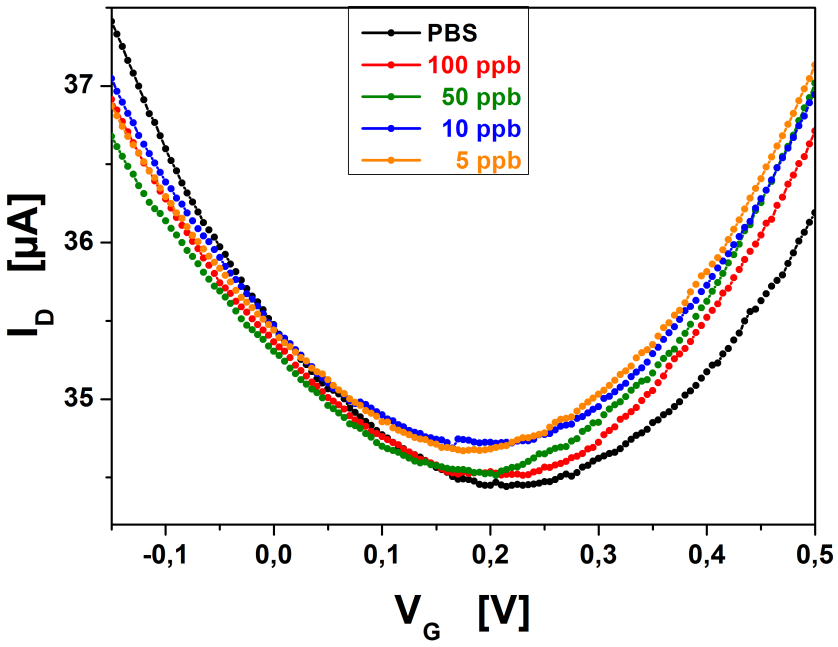

Figure 8.12: $I_D V_G$ measurements of a Ta_2O_5-passivated rGO FET immobilized with target aflatoxin B1 antibodies form corn extracts. The first curve is measured in PBS buffer without any toxin contamination, while the remaining four curves were measured for the corn extracts and also used for the measurements and detection of aflatoxin B1 for the construction of a calibration curve.

Bibliography

[1] C. Reiner-Rozman, M. Larisika, C. Nowak, and W. Knoll, "Graphene-based liquid-gated field effect transistor for biosensing: Theory and experiments," *Biosensors and Bioelectronics*, vol. 70, pp. 21 – 27, 2015.

[2] "Rippling and fracture of graphene," http://chaos.utexas.edu/people/faculty/michael-p-marder/rippling-of-graphene.

[3] B. C. Brodie, "On the Atomic Weight of Graphite," *Philosophical Transactions of the Royal Society of London*, vol. 149, pp. 249–259, Jan. 1859.

[4] W. Bragg, "The structure of the spinel group of crystals," *Philosophical Magazine Series 6*, vol. 30, no. 176, pp. 305–315, 1915.

[5] S. P. Debye, P., "Ueber die konstitution von graphit und amorpher kohle," *Nachrichten von der Gesellschaft der Wissenschaften zu Göttingen, Mathematisch-Physikalische Klasse*, vol. 1917, pp. 180–188, 1917.

[6] J. D. Bernal, "The Structure of Graphite," *Proceedings of the Royal Society of London. Series A, Containing Papers of a Mathematical and Physical Character*, vol. 106, no. 740, pp. 749–773, 1924.

[7] D. Haar, *Collected Papers of L.D. Landau*. Elsevier Science, 2013.

[8] R. Peierls, "Quelques propriétés typiques des corps solides," *Annales de l'institut Henri Poincaré*, vol. 5, no. 3, pp. 177–222, 1935.

[9] N. D. Mermin and H. Wagner, "Absence of ferromagnetism or antiferromagnetism in one- or two-dimensional isotropic heisenberg models," *Phys. Rev. Lett.*, vol. 17, pp. 1133–1136, Nov 1966.

[10] P. C. Hohenberg, "Existence of long-range order in one and two dimensions," *Phys. Rev.*, vol. 158, pp. 383–386, Jun 1967.

[11] J. Fröhlich and C. Pfister, "On the absence of spontaneous symmetry breaking and of crystalline ordering in two-dimensional systems," *Comm. Math. Phys.*, vol. 81, no. 2, pp. 277–298, 1981.

[12] N. N. Bogoliubov, *Abhandlungen aus der Sowjetunion*, vol. 6, pp. 229–231, 1962.

[13] H. P. Boehm, A. Clauss, G. O. Fischer, and U. Hofmann, "Das adsorptionsverhalten sehr dünner kohlenstoff-folien," *Zeitschrift für anorganische und allgemeine Chemie*, vol. 316, no. 3-4, pp. 119–127, 1962.

[14] P. R. Wallace, "The band theory of graphite," *Phys. Rev.*, vol. 71, pp. 622–634, May 1947.

[15] W. S. Hummers and R. E. Offeman, "Preparation of Graphitic Oxide," *Journal of the American Chemical Society*, vol. 80, no. 6, pp. 1339–1339, Mar. 1958.

[16] E. D.P., DiVincenzo and Mele, "Self-consistent effective-mass theory for intralayer screening in graphite intercalation compounds," *Phys. Rev. B*, vol. 29, pp. 1685–1694, Feb 1984.

[17] K. S. Novoselov, A. K. Geim, S. V. Morozov, D. Jiang, Y. Zhang, S. V. Dubonos, I. V. Grigorieva, and A. A. Firsov, "Electric Field Effect in Atomically Thin Carbon Films," *Science*, vol. 306, no. 5696, pp. 666–669, Oct. 2004.

[18] K. S. Novoselov, D. Jiang, F. Schedin, T. J. Booth, V. V. Khotkevich, S. V. Morozov, and A. K. Geim, "Two-dimensional atomic crystals," *Proceedings of the National Academy of Sciences of the United States of America*, vol. 102, no. 30, pp. 10 451–10 453, Jul. 2005.

[19] A. K. Geim and K. S. Novoselov, "The rise of graphene," *Nat Mater*, vol. 6, no. 3, pp. 183–191, Mar. 2007.

[20] A. Fasolino, J. H. Los, and M. I. Katsnelson, "Intrinsic ripples in graphene," *Nat Mater*, vol. 6, no. 11, pp. 858–861, Nov. 2007.

[21] S. Park, J. An, J. R. Potts, A. Velamakanni, S. Murali, and R. S. Ruoff, "Hydrazine-reduction of graphite- and graphene oxide," *Carbon*, vol. 49, no. 9, pp. 3019 – 3023, 2011.

[22] X. Huang, X. Qi, F. Boey, and H. Zhang, "Graphene-based composites," *Chem. Soc. Rev.*, vol. 41, no. 2, pp. 666–686, 2012.

[23] M. J. Fernández-Merino, L. Guardia, J. I. Paredes, S. Villar-Rodil, P. Solís-Fernández, A. Martínez-Alonso, and J. M. D. Tascón, "Vitamin C Is an Ideal Substitute for Hydrazine in the Reduction of Graphene Oxide Suspensions," *The Journal of Physical Chemistry C*, vol. 114, no. 14, pp. 6426–6432, Apr. 2010.

[24] J. Zhang, H. Yang, G. Shen, P. Cheng, J. Zhang, and S. Guo, "Reduction of graphene oxide vial-ascorbic acid," *Chem. Commun.*, vol. 46, no. 7, pp. 1112–1114, 2010.

[25] G. Williams, B. Seger, and P. V. Kamat, "TiO2-Graphene Nanocomposites. UV-Assisted Photocatalytic Reduction of Graphene Oxide," *ACS Nano*, vol. 2, no. 7, pp. 1487–1491, Jul. 2008.

[26] W. Chen, L. Yan, and P. R. Bangal, "Preparation of graphene by the rapid and mild thermal reduction of graphene oxide induced by microwaves," *Carbon*, vol. 48, no. 4, pp. 1146–1152, Apr. 2010.

[27] S. Pei and H.-M. Cheng, "The reduction of graphene oxide," *Festschrift dedicated to Peter A. Thrower, Editor-in-Chief, 1972 - 2012*, vol. 50, no. 9, pp. 3210–3228, Aug. 2012.

[28] C. Miao, C. Zheng, O. Liang, and Y.-H. Xie, *Chemical vapor deposition of graphene*. INTECH Open Access Publisher, 2011.

[29] C. Mattevi, H. Kim, and M. Chhowalla, "A review of chemical vapour deposition of graphene on copper," *Journal of Materials Chemistry*, vol. 21, no. 10, pp. 3324–3334, 2011.

[30] B. Wang, X. Ma, M. Caffio, R. Schaub, and W.-X. Li, "Size-selective carbon nanoclusters as precursors to the growth of epitaxial graphene," *Nano Letters*, vol. 11, no. 2, pp. 424–430, 2011, pMID: 21247214.

[31] W. Guo, H. Li, M. Li, W. Dai, Z. Shao, X. Wu, and B. Yang, "Synthesis of nickel nanosheet/graphene composites for biosensor applications," *Carbon*, vol. 79, pp. 636–645, 2014.

[32] A. Pirkle, J. Chan, A. Venugopal, D. Hinojos, C. Magnuson, S. McDonnell, L. Colombo, E. Vogel, R. Ruoff, and R. Wallace, "The effect of chemical residues on the physical and electrical properties of chemical vapor deposited graphene transferred to sio2," *Applied Physics Letters*, vol. 99, no. 12, p. 122108, 2011.

[33] D. A. Brownson and C. E. Banks, "Cvd graphene electrochemistry: the role of graphitic islands," *Physical Chemistry Chemical Physics*, vol. 13, no. 35, pp. 15 825–15 828, 2011.

[34] J. Lee, J. Baek, G. H. Ryu, M. J. Lee, S. Oh, S. K. Hong, B.-H. Kim, S.-H. Lee, B. J. Cho, Z. Lee *et al.*, "High-angle tilt boundary graphene domain recrystallized from mobile hot-wire-assisted chemical vapor deposition system," *Nano letters*, vol. 14, no. 8, pp. 4352–4359, 2014.

[35] H. Tetlow, J. P. De Boer, I. Ford, D. Vvedensky, J. Coraux, and L. Kantorovich, "Growth of epitaxial graphene: theory and experiment," *Physics Reports*, vol. 542, no. 3, pp. 195–295, 2014.

[36] X. Wang and Y. Shi, "Fabrication techniques of graphene nanostructures," 2014.

[37] C. Lee, X. Wei, J. W. Kysar, and J. Hone, "Measurement of the elastic properties and intrinsic strength of monolayer graphene," *science*, vol. 321, no. 5887, pp. 385–388, 2008.

[38] H.-S. P. Wong and D. Akinwande, *Carbon nanotube and graphene device physics*. Cambridge University Press, 2011.

[39] K. I. Bolotin, K. Sikes, Z. Jiang, M. Klima, G. Fudenberg, J. Hone, P. Kim, and H. Stormer, "Ultrahigh electron mobility in suspended graphene," *Solid State Communications*, vol. 146, no. 9, pp. 351–355, 2008.

[40] A. K. Geim and K. S. Novoselov, "The rise of graphene," *Nature materials*, vol. 6, no. 3, pp. 183–191, 2007.

[41] K. Rytkönen, J. Akola, and M. Manninen, "Density functional study of alkali-metal atoms and monolayers on graphite (0001)," *Phys. Rev. B*, vol. 75, p. 075401, Feb 2007.

[42] S. Adam and S. D. Sarma, "Transport in suspended graphene," *Solid State Communications*, vol. 146, no. 9, pp. 356–360, 2008.

[43] P. Y. Huang, C. S. Ruiz-Vargas, A. M. van der Zande, W. S. Whitney, M. P. Levendorf, J. W. Kevek, S. Garg, J. S. Alden, C. J. Hustedt, Y. Zhu *et al.*, "Grains and grain boundaries in single-layer graphene atomic patchwork quilts," *Nature*, vol. 469, no. 7330, pp. 389–392, 2011.

[44] F. Banhart, J. Kotakoski, and A. V. Krasheninnikov, "Structural defects in graphene," *ACS nano*, vol. 5, no. 1, pp. 26–41, 2010.

[45] X. Feng, S. Maier, and M. Salmeron, "Water splits epitaxial graphene and intercalates," *Journal of the American Chemical Society*, vol. 134, no. 12, pp. 5662–5668, 2012.

[46] K. S. Novoselov, A. K. Geim, S. V. Morozov, D. Jiang, M. I. Katsnelson, I. V. Grigorieva, S. V. Dubonos, and A. A. Firsov, "Two-dimensional gas of massless Dirac fermions in graphene," *Nature*, vol. 438, no. 7065, pp. 197–200, Nov. 2005.

[47] E. Henriksen, Z. Jiang, L.-C. Tung, M. Schwartz, M. Takita, Y.-J. Wang, P. Kim, and H. Stormer, "Cyclotron resonance in bilayer graphene," *Physical review letters*, vol. 100, no. 8, p. 087403, 2008.

[48] A. S. Mayorov, R. V. Gorbachev, S. V. Morozov, L. Britnell, R. Jalil, L. A. Ponomarenko, P. Blake, K. S. Novoselov, K. Watanabe, T. Taniguchi, and A. K. Geim, "Micrometer-Scale Ballistic Transport in Encapsulated Graphene at Room Temperature," *Nano Letters*, vol. 11, no. 6, pp. 2396–2399, Jun. 2011.

[49] J. Baringhaus, M. Ruan, F. Edler, A. Tejeda, M. Sicot, A. T. Ibrahimi, Z. Jiang, E. Conrad, C. Berger, C. Tegenkamp *et al.*, "Exceptional ballistic transport in epitaxial graphene nanoribbons," *arXiv preprint arXiv:1301.5354*, 2013.

[50] W. Yang, K. R. Ratinac, S. P. Ringer, P. Thordarson, J. J. Gooding, and F. Braet, "Carbon nanomaterials in biosensors: should you use nanotubes or

graphene?" *Angewandte Chemie International Edition*, vol. 49, no. 12, pp. 2114–2138, 2010.

[51] E. V. Castro, K. S. Novoselov, S. V. Morozov, N. M. R. Peres, J. M. B. L. dos Santos, J. Nilsson, F. Guinea, A. K. Geim, and A. H. C. Neto, "Biased Bilayer Graphene: Semiconductor with a Gap Tunable by the Electric Field Effect," *Physical Review Letters*, vol. 99, no. 21, p. 216802, Nov. 2007.

[52] M. Breusing, C. Ropers, and T. Elsaesser, "Ultrafast carrier dynamics in graphite," *Physical review letters*, vol. 102, no. 8, p. 086809, 2009.

[53] M. Craciun, S. Russo, M. Yamamoto, J. B. Oostinga, A. Morpurgo, and S. Tarucha, "Trilayer graphene is a semimetal with a gate-tunable band overlap," *Nature nanotechnology*, vol. 4, no. 6, pp. 383–388, 2009.

[54] E. J. Santos and E. Kaxiras, "Electric-field dependence of the effective dielectric constant in graphene," *Nano letters*, vol. 13, no. 3, pp. 898–902, 2013.

[55] A. Ambrosi, C. K. Chua, A. Bonanni, and M. Pumera, "Electrochemistry of graphene and related materials," *Chemical Reviews*, vol. 114, no. 14, pp. 7150–7188, 2014.

[56] L. Malard, M. Pimenta, G. Dresselhaus, and M. Dresselhaus, "Raman spectroscopy in graphene," *Physics Reports*, vol. 473, no. 5–6, pp. 51–87, Apr. 2009.

[57] A. T. Valota, I. A. Kinloch, K. S. Novoselov, C. Casiraghi, A. Eckmann, E. W. Hill, and R. A. Dryfe, "Electrochemical behavior of monolayer and bilayer graphene," *ACS nano*, vol. 5, no. 11, pp. 8809–8815, 2011.

[58] A. Ambrosi, A. Bonanni, Z. Sofer, J. S. Cross, and M. Pumera, "Electrochemistry at chemically modified graphenes," *Chemistry–A European Journal*, vol. 17, no. 38, pp. 10 763–10 770, 2011.

[59] J. Xia, F. Chen, J. Li, and N. Tao, "Measurement of the quantum capacitance of graphene," *Nature nanotechnology*, vol. 4, no. 8, pp. 505–509, 2009.

[60] H. L. Poh, F. Šaněk, A. Ambrosi, G. Zhao, Z. Sofer, and M. Pumera, "Graphenes prepared by staudenmaier, hofmann and hummers methods with consequent thermal exfoliation exhibit very different electrochemical properties," *Nanoscale*, vol. 4, no. 11, pp. 3515–3522, 2012.

[61] D. R. Dreyer, S. Park, C. W. Bielawski, and R. S. Ruoff, "The chemistry of graphene oxide," *Chem. Soc. Rev.*, vol. 39, pp. 228–240, 2010.

[62] F. Schedin, A. Geim, S. Morozov, E. Hill, P. Blake, M. Katsnelson, and K. Novoselov, "Detection of individual gas molecules adsorbed on graphene," *Nature materials*, vol. 6, no. 9, pp. 652–655, 2007.

[63] A. Inaba, K. Yoo, Y. Takei, K. Matsumoto, and I. Shimoyama, "Ammonia gas sensing using a graphene field–effect transistor gated by ionic liquid," *Sensors and Actuators B: Chemical*, vol. 195, pp. 15–21, May 2014.

[64] C. Wang, L. Zhang, Z. Guo, J. Xu, H. Wang, K. Zhai, and X. Zhuo, "A novel hydrazine electrochemical sensor based on the high specific surface area graphene," *Microchimica Acta*, vol. 169, no. 1-2, pp. 1–6, Apr. 2010.

[65] K. Alexandrou, N. Petrone, J. Hone, and I. Kymissis, "Encapsulated graphene field-effect transistors for air stable operation," *Applied Physics Letters*, vol. 106, no. 11, pp. –, 2015.

[66] X. Wang, S. M. Tabakman, and H. Dai, "Atomic layer deposition of metal oxides on pristine and functionalized graphene," *Journal of the American Chemical Society*, vol. 130, no. 26, pp. 8152–8153, 2008.

[67] G. F. Schneider, Q. Xu, S. Hage, S. Luik, J. N. Spoor, S. Malladi, H. Zandbergen, and C. Dekker, "Tailoring the hydrophobicity of graphene for its use as nanopores for dna translocation," *Nature communications*, vol. 4, 2013.

[68] R. K. Layek and A. K. Nandi, "A review on synthesis and properties of polymer functionalized graphene," *Polymer*, vol. 54, no. 19, pp. 5087–5103, 2013.

[69] C. G. Kang, Y. G. Lee, S. K. Lee, E. Park, C. Cho, S. K. Lim, H. J. Hwang, and B. H. Lee, "Mechanism of the effects of low temperature al 2 o 3 passivation on graphene field effect transistors," *Carbon*, vol. 53, pp. 182–187, 2013.

[70] A. ZurutuzaáElorza *et al.*, "Highly air stable passivation of graphene based field effect devices," *Nanoscale*, vol. 7, no. 8, pp. 3558–3564, 2015.

[71] Y. Fan, X. Yang, C. Yang, and J. Liu, "Au-tio2/graphene nanocomposite film for electrochemical sensing of hydrogen peroxide and nadh," *Electroanalysis*, vol. 24, no. 6, pp. 1334–1339, 2012.

[72] D. Khatayevich, T. Page, C. Gresswell, Y. Hayamizu, W. Grady, and M. Sarikaya, "Selective detection of target proteins by peptide-enabled graphene biosensor," *Small*, vol. 10, no. 8, pp. 1505–1513, 2014.

[73] G.-X. Zhong, P. Wang, F.-H. Fu, S.-H. Weng, W. Chen, S.-G. Li, A.-L. Liu, Z.-Y. Wu, X. Zhu, X.-H. Lin *et al.*, "Electrochemical immunosensor for detection of topoisomerase based on graphene–gold nanocomposites," *Talanta*, vol. 125, pp. 439–445, 2014.

[74] A. Pattammattel, C. L. Williams, P. Pande, W. G. Tsui, A. K. Basu, and C. V. Kumar, "Biological relevance of oxidative debris present in as-prepared graphene oxide," *RSC advances*, vol. 5, no. 73, pp. 59 364–59 372, 2015.

[75] B. Long, M. Manning, M. Burke, B. N. Szafranek, G. Visimberga, D. Thompson, J. C. Greer, I. M. Povey, J. MacHale, G. Lejosne *et al.*, "Non-covalent functionalization of graphene using self-assembly of alkane-amines," *Advanced Functional Materials*, vol. 22, no. 4, pp. 717–725, 2012.

[76] W. Qiu, P. D. Nguyen, and E. Skafidas, "Graphene nanopores as negative differential resistance devices," *Journal of Applied Physics*, vol. 117, no. 5, p. 054306, 2015.

[77] W. Fu, C. Nef, A. Tarasov, M. Wipf, R. Stoop, O. Knopfmacher, M. Weiss, M. Calame, and C. Schönenberger, "High mobility graphene ion-sensitive field-effect transistors by noncovalent functionalization," *Nanoscale*, vol. 5, no. 24, pp. 12 104–12 110, 2013.

[78] M. Munz, C. E. Giusca, R. L. Myers-Ward, D. K. Gaskill, and O. Kazakova, "Thickness-dependent hydrophobicity of epitaxial graphene," *ACS nano*, vol. 9, no. 8, pp. 8401–8411, 2015.

[79] D. Berman, A. Erdemir, and A. V. Sumant, "Graphene: a new emerging lubricant," *Materials Today*, vol. 17, no. 1, pp. 31–42, 2014.

[80] I. Strauss, H. Chan, and P. Kral, "Ultralong polarization chains induced by ions solvated in confined water monolayers," *Journal of the American Chemical Society*, vol. 136, no. 4, pp. 1170–1173, 2014.

[81] N. Greenwood and A. Earnshaw, *Chemistry of the Elements*. Elsevier Science, 2012.

[82] G. Algara-Siller, O. Lehtinen, F. Wang, R. Nair, U. Kaiser, H. Wu, A. Geim, and I. Grigorieva, "Square ice in graphene nanocapillaries," *Nature*, vol. 519, no. 7544, pp. 443–445, 2015.

[83] Z. Qian and G. Wei, "Electric-field-induced phase transition of confined water nanofilms between two graphene sheets," *The Journal of Physical Chemistry A*, vol. 118, no. 39, pp. 8922–8928, 2014.

[84] S. F. Braga, V. R. Coluci, S. B. Legoas, R. Giro, D. S. Galvão, and R. H. Baughman, "Structure and dynamics of carbon nanoscrolls," *Nano letters*, vol. 4, no. 5, pp. 881–884, 2004.

[85] P. Zhang, L. Ma, F. Fan, Z. Zeng, C. Peng, P. E. Loya, Z. Liu, Y. Gong, J. Zhang, X. Zhang *et al.*, "Fracture toughness of graphene," *Nature communications*, vol. 5, 2014.

[86] R. Nair, P. Blake, A. Grigorenko, K. Novoselov, T. Booth, T. Stauber, N. Peres, and A. Geim, "Fine structure constant defines visual transparency of graphene," *Science*, vol. 320, no. 5881, pp. 1308–1308, 2008.

[87] D. Abergel, A. Russell, and V. I. Fal'ko, "Visibility of graphene flakes on a dielectric substrate," *arXiv preprint arXiv:0705.0091*, 2007.

[88] A. Grigorenko, M. Polini, and K. Novoselov, "Graphene plasmonics," *Nature photonics*, vol. 6, no. 11, pp. 749–758, 2012.

[89] L. Wu, H. Chu, W. Koh, and E. Li, "Highly sensitive graphene biosensors based on surface plasmon resonance," *Optics express*, vol. 18, no. 14, pp. 14 395–14 400, 2010.

[90] H. Jussila, H. Yang, N. Granqvist, and Z. Sun, "Surface plasmon resonance for characterization of large-area atomic-layer graphene film," *Optica*, vol. 3, no. 2, pp. 151–158, 2016.

[91] M. F. El-Kady, V. Strong, S. Dubin, and R. B. Kaner, "Laser scribing of high-performance and flexible graphene-based electrochemical capacitors," *Science*, vol. 335, no. 6074, pp. 1326–1330, 2012.

[92] M. F. El-Kady and R. B. Kaner, "Scalable fabrication of high-power graphene micro-supercapacitors for flexible and on-chip energy storage," *Nat Commun*, vol. 4, p. 1475, Feb. 2013.

[93] R. Raccichini, A. Varzi, S. Passerini, and B. Scrosati, "The role of graphene for electrochemical energy storage," *Nat Mater*, vol. 14, no. 3, pp. 271–279, Mar. 2015.

[94] Z. Zhu, J. Ma, Z. Wang, C. Mu, Z. Fan, L. Du, Y. Bai, L. Fan, H. Yan, D. L. Phillips, and S. Yang, "Efficiency enhancement of perovskite solar cells through fast electron extraction: The role of graphene quantum dots," *Journal of the American Chemical Society*, vol. 136, no. 10, pp. 3760–3763, 2014, pMID: 24558950.

[95] Z. Liu, Q. Liu, Y. Huang, Y. Ma, S. Yin, X. Zhang, W. Sun, and Y. Chen, "Organic photovoltaic devices based on a novel acceptor material: Graphene," *Advanced Materials*, vol. 20, no. 20, pp. 3924–3930, 2008.

[96] Z. Yang, H. Sun, T. Chen, L. Qiu, Y. Luo, and H. Peng, "Photovoltaic wire derived from a graphene composite fiber achieving an 8.45% energy conversion efficiency," *Angewandte Chemie International Edition*, vol. 52, no. 29, pp. 7545–7548, 2013.

[97] I. Valov, E. Linn, S. Tappertzhofen, S. Schmelzer, J. Van den Hurk, F. Lentz, and R. Waser, "Nanobatteries in redox-based resistive switches require extension of memristor theory," *Nature communications*, vol. 4, p. 1771, 2013.

[98] A. Geim, "Researchers show graphene is super-permeable with respect to water," *Membrane Technology*, 2012.

[99] D.-e. Jiang, V. R. Cooper, and S. Dai, "Porous graphene as the ultimate membrane for gas separation," *Nano letters*, vol. 9, no. 12, pp. 4019–4024, 2009.

[100] L. M. Pastrana-Martínez, S. Morales-Torres, J. L. Figueiredo, J. L. Faria, and A. M. Silva, "Graphene oxide based ultrafiltration membranes for photocatalytic degradation of organic pollutants in salty water," *Water Research*, vol. 77, pp. 179–190, Jun. 2015.

[101] B. M. Ludbrook, G. Levy, P. Nigge, M. Zonno, M. Schneider, D. J. Dvorak, C. N. Veenstra, S. Zhdanovich, D. Wong, P. Dosanjh, C. Straßer, A. Stöhr, S. Forti, C. R. Ast, U. Starke, and A. Damascelli, "Evidence for superconductivity in li-decorated monolayer graphene," *Proceedings of the National Academy of Sciences*, vol. 112, no. 38, pp. 11 795–11 799, 2015.

[102] S.-L. Yang, J. A. Sobota, C. A. Howard, C. J. Pickard, M. Hashimoto, D. H. Lu, S.-K. Mo, P. S. Kirchmann, and Z.-X. Shen, "Superconducting graphene sheets in CaC6 enabled by phonon-mediated interband interactions," *Nat Commun*, vol. 5, Mar. 2014.

[103] S. Bae, H. Kim, Y. Lee, X. Xu, J.-S. Park, Y. Zheng, J. Balakrishnan, T. Lei, H. Ri Kim, Y. I. Song, Y.-J. Kim, K. S. Kim, B. Ozyilmaz, J.-H. Ahn, B. H. Hong, and S. Iijima, "Roll-to-roll production of 30-inch graphene films for transparent electrodes," *Nat Nano*, vol. 5, no. 8, pp. 574–578, Aug. 2010.

[104] A. A. Balandin, S. Ghosh, W. Bao, I. Calizo, D. Teweldebrhan, F. Miao, and C. N. Lau, "Superior thermal conductivity of single-layer graphene," *Nano letters*, vol. 8, no. 3, pp. 902–907, 2008.

[105] T.-H. Han, Y. Lee, M.-R. Choi, S.-H. Woo, S.-H. Bae, B. H. Hong, J.-H. Ahn, and T.-W. Lee, "Extremely efficient flexible organic light-emitting diodes with modified graphene anode," *Nat Photon*, vol. 6, no. 2, pp. 105–110, Feb. 2012.

[106] J. Wu, M. Agrawal, H. A. Becerril, Z. Bao, Z. Liu, Y. Chen, and P. Peumans, "Organic light-emitting diodes on solution-processed graphene transparent electrodes," *ACS Nano*, vol. 4, no. 1, pp. 43–48, 2010, pMID: 19902961.

[107] I. Meric, M. Y. Han, A. F. Young, B. Ozyilmaz, P. Kim, and K. L. Shepard, "Current saturation in zero-bandgap, top-gated graphene field-effect transistors," *Nat Nano*, vol. 3, no. 11, pp. 654–659, Nov. 2008.

[108] M. C. Lemme, T. Echtermeyer, M. Baus, and H. Kurz, "A Graphene Field-Effect Device," *Electron Device Letters, IEEE*, vol. 28, no. 4, pp. 282–284, Apr. 2007.

[109] M. Pumera, "Graphene in biosensing," *Materials Today*, vol. 14, no. 7–8, pp. 308–315, Jul. 2011.

[110] Y. Ohno, K. Maehashi, Y. Yamashiro, and K. Matsumoto, "Electrolyte-Gated Graphene Field-Effect Transistors for Detecting pH and Protein Adsorption," *Nano Letters*, vol. 9, no. 9, pp. 3318–3322, Sep. 2009.

[111] A. Fabbro, D. Scaini, V. Leon, E. Vázquez, G. Cellot, G. Privitera, L. Lombardi, F. Torrisi, F. Tomarchio, F. Bonaccorso *et al.*, "Graphene-based interfaces do not alter target nerve cells," *ACS nano*, 2015.

[112] S. Stankovich, D. A. Dikin, G. H. Dommett, K. M. Kohlhaas, E. J. Zimney, E. A. Stach, R. D. Piner, S. T. Nguyen, and R. S. Ruoff, "Graphene-based composite materials," *nature*, vol. 442, no. 7100, pp. 282–286, 2006.

[113] J. Bardeen and W. H. Brattain, "The transistor, a semi-conductor triode," *Physical Review*, vol. 74, no. 2, p. 230, 1948.

[114] Z. Bao and J. Locklin, *Organic Field-Effect Transistors*, ser. Optical Science and Engineering. CRC Press, 2007.

[115] E. Tlelo-Cuautle, *Integrated Circuits for Analog Signal Processing*, ser. SpringerLink : Bücher. Springer New York, 2012.

[116] J. P. Uyemura, *CMOS logic circuit design*. Springer Science & Business Media, 1999.

[117] T. O'Reilly, "Effect of surface traps on characteristics of insulated-gate field-effect transistors," *Solid-State Electronics*, vol. 8, no. 3, pp. 267–274, 1965.

[118] X. Fang and L. Wu, *Handbook of Innovative Nanomaterials: From Syntheses to Applications*. Pan Stanford Publishing, 2012.

[119] A. Diallo, J. Tardy, Z. Zhang, F. Bessueille, N. Jaffrezic-Renault, and M. Lemiti, "Trimethylamine biosensor based on pentacene enzymatic organic field effect transistor," *Applied Physics Letters*, vol. 94, no. 26, p. 263302, 2009.

[120] M. Gerard, A. Chaubey, and B. Malhotra, "Application of conducting polymers to biosensors," *Biosensors and Bioelectronics*, vol. 17, no. 5, pp. 345–359, 2002.

[121] P. Mohanty, Y. Chen, X. Wang, M. K. Hong, C. L. Rosenberg, D. T. Weaver, and S. Erramilli, "Field effect transistor nanosensor for breast cancer diagnostics," *arXiv preprint arXiv:1401.1168*, 2014.

[122] K. Balasubramanian and M. Burghard, "Biosensors based on carbon nanotubes," *Analytical and bioanalytical chemistry*, vol. 385, no. 3, pp. 452–468, 2006.

[123] A. Liu, "Towards development of chemosensors and biosensors with metal-oxide-based nanowires or nanotubes," *Biosensors and Bioelectronics*, vol. 24, no. 2, pp. 167–177, 2008.

[124] W. Russel, D. Saville, and W. Schowalter, *Colloidal Dispersions*, ser. Cambridge Monographs on Mechanics. Cambridge University Press, 1989.

[125] R. Robinson and R. Stokes, *Electrolyte Solutions: Second Revised Edition*, ser. Dover Books on Chemistry Series. Dover Publications, Incorporated, 2012.

[126] A. Stogryn, "Equations for calculating the dielectric constant of saline water (correspondence)," *Microwave Theory and Techniques, IEEE Transactions on*, vol. 19, no. 8, pp. 733–736, Aug 1971.

[127] D. Gadani, V. Rana, S. Bhatnagar, A. Prajapati, and A. Vyas, "Effect of salinity on the dielectric properties of water," *Indian Journal of Pure and Applied Physics*, vol. 50, no. 6, pp. 405–410, 2012.

[128] E. Stern, R. Wagner, F. J. Sigworth, R. Breaker, T. M. Fahmy, and M. A. Reed, "Importance of the Debye Screening Length on Nanowire Field Effect Transistor Sensors," *Nano Letters*, vol. 7, no. 11, pp. 3405–3409, Nov. 2007.

[129] H. v. Helmholtz, "Ueber einige gesetze der vertheilung elektrischer ströme in körperlichen leitern mit anwendung auf die thierisch-elektrischen versuche," *Annalen der Physik*, vol. 165, no. 6, pp. 211–233, 1853.

[130] G. Gouy, "Sur la constitution de la charge electrique a la surface d'un electrolyte," *J. phys*, vol. 9, no. 4, pp. 457–468, 1910.

[131] O. Stern, "Zur theorie der elektrolytischen doppelschicht," *Zeitschrift für Elektrochemie und angewandte physikalische Chemie*, vol. 30, no. 21-22, pp. 508–516, 1924.

[132] D. C. Grahame, "The electrical double layer and the theory of electrocapillarity." *Chemical reviews*, vol. 41, no. 3, pp. 441–501, 1947.

[133] I. Langmuir, "THE ADSORPTION OF GASES ON PLANE SURFACES OF GLASS, MICA AND PLATINUM." *Journal of the American Chemical Society*, vol. 40, no. 9, pp. 1361–1403, Sep. 1918.

[134] ——, "The constitution and fundamental properties of solids and liquids. part i. solids." *Journal of the American Chemical Society*, vol. 38, no. 11, pp. 2221–2295, 1916.

[135] C. Rozman, "Konstruktion und optimierung eines auf graphen basierenden feld-effekt-transistor-devices," 2013, diploma thesis.

[136] W. Kauzmann, "Some factors in the interpretation of protein denaturation1," ser. Advances in Protein Chemistry, K. B. C.B. Anfinsen, M.L. Anson and J. T. Edsall, Eds. Academic Press, 1959, vol. 14, pp. 1 – 63.

[137] H. Flyvbjerg, J. Hertz, M. Jensen, O. Mouritsen, and K. Sneppen, *Physics of Biological Systems: From Molecules to Species*, ser. Lecture Notes in Physics. Springer Berlin Heidelberg, 1997.

[138] J. N. Onuchic, Z. Luthey-Schulten, , and P. G. Wolynes, "Theory of protein folding: The energy landscape perspective," *Annual Review of Physical Chemistry*, vol. 48, no. 1, pp. 545–600, 1997, pMID: 9348663.

[139] A. Volkov and D. Deamer, *Liquid-Liquid InterfacesTheory and Methods*. Taylor & Francis, 1996.

[140] C. J. Alexopoulos, "Introductory mycology." *Soil Science*, vol. 74, no. 6, p. 481, 1952.

[141] A. Ciegler and J. Bennett, "Mycotoxins and mycotoxicoses," *Bioscience*, vol. 30, no. 8, pp. 512–515, 1980.

[142] J. F. D'Mello, *Handbook of plant and fungal toxicants*. CRC Press, 1997.

[143] C. A. Robbins, L. J. Swenson, M. L. Nealley, B. J. Kelman, and R. E. Gots, "Health effects of mycotoxins in indoor air: a critical review," *Applied occupational and environmental hygiene*, vol. 15, no. 10, pp. 773–784, 2000.

[144] "Secondary metabolism: regulation and role in fungal biology," *Current Opinion in Microbiology*, vol. 11, no. 6, pp. 481 – 487, 2008, growth and Development: Eukaryotes/Prokaryotes.

[145] J. Dijksterhuis and R. A. Samson, *Food mycology: a multifaceted approach to fungi and food*. CRC Press, 2007.

[146] K. Mendgen and M. Hahn, "Plant infection and the establishment of fungal biotrophy," *Trends in plant science*, vol. 7, no. 8, pp. 352–356, 2002.

[147] D. Prusky, J. L. McEvoy, B. Leverentz, and W. S. Conway, "Local modulation of host ph by colletotrichum species as a mechanism to increase virulence," *Molecular Plant-Microbe Interactions*, vol. 14, no. 9, pp. 1105–1113, 2001.

[148] A. Tiedemann, "Evidence for a primary role of active oxygen species in induction of host cell death during infection of bean leaves withbotrytis cinerea," *Physiological and Molecular Plant Pathology*, vol. 50, no. 3, pp. 151–166, 1997.

[149] L. C. Vining, "Functions of secondary metabolites," *Annual Reviews in Microbiology*, vol. 44, no. 1, pp. 395–427, 1990.

[150] A. Morton, "The induction of sporulation in mould fungi," *Proceedings of the Royal Society of London B: Biological Sciences*, vol. 153, no. 953, pp. 548–569, 1961.

[151] M. Castro, K. Kramer, L. Valdivia, S. Ortiz, and A. Castillo, "A double-stranded rna mycovirus confers hypovirulence-associated traits to botrytis cinerea," *FEMS Microbiology Letters*, vol. 228, no. 1, pp. 87–91, 2003.

[152] M. A. Flaishman and P. E. Kolattukudy, "Timing of fungal invasion using host's ripening hormone as a signal," *Proceedings of the National Academy of Sciences*, vol. 91, no. 14, pp. 6579–6583, 1994.

[153] A. El-Ghaouth, "Biologically-based alternatives to synthetic fungicides for the control of postharvest diseases," *Journal of Industrial Microbiology and Biotechnology*, vol. 19, no. 3, pp. 160–162, 1997.

[154] E. Boutrif and C. Canet, "Mycotoxin prevention and control: Fao programmes," *Revue de Medecine Veterinaire (France)*, 1998.

[155] C. Probst, H. Njapau, and P. J. Cotty, "Outbreak of an acute aflatoxicosis in kenya in 2004: identification of the causal agent," *Applied and Environmental Microbiology*, vol. 73, no. 8, pp. 2762–2764, 2007.

[156] L. B. Bullerman and A. Bianchini, "Stability of mycotoxins during food processing," *International Journal of Food Microbiology*, vol. 119, no. 1–2, pp. 140 – 146, 2007, mycotoxins from the Field to the Table.

[157] P. Restani, "Diffusion of mycotoxins in fruits and vegetables," in *Mycotoxins in Fruits and Vegetables*. Elsevier San Diego, California, 2008, pp. 105–114.

[158] P. White and L. Johnson, *Corn: Chemistry and Technology*, ser. AACC monograph series. American Association of Cereal Chemists, 2003.

[159] *Aflatoxins in foods and feeds.*

[160] M. Manabe, T. Goto, and S. Matsuura, "High-performance liquid chromatography of aflatoxins with fluorescence detection," *Agricultural and Biological Chemistry*, vol. 42, no. 11, pp. 2003–2007, 1978.

[161] S. C. Basappa, *Aflatoxins: Formation, analysis and Cotrol.* Alpha Science, 2009.

[162] D. H. Swenson, J.-K. Lin, E. C. Miller, and J. A. Miller, "Aflatoxin b1-2, 3-oxide as a probable intermediate in the covalent binding of aflatoxins b1 and b2 to rat liver dna and ribosomal rna in vivo," *Cancer Research*, vol. 37, no. 1, pp. 172–181, 1977.

[163] C. Stora, I. Dvorackova, and N. Ayraud, "Characterization of aflatoxin bi (afb) in human liver cancer." *Research communications in chemical pathology and pharmacology*, vol. 31, no. 1, pp. 77–84, 1981.

[164] C. P. S. Sekhon, J. Kapur, S. S. Sodhi, and S. K. Jand, "Qualitative and quantitative detection of aflatoxin b1 in poultry sera by enzyme-linked immunosorbent assay," *Journal of Biosciences*, vol. 21, no. 4, pp. 471–476.

[165] R. Ghali, I. Belouaer, S. Hdiri, H. Ghorbel, K. Maaroufi, and A. Hedilli, "Simultaneous {HPLC} determination of aflatoxins b1, b2, {G1} and {G2} in tunisian sorghum and pistachios," *Journal of Food Composition and Analysis*, vol. 22, no. 7–8, pp. 751 – 755, 2009.

[166] Y. Wang, N. Liu, B. Ning, M. Liu, Z. Lv, Z. Sun, Y. Peng, C. Chen, J. Li, and Z. Gao, "Simultaneous and rapid detection of six different mycotoxins using an immunochip," *Biosensors and Bioelectronics*, vol. 34, no. 1, pp. 44 – 50, 2012.

[167] A. Beizaei, S. L. O. Kane, A. Kamkar, A. Misaghi, G. Henehan, and D. J. Cahill, "Highly sensitive toxin microarray assay for aflatoxin {B1} detection in cereals," *Food Control*, vol. 57, pp. 210 – 215, 2015.

[168] M. Vosough and A. Salemi, "Exploiting second-order advantage using parafac2 for fast hplc-dad quantification of mixture of aflatoxins in pistachio nuts," *Food Chemistry*, vol. 127, no. 2, pp. 827 – 833, 2011.

[169] M. Carlson, C. Bargeron, R. Benson, A. Fraser, T. Phillips, J. Velky, J. Groopman, P. Strickland, and H. Ko, "An automated, handheld biosensor for aflatoxin," *Biosensors and Bioelectronics*, vol. 14, no. 10, pp. 841–848, 2000.

[170] C. S. Ah, C. W. Park, J.-H. Yang, J. S. Lee, W.-J. Kim, K. H. Chung, Y. H. Choi, I. B. Baek, J. Kim, and G. Y. Sung, "Detection of uncharged or feebly charged small molecules by field-effect transistor biosensors," *Biosensors and Bioelectronics*, vol. 33, no. 1, pp. 233–240, 2012.

[171] R. A. Villamizar, A. Maroto, and F. X. Rius, "Rapid detection of aspergillus flavus in rice using biofunctionalized carbon nanotube field effect transistors," *Analytical and bioanalytical chemistry*, vol. 399, no. 1, pp. 119–126, 2011.

[172] R. Paolesse, A. Alimelli, E. Martinelli, C. Di Natale, A. D'Amico, M. G. D'Egidio, G. Aureli, A. Ricelli, and C. Fanelli, "Detection of fungal contamination of cereal grain samples by an electronic nose," *Sensors and Actuators B: Chemical*, vol. 119, no. 2, pp. 425–430, 2006.

[173] G. Keshri and N. Magan, "Detection and differentiation between mycotoxigenic and non-mycotoxigenic strains of two fusarium spp. using volatile production profiles and hydrolytic enzymes," *Journal of Applied Microbiology*, vol. 89, no. 5, pp. 825–833, 2000.

[174] M. Falasconi, E. Gobbi, M. Pardo, M. Della Torre, A. Bresciani, and G. Sberveglieri, "Detection of toxigenic strains of fusarium verticillioides in corn by electronic olfactory system," *Sensors and Actuators B: Chemical*, vol. 108, no. 1, pp. 250–257, 2005.

[175] S. Amaya-González, N. de-los Santos-Álvarez, A. J. Miranda-Ordieres, and M. J. Lobo-Castañón, "Aptamer-based analysis: A promising alternative for food safety control," *Sensors*, vol. 13, no. 12, pp. 16 292–16 311, 2013.

[176] P. Mandal, A. Biswas, K. Choi, and U. Pal, "Methods for rapid detection of foodborne pathogens: an overview," *American Journal Of Food Technology*, vol. 6, no. 2, pp. 87–102, 2011.

[177] C. Smith, J. Betrán, and E. Runge, *Corn: Origin, History, Technology, and Production*, ser. Wiley Series in Crop Science. Wiley, 2004.

[178] J. A. Beti, T. W. Phillips, and E. B. Smalley, "Effects of maize weevils (coleoptera: Curculionidae) on production of aflatoxin b1 by aspergillus flavus in stored corn," *Journal of Economic Entomology*, vol. 88, no. 6, pp. 1776–1782, 1995.

[179] M. Larisika, J. Huang, A. Tok, W. Knoll, and C. Nowak, "An improved synthesis route to graphene for molecular sensor applications," *Materials Chemistry and Physics*, vol. 136, no. 2–3, pp. 304 – 308, 2012.

[180] E. Wegmüller, A. Montandon, U. Nydegger, and C. Descoeudres, "Biocompatibility of different hemodialysis membranes: activation of complement and leukopenia," *The International journal of artificial organs*, vol. 9, no. 2, p. 85—92, March 1986.

[181] R. Lanche, L. E. Delle, M. Weil, X. T. Vu, V. Pachauri, W. M. Munief, P. Wagner, and S. Ingebrandt, "Routine fabrication of reduced graphene oxide microarray devices via all solution processing," *physica status solidi (a)*, vol. 210, no. 5, pp. 968–974, 2013.

[182] P. K. Ang, S. Wang, Q. Bao, J. T. L. Thong, and K. P. Loh, "High-Throughput Synthesis of Graphene by Intercalation Exfoliation of Graphite Oxide and Study of Ionic Screening in Graphene Transistor," *ACS Nano*, vol. 3, no. 11, pp. 3587–3594, Nov. 2009.

[183] C. Reiner-Rozman, J. Schodl, C. Nowak, and C. Kleber, "Scanning electrochemical microscopy as a characterization tool for reduced graphene oxide field effect transistors," *e-Journal of Surface Science and Nanotechnology*, vol. 13, pp. 366–372, 2015.

[184] J. Molina, J. Fernández, J. Inés, A. del Río, J. Bonastre, and F. Cases, "Electrochemical characterization of reduced graphene oxide-coated polyester fabrics," *Electrochimica Acta*, vol. 93, pp. 44 – 52, 2013.

[185] J. Molina, J. Fernández, A. del Río, J. Bonastre, and F. Cases, "Chemical and electrochemical study of fabrics coated with reduced graphene oxide," *Applied Surface Science*, vol. 279, pp. 46 – 54, 2013.

[186] M. A. Mezour, M. Morin, and J. Mauzeroll, "Fabrication and characterization of laser pulled platinum microelectrodes with controlled geometry," *Analytical Chemistry*, vol. 83, no. 6, pp. 2378–2382, 2011, pMID: 21323390.

[187] B. Katemann and W. Schuhmann, "Fabrication and characterization of needle-type," *Electroanalysis*, vol. 14, no. 1, pp. 22–28, 2002.

[188] W. Fu, C. Nef, O. Knopfmacher, A. Tarasov, M. Weiss, M. Calame, and C. Schönenberger, "Graphene transistors are insensitive to ph changes in solution," *Nano Letters*, vol. 11, no. 9, pp. 3597–3600, 2011, pMID: 21766793.

[189] S. Tanaka, H. Goto, H. Tomori, Y. Ootuka, K. Tsukagoshi, and A. Kanda, "Effect of current annealing on electronic properties of multilayer graphene," *Journal of Physics: Conference Series*, vol. 232, no. 1, p. 012015, 2010.

[190] E. V. Castro, H. Ochoa, M. I. Katsnelson, R. V. Gorbachev, D. C. Elias, K. S. Novoselov, A. K. Geim, and F. Guinea, "Limits on charge carrier mobility in suspended graphene due to flexural phonons," *Phys. Rev. Lett.*, vol. 105, p. 266601, Dec 2010.

[191] V. Zeghbroeck, *Principles of Semiconductor Devices and Heterojunctions*. Prentice Hall PTR, 2007.

[192] J.-P. Randin and E. Yeager, "Differential capacitance study on the basal plane of stress-annealed pyrolytic graphite," *Journal of Electroanalytical Chemistry and Interfacial Electrochemistry*, vol. 36, no. 2, pp. 257–276, May 1972.

[193] C. Punckt, M. A. Pope, and I. A. Aksay, "On the electrochemical response of porous functionalized graphene electrodes," *The Journal of Physical Chemistry C*, vol. 117, no. 31, pp. 16 076–16 086, 2013.

[194] R. Schasfoort and A. Tudos, *Handbook of Surface Plasmon Resonance*. Royal Society of Chemistry, 2008.

[195] R. Van Hal, J. Eijkel, and P. Bergveld, "A general model to describe the electrostatic potential at electrolyte oxide interfaces," *Advances in colloid and interface science*, vol. 69, no. 1, pp. 31–62, 1996.

[196] P. Bergveld and A. Sibbald, *Analytical and Biomedical Applications of Ion-selective Field-effect Transistors*, ser. Analytical and Biomedical Applications of Ion-selective Field-effect Transistors. Elsevier, 1988.

[197] R. Tian, S. Regonda, J. Gao, Y. Liu, and W. Hu, "Ultrasensitive protein detection using lithographically defined si multi-nanowire field effect transistors," *Lab Chip*, vol. 11, pp. 1952–1961, 2011.

[198] C. Rozman, "Flow and pressure sensitive graphene sensor," Sep. 30 2015, eP Patent App. EP20,140,162,292.

[199] A. K. M. Newaz, D. A. Markov, D. Prasai, and K. I. Bolotin, "Graphene transistor as a probe for streaming potential," *Nano Letters*, vol. 12, no. 6, pp. 2931–2935, 2012, pMID: 22568874.

[200] J. E. Proctor, E. Gregoryanz, K. S. Novoselov, M. Lotya, J. N. Coleman, and M. P. Halsall, "High-pressure raman spectroscopy of graphene," *Phys. Rev. B*, vol. 80, p. 073408, Aug 2009.

[201] ——, "Graphene under hydrostatic pressure," *arXiv preprint arXiv:0905.3103*, 2009.

[202] "Electricity generator or flow speed measuring method based on graphite alkene and the air stream." Feb. 1 2012, cN Patent App. CN 201,110,167,203.

[203] H. U. Khan, J. Jang, J.-J. Kim, and W. Knoll, "In Situ Antibody Detection and Charge Discrimination Using Aqueous Stable Pentacene Transistor Biosensors," *Journal of the American Chemical Society*, vol. 133, no. 7, pp. 2170–2176, Feb. 2011.

[204] X. Li, P. Li, Q. Zhang, Y. Li, W. Zhang, and X. Ding, "Molecular characterization of monoclonal antibodies against aflatoxins: A possible explanation for the highest sensitivity," *Analytical Chemistry*, vol. 84, no. 12, pp. 5229–5235, 2012, pMID: 22548609.

[205] X. Wang, R. Niessner, and D. Knopp, "Magnetic Bead-Based Colorimetric Immunoassay for Aflatoxin B1 Using Gold Nanoparticles," *Sensors (Basel, Switzerland)*, vol. 14, no. 11, pp. 21 535–21 548, Nov. 2014.

[206] X. Xu, X. Liu, Y. Li, and Y. Ying, "A simple and rapid optical biosensor for detection of aflatoxin B1 based on competitive dispersion of gold nanorods," *Biosensors and Bioelectronics*, vol. 47, pp. 361–367, Sep. 2013.

[207] A. Zanobini, P. Vanni, E. Mastronuzzi, A. Firenzuoli, and G. Ramponi, "Use of tween 80 in ferredoxin extraction from gymnosperms," *Phytochemistry*, vol. 6, no. 12, pp. 1633 – 1635, 1967.

[208] S. Spaan, D. J. J. Heederik, P. S. Thorne, and I. M. Wouters, "Optimization of airborne endotoxin exposure assessment: Effects of filter type, transport conditions, extraction solutions, and storage of samples and extracts," *Applied and Environmental Microbiology*, vol. 73, no. 19, pp. 6134 – 6143, 2007.

[209] J. Kenna, G. Major, and R. Williams, "Methods for reducing non-specific antibody binding in enzyme-linked immunosorbent assays," *Journal of Immunological Methods*, vol. 85, no. 2, pp. 409 – 419, 1985.

[210] E. A. Coors, H. Seybold, H. F. Merk, and V. Mahler, "Polysorbate 80 in medical products and nonimmunologic anaphylactoid reactions," *Annals of Allergy, Asthma & Immunology*, vol. 95, no. 6, pp. 593 – 599, 2005.

[211] C. W. Park, J.-H. Yang, C. S. Ah, C.-G. Ahn, Y. H. Choi, K. H. Chung, W.-J. Kim, and G. Y. Sung, "Toxin detection by si photosensitive biosensors with a new measurement scheme," *Biosensors and Bioelectronics*, vol. 29, no. 1, pp. 219 – 223, 2011.

[212] J. P. Kim, B. Y. Lee, J. Lee, S. Hong, and S. J. Sim, "Enhancement of sensitivity and specificity by surface modification of carbon nanotubes in diagnosis of prostate cancer based on carbon nanotube field effect transistors," *Biosensors and Bioelectronics*, vol. 24, no. 11, pp. 3372 – 3378, 2009.

[213] P. Debye and E. Hückel, "De la théorie des électrolytes. i. abaissement du point de congélation et phénomènes associés," *Physikalische Zeitschrift*, vol. 24, no. 9, pp. 185–206, 1923.

[214] P. Aspermair, "Odorant messungen mit funktionalisierten graphene feldeffekttransistoren unter verwendung von impendanzspektroskopie," 2016, diploma thesis.

[215] K. Yang, L. Feng, X. Shi, and Z. Liu, "Nano-graphene in biomedicine: theranostic applications," *Chem. Soc. Rev.*, vol. 42, pp. 530–547, 2013.

[216] C. M. Castilla, "Adsorption of organic molecules from aqueous solutions on carbon materials," *Carbon*, vol. 42, no. 1, pp. 83 – 94, 2004.

[217] Y. Liu, X. Dong, and P. Chen, "Biological and chemical sensors based on graphene materials," *Chemical Society Reviews*, vol. 41, no. 6, pp. 2283–2307, 2012.

[218] X. Zhang, S. Wan, J. Pu, L. Wang, and X. Liu, "Highly hydrophobic and adhesive performance of graphene films," *Journal of Materials Chemistry*, vol. 21, no. 33, pp. 12 251–12 258, 2011.

[219] S. Banerjee, T. Hemraj-Benny, and S. S. Wong, "Covalent surface chemistry of single-walled carbon nanotubes," *Advanced Materials*, vol. 17, no. 1, pp. 17–29, 2005.

[220] Y. Wang, Z. Li, J. Wang, J. Li, and Y. Lin, "Graphene and graphene oxide: biofunctionalization and applications in biotechnology," *Trends in biotechnology*, vol. 29, no. 5, pp. 205–212, 2011.

[221] K. E. Heusler, D. Landolt, and S. Trasatti, "Electrochemical corrosion nomenclature (recommendations 1988)," *Pure Appl. Chem.*, vol. 61, pp. 19–22, 1989.

[222] C. Christensen, R. de Reus, and S. Bouwstra, "Tantalum oxide thin films as protective coatings for sensors," *Journal of Micromechanics and Microengineering*, vol. 9, no. 2, p. 113, 1999.

[223] C. Chaneliere, J. Autran, R. Devine, and B. Balland, "Tantalum pentoxide (ta2o5) thin films for advanced dielectric applications," *Materials Science and Engineering: R: Reports*, vol. 22, no. 6, pp. 269 – 322, 1998.

[224] K. Chen, M. Nielsen, G. R. Yang, E. J. Rymaszewski, and T. M. Lu, "Study of amorphous ta2o5 thin films by dc magnetron reactive sputtering," *Journal of Electronic Materials*, vol. 26, no. 4, pp. 397–401.

[225] J. Zhang, S. Li, and P. W. Carter, "Chemical mechanical polishing of tantalum aqueous interfacial reactivity of tantalum and tantalum oxide," *Journal of The Electrochemical Society*, vol. 154, no. 2, pp. H109–H114, 2007.

[226] T. Riekkinen and J. Molarius, "Reactively sputtered tantalum pentoxide thin films for integrated capacitors," *Microelectronic Engineering*, vol. 70, no. 2–4, pp. 392 – 397, 2003, materials for Advanced Metallization 2003.

[227] O. Kerrec, D. Devilliers, H. Groult, and M. Chemla, "Dielectric properties of anodic oxide films on tantalum," *Electrochimica Acta*, vol. 40, no. 6, pp. 719 – 724, 1995.

[228] "A novel description of {ISFET} sensitivity with the buffer capacity and double-layer capacitance as key parameters," *Sensors and Actuators B: Chemical*, vol. 24, no. 1–3, pp. 201 – 205, 1995.

[229] M. Hiratani, S. Kimura, T. Hamada, S. Iijima, and N. Nakanishi, "Hexagonal polymorph of tantalum-pentoxide with enhanced dielectric constant," *Applied physics letters*, vol. 81, p. 2433, 2002.

[230] S.-i. Kimura, Y. Nishioka, A. Shintani, and K. Mukai, "Leakage-current increase in amorphous ta2o5 films due to pinhole growth during annealing below 600 degrees c," *Journal of the Electrochemical Society*, vol. 130, no. 12, pp. 2414–2418, 1983.

[231] C. Cannes, F. Kanoufi, and A. J. Bard, "Cyclic voltammetry and scanning electrochemical microscopy of ferrocenemethanol at monolayer and bilayer-modified gold electrodes," *Journal of Electroanalytical Chemistry*, vol. 547, no. 1, pp. 83 – 91, 2003.

[232] M. Rehak and E. A. H. Hall, "Examination of bilayer lipid membranes for 'pin-hole' character," *Analyst*, vol. 129, pp. 1014–1025, 2004.

[233] A. Villares, G. Pera, I. Giner, P. Cea, M. C. López, and S. Martín, "The use of cyclic voltammetry to probe the passivation of electrode surfaces by well-ordered self-assembly and langmuir–blodgett films. an advanced undergraduate laboratory experiment in surface science and nanomaterials chemistry," *Journal of chemical education*, vol. 86, no. 6, p. 723, 2009.

[234] D. Rodbard and S. McClean, "Automated computer analysis for enzyme-multiplied immunological techniques." *Clinical chemistry*, vol. 23, no. 1, pp. 112–115, 1977.

[235] Q. He, S. Wu, Z. Yin, and H. Zhang, "Graphene-based electronic sensors," *Chem. Sci.*, vol. 3, no. 6, pp. 1764–1772, 2012.

[236] Y. Liu, D. Yu, C. Zeng, Z. Miao, and L. Dai, "Biocompatible graphene oxide-based glucose biosensors," *Langmuir*, vol. 26, no. 9, pp. 6158–6160, 2010, pMID: 20349968.

[237] A. Palaniappan, W. Goh, D. Fam, G. Rajaseger, C. Chan, B. Hanson, S. Moochhala, S. Mhaisalkar, and B. Liedberg, "Label-free electronic detection of bio-toxins using aligned carbon nanotubes," *Biosensors and Bioelectronics*, vol. 43, pp. 143 – 147, 2013.

[238] L. Wang, W. Chen, D. Xu, B. S. Shim, Y. Zhu, F. Sun, L. Liu, C. Peng, Z. Jin, C. Xu, and N. A. Kotov, "Simple, rapid, sensitive, and versatile swntpaper sensor for environmental toxin detection competitive with elisa," *Nano Letters*, vol. 9, no. 12, pp. 4147–4152, 2009, pMID: 19928776.

Acknowledgements

Thw work was conducted at CEST, Austria's Centre for Excellence for Electrochemical Surface Technology and the Austrian Institute of Technology in the common framework of a COMET/FFG project with Romer Labs®. The financial support of the FFG and the government of Lower Austria is highly appreciated.

The work would not been possible without the support and care of my colleagues and other people around me. Special thanks go to Wolfgang Knoll, Christoph Kleber, Christina Bliem, Caroline Kotlowski, Andreas Geiß, Patrik Aptermair, Jürgen Schodl, Christoph Steininger, Niko Leitner, JKU Linz, Prof. Hassel, Johannes Srajer, Andreas Schweighofer, Jakub Dostalek, Pinar Frank, Esteban Peccini, Ulrich Ramach, Anja Agneter, Renate Naumann, my family and everyone else that supported me during this time. Thanks for the experiences and fruitful discussions.

Erklärung

Ich erkläre, dass ich die vorgelegte Thesis selbständig, ohne unerlaubte fremde Hilfe und nur mit den Hilfen angefertigt habe, die ich in der Thesis angegeben habe. Alle Textstellen, die wörtlich oder sinngemäß aus veröffentlichten oder nicht veröffentlichten Schriften entnommen sind, und alle Angaben, die auf mündlichen Auskünften beruhen, sind als solche kenntlich gemacht. Bei den von mir durchgeführten Untersuchungen habe ich die Grundsätze guter wissenschaftlicher Praxis, wie sie in der Satzung der Johannes Gutenberg - Universität Mainz zur Sicherung guter wissenschaftlicher Praxis niedergelegt sind, eingehalten.“